الجمهورية الجزائرية الديمقراطية الشعبية

PEOPLE'S DEMOCRATIC REPUBLIC OF ALGERIA

وزارة التعليم العالي والبحث العلمي

MINISTRY OF HIGHER EDUCATION AND SCIENTIFIC RESEARCH

المدرسة الوطنية العليا للتكنولوجيا والهندسة – عنابة

NATIONAL HIGHER SCHOOL OF TECHNOLOGY AND ENGINEERING

DEPARTMENT OF PROCESS AND ENERGY ENGINEERING

THESIS FOR THE OBTENTION OF THIRD CYCLE DOCTORAL DEGREE IN

DOMAIN: SCIENCE AND TECHNOLOGY

FIELD: MECHANICAL ENGINEERING

OPTION: RENEWABLE ENERGIES IN MECHANICS

SOLAR ENERGY TO GREEN HYDROGEN: EXPLORATION OF THE ELECTRO-SONOLYTIC PATHWAY IN A PERSPECTIVE OF SUSTAINABLE DEVELOPMENT

PRESENTED BY

NOUR HANE MERABET

Defended on May 19th, 2024, in front of the Jury's members:

MEMBER	RANK	ROLE	INSTITUTION
HAMOUDA BOUTAGHANE	PROFESSOR	PRESIDENT	BADJI MOKHTAR UNIVERSITY-ANNABA
KAOUTHER KERBOUA	MCA	SUPERVISOR	NATIONAL HIGHER SCHOOL OF TECHNOLOGY AND ENGINEERING
JAN HOINKIS	PROFESSOR	CO-SUPERVISOR	KARLSRUHE UNIVERSITY OF APPLIED SCIENCES-GERMANY
MOUNA NACEF	PROFESSOR	EXAMINATOR	8 MAI 1945 UNIVERSITY-GUELMA
RIYADH BELAMADI	MCA	EXAMINATOR	NATIONAL HIGHER SCHOOL OF TECHNOLOGY AND ENGINEERING
SALIMA BENDEBANE	MCA	EXAMINATOR	NATIONAL HIGHER SCHOOL OF TECHNOLOGY AND ENGINEERING

2023/2024

Acknowledgment

I would like to thank my supervisor Dr.Kerboua Kaouther from the bottom of my heart for being a good example to me professionally and personally, for being the person who guided me, supported me to achieve my goals and believed in me all the way. I wouldn't have made it this far without you, you have been more than a supervisor to me.

I would also like to express my sincere, deep and heartfelt thanks to Prof. Jan Hoinkis, Faculty of Electrical Engineering and Electronics, Karlsruhe University of Applied Sciences, Karlsruhe, Germany, for his help and guidance throughout this thesis, as well as his expertise and for always being present to listen and help me.

I am particularly grateful to the DAAD for the financial assistance and the opportunity to carry out my doctorate within the binational doctorate between the university of applied sciences Karlsruhe, Germany, and the National Higher Technical School, Annaba, Algeria.

Many thanks to the members of the laboratory of my university in Algeria, to Fahima, Ramzi, Intissar and Sarah for their help and the positive energy that they used to spread together with the beautiful Soul 'Nada', who created the atmosphere of a family.

I would also like to express my special thanks to Sneha De, who helped me to better understand the experimental work carried out at HKA and provided me with a high level of knowledge of MBR technology. A big thank you to my colleagues in the lab, Duc, Edgardo, Ulrich, Talha and Margarita, who were always ready to help me in any way they could during my work at the HKA.

I would also like to express my gratitude to the ITM team in University of Calabria, to Enrica, Elisa and Valentina for their support during my stay in Italy and for their wealth of knowledge in the field of membrane technologies.

A big thank you to my family, my parents, my sister Achouak and my brother Kheir eddine for being the most supportive family and the best gift God gave me. Thank you from the bottom of my heart to my friends Salah eddine, Rayen, Lina, Rabab, Lina, Asma and Ines, to whom I am grateful for being the real people in my life.

…. Thank you

Dedication

THANKS GOD FOR THE STRENGTH AND THE CHANCE GIVEN TO ME TO COMPLETE THIS WORK AND LIVE THIS DAY.

TO ALL MY DEAR PEOPLE WHO STOOD BY MY SIDE AND WAITED FOR THE FRUITS OF THIS WORK, THANK YOU FOR MAKING ME SEE THIS ADVENTURE THROUGH TO THE END

… TO YOU I DEDICATE THIS WORK.

Nour Hane

PREFACE

The motivation for the current research project entitled "Solar Energy to Green Hydrogen: Exploration of the Electro-Sonolytic Pathway in a Perspective of Sustainable Development" stems from a deep interest in the field of renewable energy and innovative technologies. The primary objective was to make a modest contribution to the field of green hydrogen production and wastewater management. The journey of researching and writing this thesis lasted from April 2021 to November 2023.

Throughout this journey, I have had the privilege of immersing myself in a wealth of scientific literature, complemented by practical experimentation, thereby broadening my understanding of electrochemistry, sono-electrochemistry, wastewater treatment, photovoltaic solar energy supply and green hydrogen. The guidance and expertise of my two supervisors were instrumental in overcoming the challenges encountered at various stages of this research. I also gained useful understanding in MATLAB modelling, membrane bioreactor operation and water quality analysis. The PhD experience has not only enhanced my analytical skills but also refined my approach to problem solving, enriching me both professionally and personally.

I would like to express my sincere gratitude to Dr. Kaouther Kerboua, whose endless support, guidance and vast knowledge contributed greatly to the completion of this thesis. Her mentorship played a crucial role in securing the DAAD scholarship, for which I am deeply grateful. I would like also to express my gratitude to Prof. Jan Hoinkis at the University of Applied Sciences Karlsruhe, whose support enabled me to broaden my scientific horizons and to undertake an internship in a well-known laboratory specialized in membrane technologies.

I would like to thank the esteemed members of the Process Engineering Laboratory at the National Higher School of Technology and Engineering and the Water for Life Laboratory at the Karlsruhe University of Applied Sciences for their invaluable contributions and support.

Finally, I am grateful to my family and friends for their continuous encouragement and support throughout this journey. To the distinguished examiners and jury members, I hope that you will find value in this research project as you engage with its contents.

Nour Hane Merabet
Karlsruhe, February 16, 2024

SCIENTIFIC PUBLICATIONS

Merabet NH, Kerboua K, Hoinkis J (2024) Hydrogen production from wastewater: A comprehensive review of conventional and solar powered technologies. Renew Energy 226:120412. https://doi.org/10.1016/j.renene.2024.120412

N.H. Merabet, K. Kerboua, Green hydrogen from sono-electrolysis : A coupled numerical and experimental study of the ultrasound assisted membraneless electrolysis of water supplied by PV, Fuel. 356 (2024) 129625. https://doi.org/10.1016/j.fuel.2023.129625.

Merabet, N., Kerboua, K., 2023. Membrane free alkaline sono-electrolysis for hydrogen production: an experimental approach, International Journal of Hydrogen Energy https://www.sciencedirect.com/science/article/abs/pii/S0360319923046268

Kerboua, K., Merabet, N., 2023. Sono-electrolysis performance based on indirect continuous sonication and membraneless alkaline electrolysis: experiment, modelling and analysis, Ultrasonics Sonochemistry https://www.sciencedirect.com/science/article/pii/S1350417723001414?via%3Dihub

Merabet, N., Kerboua, K., 2022. Sonolytic and ultrasound-assisted techniques for hydrogen production: A review based on the role of ultrasound. International journal of hydrogen energy. https://www.sciencedirect.com/science/article/abs/pii/S036031992201655X?via%3Dihub

N. Merabet, L. Chouichi, K. Kerboua, Numerical design and simulation of a thermodynamic solar solution for a pilot residential building at the edge of the sun-belt region, Environ. Dev. Sustain. (2021). https://doi.org/10.1007/s10668-021-01956-2.

Merabet, N., Kerboua, K., 2022. The sonochemical and ultrasound-assisted production of hydrogen: Energy efficiency for the generation of an energy carrier, in: Hamdaoui, O., Kerboua, K. (Eds.), Energy Aspects of Acoustic Cavitation and Sonochemistry. Fundamentals and Engineering. Elsevier https://www.sciencedirect.com/science/article/abs/pii/B9780323919371000049?via%3Dihub

Merabet, N., Kerboua, K., Hamdaoui, O., 2023. Converting PV solar energy to green hydrogen, in Encyclopaedia of Renewable Energy, Sustainability, and the Environment. https://www.sciencedirect.com/science/article/abs/pii/B9780323939409000438?via%3Dihub

Merabet NH, Kerboua K. Comprehensive Modeling Study of the Electrical Performance of a Sono- Electrolyzer under a Voltage and Current Sources Supply : From Grey to Green Hydrogen. *Eurasia Proc Sci Technol Eng Math* 2023;**23**:400–5. http://www.epstem.net/en/pub/issue/79793/1371761

Merabet NH, Kerboua K. Green Hydrogen from PV-Supplied Sono-Electrolysis : Modelling and Experimental Investigations of the Mechanism and Performance. *Eurasia Proc Sci Technol Eng Math* 2023;**23**:100–5. http://www.epstem.net/en/pub/issue/79793/1363356

Merabet NH, Kerboua K. Dynamic Response of a Sono-Electrolyzer under PV Supply for Hydrogen Production: A Modelling Approach for the Kinetic and Energetic Assessment under Northern Algerian Meteorological Conditions. *Eng Proc* 2023;**56**:1–6. https://www.mdpi.com/2673-4591/56/1/117

NATIONAL AND INTERNATIONAL COMMUNICATIONS

Role of indirect sonication in the reduction of ohmic resistance in membraneless electrolysis for hydrogen production, The first National Seminar on Green Chemistry and Natural Products 14-15 mars 2022, El Oued Algeria, https://cgcp.sciencesconf.org/

A parametric study of an alkaline sono-electrolysis system for hydrogen production, International Congress of Energies and Engineering of Industrial Processes CEGPI'22, 23 - 25 May 2022, Algiers Algeria, https://iceipe-usthb-dz.com/Cegpi22En

Green hydrogen from a PV-supplied sono-electrolysis: modelling and experimental investigations of the mechanism and performance, International Conference on Research in Engineering, Technology and Science, 06-09 July 2023, Budapest Hungary https://www.2023.icrets.net/pages/19/call-for-paper?l=

Comprehensive modelling study of the electrical performance of a sono-electrolyzer under a voltage and current sources supply: from grey to green hydrogen, International Conference on Research in Engineering, Technology and Science, 06-09 July 2023, Budapest Hungary, https://www.2023.icrets.net/pages/19/call-for-paper?l=

Hydrogen generation from MBR permeate via ultrasound-assisted membraneless electrolysis, the 5th Euro-Mediterranean Conference on Environmental Integration (EMCEI-2023), 02-05 October, Rende Italy, https://emcei.net/2023/

Dynamic Response of a Sono-Electrolyzer under PV Supply for Hydrogen Production: A Modelling Approach for the Kinetic and Energetic Assessment under Northern Algerian Meteorological Conditions, 4th International Electronic Conference on Applied Sciences, 27 Oct-10 Nov 2023, Online, https://sciforum.net/dashboard/author/submissions/0b5cea60eab476708f5c7c6c76162551

ABSTRACT

The aim of the present thesis is to develop an innovative process for the production of green hydrogen from treated wastewater sono-electrolysis, using photovoltaic solar energy and low-cost materials. The thesis combines theoretical and experimental approaches, which focus on membraneless and membrane sono-electrolysis, with a transition from blue to green hydrogen by integrating PV supply. In addition, the project investigates the membrane bioreactor treatment of domestic wastewater for its reuse in hydrogen production and evaluates the purity of the produced gas. Finally, a comparative analysis is carried out to provide insights for scaling up the research results.

At the very beginning, a preliminary parametric study was performed using two configurations, Hoffmann and H-cell, by varying the concentration and the nature of the salt, the solution and bath temperatures and the electrode's material. The parametric study revealed that the integration of continuous sonication prevents high temperature operation. The H-cell experiments highlighted the significant influence of cell geometry on ion transport phenomena, while the sono-electrolytic configuration showed a dependency on the electrolyte type, with NaOH facilitating bubble formation and degassing. Continuous sonication offered the highest improvement in kinetics and energy efficiency, with the greatest reduction in bubble resistance observed with nickel foam electrodes and KOH electrolyte.

Then, the investigation of the membraneless sonoelectrolytic process using an H-cell configuration and indirect continuous sonication demonstrated experimentally a 3.93% improvement in H_2 rate and a 2.76% gain in energy conversion efficiency with sonication. Polarisation curves showed quasi-linear evolution, indicating an ohmic overpotential zone, with a 7.2% reduction in average ohmic resistance under sonication. At the microscopic scale, numerical simulations proved that small bubbles primarily contribute to shockwave-induced turbulence, which facilitated hydrogen bubble detachment, while large bubbles are more involved in microjetting, both phenomena reduced electrode coverage by bubbles from 76% to 42%, and decreased bubble resistance by 62.35%. Meanwhile, the contribution of the sonochemical activity was negligible.

In terms of membrane sono-electrolysis, the results showed that the Zirfon® separator outperformed other diaphragms/membranes in terms of energy efficiency, hydrogen production kinetics and stability under high alkaline conditions. However, sonication integration didn't improve energy efficiency, yet it enhanced hydrogen production kinetics due to desorption and stirring effects in the electrolyte.

Regarding the coupled PV-sono-electrolysis, Indirect continuous sono-electrolysis had the lowest electrode coverage (37%) and reduced bubble resistance by 76% compared to silent mode and 52% compared to pulsed sonication. The influence of ultrasound on the diffusion coefficient suggested a limited effect on mass transport properties, while the Faraday efficiency remained constant regardless of the presence of ultrasounds. This was confirmed by numerical simulations. Dynamic conditions showed higher hydrogen production in summer, with a notable reduction of ohmic and cell voltages with increased radiation.

The substitution of fresh water by membrane bioreactor permeate passed through the pretreatment process. The membrane bioreactor treatment achieved high COD and TOC removal rates of 96% each. However, additional steps are required to meet ASTM Type II limits for H_2 production. Despite achieving an overall hydrogen purity of 85%, traces of nitrogen and oxygen gases were present within safe limits of the O_2/H_2 ratio. When using a current source with permeate instead of distilled water, the integration of ultrasound didn't improve energy efficiency, but improved hydrogen flow rate due to enhanced desorption, leading to better electrochemical hydrogen production.

Finally, the comparative study made in the last chapter showed that the integration of continuous ultrasound leads to higher improvement in hydrogen flow rate when a voltage source is used, due to reduced ohmic resistance and accelerated kinetics. Hydrogen purity from distilled water was 5% higher than from permeate.

ملخص

الهدف من هذه الأطروحة هو تطوير عملية مبتكرة لإنتاج الهيدروجين الأخضر من التحليل الكهربائي لمياه الصرف الصحي المعالجة باستخدام الطاقة الشمسية الكهروضوئية ومواد منخفضة التكلفة. تجمع الأطروحة بين الأساليب النظرية والتجريبية، التي تركز على التحليل الكهربائي الصوتي الغشائي وغير الغشائي، مع الانتقال من الهيدروجين الأزرق إلى الهيدروجين الأخضر من خلال دمج الطاقة الشمسية الكهروضوئية. بالإضافة إلى ذلك، يبحث المشروع في معالجة مياه الصرف الصحي المنزلية باستخدام المفاعل الحيوي الغشائي لإعادة استخدامها في إنتاج الهيدروجين وتقييم نقاء الغاز المنتج. وأخيرا، يتم إجراء تحليل مقارن لتقديم رؤى لتوسيع نطاق نتائج البحث.

في البداية، تم إجراء دراسة حدودية أولية باستخدام تكوينين، هوفمان وخلية H، عن طريق تغيير التركيز وطبيعة الملح، ودرجات حرارة المحلول والحمام ومواد القطب الكهربائي. كشفت الدراسة الحدودية أن دمج الموجات فوق الصوتية المستمرة يجنب التشغيل بدرجة حرارة عالية. سلطت تجارب الخلايا H الضوء على التأثير الكبير لهندسة الخلية على ظواهر النقل الأيوني، في حين أظهر التتحليل الكهربائي الصوتي التعلق بنوع المنحل، حيث يسهل NaOH تكوين الفقاعات وتفريغ الغاز. أثبت دمج الموجات فوق الصوتية المستمرة أعلى تحسن في الحركية وكفاءة الطاقة، مع أكبر انخفاض في مقاومة الفقاعة التي لوحظت مع أقطاب رغوة النيكل وKOH.

بعد ذلك، أظهر التحقيق في عملية التحليل الكهربائي بالموجات فوق الصوتية باستخدام الخلية H والصوتنة المستمرة غير المباشرة بشكل تجريبي تحسنًا بنسبة 3.93% في تدفق H_2 وزيادة بنسبة 2.76% في كفاءة تحويل الطاقة مع الصوتنة. أظهرت منحنيات الاستقطاب تطورًا شبه خطي، مما يشير إلى وجود منطقة أومية ، مع انخفاض بنسبة 7.2% في متوسط المقاومة الأومية تحت الصوتنة. على المستوى المجهري، أثبتت عمليات المحاكاة العددية أن الفقاعات الصغيرة تساهم في المقام الأول في الاضطراب الناجم عن موجة الصدمة، مما سهل انفصال فقاعة الهيدروجين، في حين أن الفقاعات الكبيرة أكثر مشاركة في النفث الدقيق، وقد خفضت كلتا الظاهرتين تغطية القطب الكهربائي بالفقاعات من 76٪ إلى 42٪، وانخفضت مقاومة الفقاعات بنسبة 62.35%. وفي الوقت نفسه، كانت مساهمة النشاط الكيميائي الصوتي ضئيلة.

فيما يتعلق بالتحليل الكهربائي الصوتي في وجود الغشاء، أظهرت النتائج أن فاصل Zirfon® يتفوق على الأغشية/الفواصل الأخرى من حيث كفاءة الطاقة، وحركية إنتاج الهيدروجين والاستقرار في ظل الظروف القاعدية العالية. ومع ذلك، فإن دمج الصوتنة لم يحسن كفاءة استخدام الطاقة، ولكنه عزز حركية إنتاج الهيدروجين بسبب تأثيرات الامتزاز والتحريك في المنحل بالكهرباء.

فيما يتعلق بالتحليل الكهربائي الصوتي الكهروضوئي المقترن، كان للتحليل الكهربائي الصوتي المستمر غير المباشر أقل تغطية قطبية (37٪) وانخفاض مقاومة الفقاعات بنسبة 76٪ مقارنة بالوضع الصامت و 52٪ مقارنة بالصوتنة النبضية. يشير تأثير الموجات فوق الصوتية على معامل الانتشار إلى وجود تأثير محدود على خصائص النقل الجماعي، في حين ظلت كفاءة فاراداي ثابتة بغض النظر عن وجود الموجات فوق الصوتية. تم تأكيد ذلك من خلال المحاكاة العددية. أظهرت الظروف الديناميكية إنتاجًا أعلى للهيدروجين في الصيف، مع انخفاض ملحوظ في التوتر الأومي وال توتر الخلوي مع زيادة الإشعاع.

يتم استبدال المياه العذبة بمياه الصرف الصحي المعالجة بواسطة المفاعل الحيوي الغشائي من خلال عملية المعالجة المسبقة. حقق العلاج بالمفاعل الحيوي الغشائي معدلات عالية لإزالة COD و TOCبنسبة 96% لكل منهما. ومع ذلك، هناك خطوات إضافية مطلوبة للوفاء بحدود ASTM Type II لإنتاج الهيدروجين. على الرغم من تحقيق نقاء الهيدروجين الإجمالي بنسبة 85%، إلا أن آثار غازات النيتروجين والأكسجين كانت موجودة ضمن الحدود الآمنة لنسبة O_2/ H_2.عند استخدام مياه الصرف الصحي المعالجة بدلاً من الماء المقطر مع مصدر تيار ، فإن دمج الموجات فوق الصوتية لم يحسن كفاءة الطاقة، ولكنه أدى إلى تحسين معدل تدفق الهيدروجين بسبب الامتزاز المعزز، مما يؤدي إلى إنتاج هيدروجين كهروكيميائي أفضل.

وأخيرا، أظهرت الدراسة المقارنة التي أجريت في الفصل الأخير أن دمج الموجات فوق الصوتية المستمرة يؤدي إلى تحسن أعلى في معدل تدفق الهيدروجين عند استخدام مصدر التوتر، وذلك بسبب انخفاض المقاومة الأومية والحركية المتسارعة. كان نقاء الهيدروجين من الماء المقطر أعلى بنسبة 5٪ من مياه الصرف الصحي المعالجة.

RESUME

L'objectif de la présente thèse est de développer un procédé innovant de production d'hydrogène vert à partir de sono-électrolyse des eaux usées traitées, en utilisant l'énergie solaire photovoltaïque et des matériaux peu coûteux. La thèse combine des approches théoriques et expérimentales, axées sur la sono-électrolyse sans membrane et à membrane, avec une transition de l'hydrogène bleu à l'hydrogène vert en intégrant l'alimentation photovoltaïque. De plus, le projet étudie le traitement par bioréacteur à membrane des eaux usées domestiques en vue de leur réutilisation dans la production d'hydrogène et évalue la pureté du gaz produit. Enfin, une analyse comparative est effectuée pour fournir des informations permettant d'étendre les résultats de la recherche.

Initialement, une étude paramétrique préliminaire a été réalisée en utilisant deux configurations, Hoffmann et cellule en H, en faisant varier la concentration et la nature du sel, les températures de la solution et du bain et le matériau de l'électrode. L'étude paramétrique a révélé que l'intégration de la sonication continue permet d'éviter un fonctionnement à haute température. Les expériences sur la cellule H ont mis en évidence l'influence significative de la géométrie cellulaire sur les phénomènes de transport des ions, tandis que la configuration sono-électrolytique a montré une dépendance au type d'électrolyte, avec NaOH facilitant la formation de bulles et le dégazage. La sonication continue a offert la plus grande amélioration de cinétique et d'efficacité énergétique, avec la plus haute réduction de la résistance des bulles observée avec les électrodes en mousse de nickel et l'électrolyte à base de KOH.

Ensuite, l'étude du processus sonoélectrolytique sans membrane utilisant une configuration de cellules H et une sonication continue indirecte a démontré expérimentalement une amélioration de 3,93 % du taux de H_2 et un gain de 2,76 % en efficacité de conversion d'énergie avec la sonication. Les courbes de polarisation ont montré une évolution quasi-linéaire, indiquant une zone de surpotentiel ohmique, avec une réduction de 7,2% de la résistance ohmique moyenne sous sonication. À l'échelle microscopique, des simulations numériques ont prouvé que les petites bulles contribuent principalement aux turbulences induites par les ondes de choc, ce qui facilite le détachement des bulles d'hydrogène, tandis que les grosses bulles sont davantage impliquées dans le microjet. Ces deux phénomènes ont réduit la couverture des électrodes par les bulles de 76 % à 42 % et diminué la résistance des bulles de 62,35 %. Cependant, la contribution de la sonochimie était négligeable. En termes de sono-électrolyse membranaire, les résultats ont montré que le séparateur Zirfon® surpassait les autres diaphragmes/membranes en termes d'efficacité énergétique, de cinétique de production d'hydrogène et de stabilité dans des conditions alcalines élevées. Cependant, l'intégration de la sonication n'a pas amélioré l'efficacité énergétique, mais a amélioré la cinétique de production d'hydrogène en raison des effets de désorption et d'agitation dans l'électrolyte.

Concernant la sono-électrolyse couplée au PV, la sono-électrolyse continue indirecte a présenté la couverture d'électrodes la plus faible (37 %) et a réduit la résistance des bulles de 76 % par rapport au mode silencieux et de 52 % par rapport à la sonication pulsée. L'influence des ultrasons sur le coefficient de diffusion suggère un effet limité sur les propriétés de transport de masse, tandis que l'efficacité de Faraday reste constante quelle que soit l'implication des ultrasons. Cela a été confirmé par des simulations numériques. Les conditions dynamiques ont montré une production de H_2 plus élevée en été, avec une réduction notable des tensions ohmiques et cellulaires sous irradiation accrue.

La substitution de l'eau douce par du perméat de bioréacteur à membrane est passée par le processus de prétraitement. Le traitement par bioréacteur à membrane a permis d'obtenir des taux d'élimination élevés de la DCO et du COT de 96 % chacun. Cependant, des étapes supplémentaires sont nécessaires pour respecter les limites ASTM Type II pour la production de H_2. Malgré une pureté globale de l'hydrogène de 85 %, des traces d'azote et d'oxygène étaient présentes dans les limites sûres du rapport O_2/H_2. Lors de l'utilisation d'une source de courant avec perméat au lieu d'eau distillée, l'intégration des ultrasons n'a pas amélioré l'efficacité énergétique, mais a amélioré le débit de H_2 grâce à une désorption poussée, conduisant à une meilleure production électrochimique de H_2.

Enfin, l'étude comparative réalisée dans le dernier chapitre a montré que l'intégration des ultrasons continus conduit à une amélioration plus importante du débit d'hydrogène lorsqu'une source de tension est utilisée, en raison d'une résistance ohmique réduite et d'une cinétique accélérée. La pureté de l'hydrogène provenant de l'eau distillée était 5 % plus élevée que celle du perméat.

TABLE OF CONTENT

LIST OF FIGURES

LIST OF TABLES

LIST OF ABBREVIATIONS

Symbol	Signification	Unit
ρ_A	Albedo	
v	Jet velocity	m/s
α	Accommodation coefficient	
a_a	Anodic charge transfer coefficient	$A.cm^{-2}$
a_c	cathodic charge transfer coefficient	$A.cm^{-2}$
β	Tilt angle	°
θ	Incident angle	°
σ	Diffusion layer thickness	cm
τ	Tortuosity	
ρ	Material resistivity	Ω.m
δ_a	Anode thickness	cm
δ_c	Cathode thickness	cm
ε_a	Acoustic efficiency	
η_F	Faradaic efficiency	
θ_z	Zenith angle	°
σ_a	Anodic conductivity	$S.cm^{-1}$
σ_{bf}	Bubble-free electrolyte conductivity	$S.m^{-1}$
σ_c	Cathodic conductivity	$S.cm^{-1}$
σ_{dia}	Thickness of the diaphragm	cm
ΔH_j	Reaction heat of the i^{th} reaction	$J.mol^{-1}$
ΔT	Variation in temperature at real and standard conditions	°C
μ	Dynamic viscosity	Pa.s
a	Diode quality factor	
ϑki	stoichiometric coefficient of the kth reactant involved in the i^{th} elementary reaction	
A	Area of the working electrode	cm^2
A_{dia}	Active area of the diaphragm	cm^2
A_f	conductor cross-sectional area.	m^2
B_β	Beam radiation	$W.m^{-2}$
c	Sound celerity	$m.s^{-1}$
C	Concentration of species in the electrolyte	$mol.cm^{-3}$
C_V	Heat capacity	J/mol.K
C_p	Heat capacity	$J.mol^{-1}.K$
d_a	Distance from anode to membrane	m
d_c	Distance from cathode to membrane	m
D_d	Hourly diffuse solar radiation on horizontal surface	$W.m^{-2}$
D_β	Diffuse radiation	$W.m^{-2}$
D_0	Diffusion coefficient	$cm^2.s^{-1}.°C$
e	Percentage of the electrodes surface covered by bubbles	
E_{rev}	Reversible voltage	V
E_{H_2}	Energy conversion efficiency	%
E_{xt}	Extraterrestrial radiation	$W.m^{-2}$
F_i	Number of fractions	

F	Faraday's constant	C/mol
f	Frequency	Hz
f_{Hay}	Anisotropy index	
G_0	Global radiation at standard conditions	$W.m^{-2}$
G	Global radiation	$W.m^{-2}$
H	Hourly global solar radiation on horizontal surface	$W.m^{-2}$
H_{H_2}	Heat of combustion of hydrogen	$mJ.kg^{-1}$
I	Cell current	A
I_a	Anodic current	A
I_{ac}	Acoustic intensity	$W.m^{-2}$
I_c	Cathodic current	A
I_d	Diode current	A
I_{lim}	Limit current of diffusion	A
I_{pv}	Light-generated current of the PV cell	A
I_{pv0}	Photonic current	A
$I_{sc,n}$	Nominal short circuit current	A
I_{sh}	current crossing shunt resistance	A
I_{sh}	Current crossing shunt resistance	A
I_0	Diode saturation current	A
I_{0a}	Anodic exchange currents	A
IEC	Ionic exchange capacity of the membrane	$meq/g_{dry\ membrane}$
K_B	Boltzmann constant	$J.K^{-1}$
K_I	Current coefficient	%/ °C
K_V	Voltage coefficient	%/ °C
l	Length of electron path	m
$\dot{m}$	Rate of evaporation–condensation of liquid	$Kg.m^{-2}.s$
$\dot{m}$	Rate of evaporation–condensation of liquid	$kg.m^{-2}.s$
$\dot{m}_{H_2}$	The mass flow of hydrogen	$g.s^{-1}$
$\ddot{m}$	Acceleration of mass flow of liquid due to evaporation–condensation	$Kg.m^{-2}.s^{-2}$
m_e	Mass of the electrolyte solution	g
M	Electrolyte molarity	mol
M_{H_2}	Molar mass of hydrogen	$g.mol^{-1}$
$M_{e,HCl}$	Moles of HCl after equilibration	mol
$M_{i,HCl}$	Moles of HCl in flask at the start of titration	mol/L
N	Cells number	
P	Acoustic power	W
P_e	Electric energy consumption	w
P_v	Vapor pressures of electrolyte solution	atm
P_v^*	Vapor pressure of purified water	atm
P_∞	Static pressure	Pa
P_A	Acoustic amplitude	Pa
P_{cell}	Consumed power of the cell	W
P_{dia}	Porosity of the diaphragm	%
P_e	Electric energy consumption	W
P_g	Gas pressure	Pa

P_j	Exit jet power	W
P_s	Power of shockwave	W
q	Charge of the electron	C
r_j	Reaction rate of the ith reaction [mol/s	mol.s^{-1}.m^{-3}
r_β	Ratio of hourly radiation	
R	Gas constant	m^2 .kg.s^{-2} .°C^{-1}
$\ddot{R}$	Bubble wall acceleration	m.s^{-2}
$\dot{R}$	Bubble wall velocity [m/s]	m.s^{-1}
R_a	Anodic resistance	Ω
R_b	Bubble resistance	Ω
R_{bf}	Bubble-free electrolyte resistance	Ω
R_c	Cathodic resistance	Ω
R_{cell}	Cell resistance	Ω
$R_{electrical}$	Electrical resistance	Ω
$R_{electrodes}$	Electrode's resistance	Ω
$R_{electrolyte}$	Electrolyte resistance	Ω
$R_{membrane}$	Membrane resistance	Ω
R_{ohm}	Ohmic resistance	Ω
R_p	Shunt resistance	Ω
R_{ra}	Reflected radiation	W.m^{-2}
R_s	Serie resistance	Ω
R_0	Bubble radius	M
S	Surface of the basis of the H-cell electrolyzer	cm^2
S_a	Anode cross section	m^2
S_c	cathode cross section	m^2
t	time	s
T	Solution temperature	°C
T_b	Temperature within the bubble	K
T_n	Temperature at standard conditions	°C
T_p	Panel temperature	°C
$U_{act\,a}$	Anodic activation voltage	V
$U_{act\,c}$	Cathodic activation voltage	V
U_{act}	Activation voltage	V
U_{cell}	Cell voltage	V
U_{conc}	Concentration voltage	V
U_{ohm}	Ohmic voltage	V
V_{ocn}	Nominal open circuit voltage	V
V_t	Thermal voltage at standard temperature	V
V_{tn}	Thermal voltage at standard conditions	V
V	The operating voltage of electrolyzer	V
Wm	Weight of the wet membrane	g

GENERAL INTRODUCTION

GENERAL INTRODUCTION

Hydrogen has attracted worldwide attention as the alternative fuel of the near future, aiming to replace hydrocarbons by a clean energy [1]. Hydrogen is the most abundant element in the universe with high specific energy combustion 140 MJ/Kg, a value that makes of hydrogen a valuable energy carrier [2,3].

Hydrocarbon's reforming is the most widely used and efficient technique to generate hydrogen, due to the low costs of production. However, this method of H_2 synthesis is considered as a polluting technique due to the high emissions of greenhouse gases [3][4]. On the other hand, hydrogen production from water as a feedstock (considered as a green process to generate hydrogen) is based on various techniques such as electrolysis, photolysis and photocatalysis. Photolysis is the process of splitting water into oxygen and hydrogen using light, where the free energy required to split water can be provided in the form of UV-visible electromagnetic radiation emitted by the Sun and reaching the Earth's surface [5]. Photocatalysis as well adopts the same technique where further catalyst is implemented. This catalyst material absorbs light energy and uses it to facilitate the splitting of water molecules into hydrogen and oxygen [6]. Both techniques are known to be simple and require no additional electricity, but the main challenge of photolysis and photocatalysis is the low energy efficiency and availability of catalysts [7].

Hydrogen production from water electrolysis is considered as a promising route for hydrogen generation from water, particularly when it is supplied with renewable sources [8]. This mainly involves solar energy, wind energy and biomass gasification as a sustainable energy sources [9]. Solar supplied hydrogen production and solar hydrogen pathways that include photovoltaic hydrogen generation, photocatalytic, photobiological, solar thermal and photoelectrochemical routes are considered as cost effective routes at large scale [10]. Yet, Photovoltaic electrolysis (PV-EL) has a comparatively high level of technical maturity, however the overall efficiency of the technology is limited owing to the large consumption of electricity [11].

In spite of the wide acknowledgement of the benefits of using renewable energy systems in fighting climate change, there remain some concerns related to these systems, such as the initial high cost, the operating cost of the energy conversion devices and weather dependency [8]. In front of this challenge, numerous researches focused during the last years on the improvement of the overall energy efficiency of the systems [8].

Lately, the application of ultrasound in chemistry, which is known as sonochemistry, has gained considerable interest due to the improvement effects to the process [12]. Water dissociation via electrolysis can be improved by applying acoustic power [13,14]. The research group of Pollet presented pioneering works in this field. They demonstrated that water electrolysis could be enhanced when integrating the sonication into the process [14].

Tens of studies investigated the sono-electrolysis process for hydrogen production and reported the positive effect of ultrasound on increasing the amount of hydrogen production. For instance, Cataldo [15] who was the first to investigate the effect of ultrasound during the electrolysis of aqueous solutions of $NaCl$ and HCl, reported that the application of ultrasound results in the increase of hydrogen production on the cathode and chlorine on the anode. In the same paper, Cataldo [15] assumed that the main phenomena resulting during sonication are degassing activity in the electrode which decreases the accumulation of bubbles in the solution and at the electrode surface [16]. According to Pollet [16], these crucial effects of ultrasound activity contribute to the limitation of the overpotential. Additionally, ultrasound waves and acoustic cavitation bubbles produce depolarization effects, increase of the mass transfer rate, decrease of the double layer thickness [17] and also facilitates the passage of ions through the electrode double layer. Hence, ultrasonic waves encourage species that are adsorbed at the electrode to desorb from the electrode surface, which is the case with graphite electrodes. Thus, the overpotential may be lowered due to the aforementioned effects, resulting in an enhancement in the rate of H_2 generation.

The role of ultrasound was also studied by Li et al. [18] for water electrolysis in alkaline solution and different concentrations of NaOH under 60 KHz and 50 W. It was observed

that applying ultrasound results in an enhancement in the range of 10% to 25% in terms of energy saving and mass transfer and thus an improvement in H_2 production efficiency by a range of 5% to 18% at high current density exceeding 80 mA.cm^{-2}.

McMurray et al. [19] investigated the effect of ultrasound on hydrogen evolution and oxygen reduction by using a titanium sonotrode and graphite electrodes and reported that hydrogen and oxygen evolution increased as a result of the rise of mass transfer and decrease of activation overpotential.

Zadeh [20] investigated the effect of added ultrasound on a conventional alkaline water electrolysis, where it was determined that ultrasound improved the production efficiency by 4.5% and energy efficiency by 1.3%. The introduction of the ultrasound resulted in bubble removal from the surface of the electrode and the electrolyte solution, which prepared the electrode surface for the electrochemical reactions and thus enhanced the hydrogen generation.

When acoustic cavitation bubble oscillates and collapses on the electrode surface, microstreaming and microjets, which are physical effects accompanying the bubble oscillation and collapse, respectively, are believed to contribute significantly to the increase of mass transfer to the electrode surface, electrode surface cleaning and activation [4].

The main objective of the present research project is to develop an innovative process for the generation of green hydrogen based on wastewater sono-electrolysis powered by photovoltaic solar energy and using low-cost materials. The research design focuses on an experimental and modelling study of the effect of sonication on reducing the resistance of water electrolysis to increase its energy efficiency and enhance the kinetics of hydrogen production in the case of DC and PV solar power supply, on one hand, and distilled water and membrane bioreactor treated wastewater, on the other hand. The first chapter is based on a membraneless alkaline sono-electrolysis for hydrogen production, and consists of preliminary experiments aiming to investigate the role of ultrasounds in alkaline sono-electrolysis powered by a voltage source. In this chapter,

we start with a parametric study based on the nature of the salt KOH/NaOH, the electrolyte concentration, the electrolyte temperature, the bath temperature and the electrode material, in order to optimize the conditions for the studies carried out in the following chapters. The optimization is based on the kinetics of hydrogen production as well as the energy efficiency of the process. In the second chapter, a membrane or diaphragm is integrated as a mechanical separator in the electrolytic cell between the anode and cathode compartments, in order to increase the purity of the produced gas. In the second chapter, a theoretical and experimental approaches are combined in order to explain the mechanism of action of ultrasounds at a microscopic scale, as well as its effect on the resistances within the cell at a macroscopic scale. In the third chapter, PV-powered sono-electrolysis for green hydrogen production is studied, in which the voltage energy source is replaced by a photovoltaic power integrated to the processes studied in the previous two chapters under optimal conditions. In addition, a hybrid experimental and theoretical approach is adopted to study the performance of the integrated process under static and dynamic weather conditions. The fourth chapter focuses on the production of green hydrogen from wastewater, alongside the integration of photovoltaic power supply and ultrasounds. In this chapter, the replacement of the fresh water used as electrolyte solvent by treated wastewater goes beyond the replacement of the conventional energy source by a 'green' source. Membrane bioreactor technology is used as treatment process of wastewater, and the performance of the combined process is studied experimentally based on hydrogen production kinetics, process energy efficiency and the purity of the produced gas. From a sustainable development point of view, the aim of this incremental approach is to make the process cleaner and less material and energy intensive. The last chapter consists of a comparative study of hydrogen production from fresh and treated wastewater under conventional and photovoltaic power supply. In this last chapter, a summary of the results is made based on a direct comparison of the results obtained in the previous chapters in terms of kinetics and energy efficiency of the process, as well as the purity of the produced gas, with the aim of deciding on the interest of each

parameter in the integrated process and to give perspectives to the study, in particular for scale-up.

CHAPTER 1

"Membraneless alkaline sono-electrolysis for hydrogen production"

CHAPTER 1: MEMBRANELESS ALKALINE SONO-ELECTROLYSIS FOR HYDROGEN PRODUCTION

1.1 Introduction

Among the different ultrasound-based techniques for hydrogen generation, sonoelectrolysis is the technique known as associating ultrasound to electrolysis. This technique proved to be efficient by several researchers. Pollet is the pioneering researcher in the field of sonoelectrolysis, Pollet and coworkers presented numerous works to explain the impact of ultrasounds on the reduction of the overpotential and the drop of ohmic voltage, which conducts to higher hydrogen generation rates [4,13,16]. Pollet [16] reported in a book entitled "Power Ultrasound in Electrochemistry: From Versatile Laboratory Tool to Engineering Solution" the application of ultrasound power in electrochemistry. Pollet discussed, reviewed and analyzed the different works and results of sonoelectrolysis and highlighted the role of ultrasound waves in the decrease of overpotential. Similarly, Islam et al. [4], from the same research group, presented the sonoelectrochemical pathway for hydrogen production and explained how does ultrasound influence the mass transport and electrodes cleaning through the combined effect of microjets and microstreaming as well as the drop of the overall potential that is caused by the degassing effects and/or the modifications of the electrodes surface [21]. Islam suggested deeper investigations of H_2 quantification for a better comprehension of the impact of different parameters of sonoelectrochemistry for hydrogen production, for the upgrade of the process. Cataldo [15] was one of the first to study the effect of ultrasound on water electrolysis for hydrogen production. Using different solutions of 6M NaCl, 6M HCl and acidified solution of 0.5NaCl/1.1 HCl under 30 kHz. It was found that the presence of ultrasound increased the rate of chloride and hydrogen gases due to the induced degassing effect. Walton et al. [17] used 38 kHz of ultrasound frequency to study its effect on hydrogen evolution from 1 M H_2SO_4 solution at a platinized platinum electrode. In their study, Walton et al.[17] reported that the effect of sonication on the removal of gases from the electrode surface improves the rate of hydrogen evolution. This positive effect of ultrasound on

hydrogen evolution during electrolysis was also proved by Mc Murray et al.[19], who used a 20 kHz and 26W/cm^2 ultrasound generator at a titanium tip sonotrode. In their study, McMurray et al. [19] assumed that the enhancement in hydrogen evolution and oxygen reduction is mainly caused by the enhancement of mass transport. Budischak et al.[22] coupled a 42 kHz and 300 W ultrasound generator with KOH electrolysis using platinum electrodes. The results showed that ultrasound increased the efficiency of the electrolyzer, especially at intermediate current densities.

Li et al.[18] exposed water alkaline solutions of different concentrations of NaOH (0.1, 0.5 and 1 M) at a RuO_2 and IrO_2 plated Ti electrode. Their study demonstrated that an enhancement in the efficiency of hydrogen generation of the order of 5% to 18% is achieved. Moreover, 10% to 25% of energy consumption was saved at high current densities and lower electrolyte concentrations. Similar studies were conducted by Symes [23] and Zadeh [20] under 20 kHz from mild acidic (H_2SO_4) and alkaline solutions (KOH and NaOH) at different electrode materials (platinum, glassy carbon, industrial carbon, 316 stainless steel and nickel based electrodes). The results of both studies showed an enhancement in hydrogen production due to the increase of mass transport, electrodes cleaning and degassing. Zadeh [20] observed an improvement in H_2 generation of 14% and 25% for NaOH and KOH, respectively, when coupling ultrasound to electrolysis process.

Lin et al. [24] investigated the polarization impedance phenomenon in water sonoelectrolysis at different concentrations of KOH solution, using nickel electrodes. The study revealed that the sonoelectrolysis process is mainly affected by the ultrasonic power, electrode gap, and electrolyte concentration. The sonication proved to reduce the concentration polarization and increases the mass transfer. In the same study, Lin et al. [24] highlighted the importance of lowering the consumption of electric power and invoked economic power efficiency, they concluded that even though the integration of an ultrasound field in electrolysis requires more material, it still increases the efficiency of hydrogen production and decreases energy consumption.

The analysis of the presented setups reveals that direct sonication is usually used in sonoelectrolysis. However, each configuration has its particularity and consequently its intrinsic effect on the process. For instance, the physical separation of the anodic and cathodic compartments in the first configuration [20] improves the purity of the produced hydrogen, however, it limits the passage of ions within the electrolytic solution and hence reduces the overall efficiency of the process. On the other hand, the absence of the physical separation influences negatively the purity of hydrogen and may create HHO mixtures (Hydrogen-Hydrogen-Oxygen, which is a mixture of hydrogen and oxygen gases, usually in a 2:1 ratio) at industrial scale.

Furthermore, in configuration [18], the horizontal placement of the ultrasonic transducer reduces the bubble detachment from the electrode surface as well as the diaphragm's life time due to the direct exposition of the diaphragm to the ultrasound action and risk of erosion. To ensure an effective removal of bubbles from the electrode surface, the vertical configuration is preferred in such situation.

Overall, it was proved from the sonoelectrolysis studies that the effects of ultrasound in the improvement of hydrogen production yield are rather of physical nature. Therefore, there is an agreement that in the case of sonoelectrolysis, the combination of ultrasound irradiation enhances mass transfer [19], bubble detachment from electrodes surface [17,18,22] degassing effect [25], and desorption effect [16].

In the present chapter, a parametric study of an alkaline water sono-electrolysis for hydrogen production is conducted using two configurations of electrolyzer. The first configuration is a Hoffman setup used as a preliminary experimental study in order to observe the effect of indirect sonication on membraneless water sono-electrolysis process. The second configuration uses an H-cell setup. The parametric study covers the nature of the dissolved salt (KOH and NaOH), the concentration of the salt in the electrolyte (2.67, 3.56, 4.46, 5.35, 6.24, 7.13 mol/ L), the electrolyte and the bath temperatures (27, 40, 45, 50, 55 and 60°C), and the electrode's nature in terms of material and microstructure (stainless steel 304 plate using the Hoffmann cell, and stainless steel 304 plate, nickel plate, nickel foam, and graphite using the H-cell setup).

These parameters are investigated in terms of energy conversion efficiency and hydrogen production kinetics. Ultrasounds power is integrated after the parametric optimization of the electrolytic process. The effect of acoustic power is then studied at the optimum conditions using two modes of sonication, namely continuous and pulsed modes, in order to take advantage of the physical effects of ultrasounds. The main objective of the study is to assess the effect of ultrasounds in the combined sono-electrolysis process in terms of kinetics of hydrogen production and energy efficiency, in order to highlight the extent of this effect and whether an upscaling of the process would be worthy, and identify the actual limitations in terms of energy and kinetics. On the other hand, the study aims to quantify the eventual effect of pulsed and continuous sonication in an alkaline electrolysis system under various configurations, and elucidate the mechanism behind their effects.

1.2 Experimental procedure

1.2.1 Silent membraneless alkaline electrolysis: experimental investigation

1.2.1.1 Electrolysis setup

a) Hoffmann cell

The configuration of the Hoffmann cell [26] consists of two graduated tubes connected to a three neck flask, with an open tube placed vertically in the middle, as shown in Fig.1(a). The experiments carried out with the Hoffmann cell serve as preliminary tests aiming to observe the effect of sonication on the kinetics of production of hydrogen and energy conversion efficiency. Each experiment is conducted in a volume of 350 mL of degassed alkaline solution of either KOH or NaOH. Stainless steel 304 electrodes with a surface of 12 cm^2 (effective contact surface of 24 cm^2) are placed at the bottom of each lateral graduated tube, at a distance of 8 cm from each other, as presented in Fig.1(a). The series of experiments is based on an incremental approach considering the variation of the concentration of the dissolved salt in the electrolyte, the variation of the solution temperature based on the optimal concentration of the electrolyte, and the variation of the bath temperature, as reported in Table 1-1.

Table 1-1 *Adopted parameters and their variation using the Hoffmann setup*

Parameter	Variations
Electrolyte type	KOH, NaOH
Electrolyte concentration (mol/L)	2.67, 3.56, 4.46, 5.35, 6.24, 7.13
Temperature of the electrolyte (°C)	Ambient, 40, 45, 50, 55, 60
Temperature of the bath (°C)	Ambient, 40, 45, 50, 55, 60
Electrodes' material (1.2 ×10 cm^2)	Stainless steel 304
Sonication mode	Continuous

b) H-cell

A volume of 300 mL of alkaline degassed solution of KOH/NaOH is used to perform the parametric study and optimize water electrolysis and sono-electrolysis system based on the kinetics of hydrogen production and the energy conversion efficiency. The configuration consists of two cylindrical compartments connected through two horizontal tubes attached to each other using a plier and taking an H form, as depicted in Fig 1.1(b). Each electrode is placed in one side of the cell at a distance of 5 cm. The same effective contact surface of 6.75 cm^2 is used for all the experiments carried out with the H-cell setup. The cell is equipped with a thermometer and placed in a water bath in order to monitor and maintain a stable temperature.

The parametric analysis is realized using the H-cell setup, the geometry of the cell allows the physical separation the two compartments (anode and cathode) of the electrolyzer. Similarly, to the experiments conducted with the Hoffmann setup, the distilled water is degassed for 5 min, then the study starts with the variation of the concentration of the electrolyte (KOH/ NaOH) using stainless steel, nickel, nickel foam and graphite electrodes. This choice is based on the popularity and availability of the materials, their low cost, particularly for graphite, which is a carbon material that is less popular in the literature [27], in addition to the recognized high activity of the nickel [27,28]. The optimal concentration of the alkaline electrolyte is chosen to study the impact of the solution and bath temperatures. The values of the studied parameters are reported in Table 1-2. After optimizing the previous parameters, a series of three

repetitive experiments are performed under optimal parameters, in order to study the kinetics of hydrogen production and the energy conversion efficiency.

Table 1-2 *Adopted parameters and their variation using the H-cell setup*

Parameter	Variations
Electrolyte type	KOH, NaOH
Electrolyte concentration (mol/L)	2.67, 3.56, 4.46, 5.35, 6.24, 7.13
Temperature of the electrolyte (°C)	Ambient, 40, 45, 50, 55, 60
Temperature of the bath (°C)	Ambient, 40, 45, 50, 55, 60
Electrodes' material (1.5×4.5 cm^2)	Stainless steel 304, Graphite, Nickel, Nickel foam
Sonication mode	Continuous, pulse

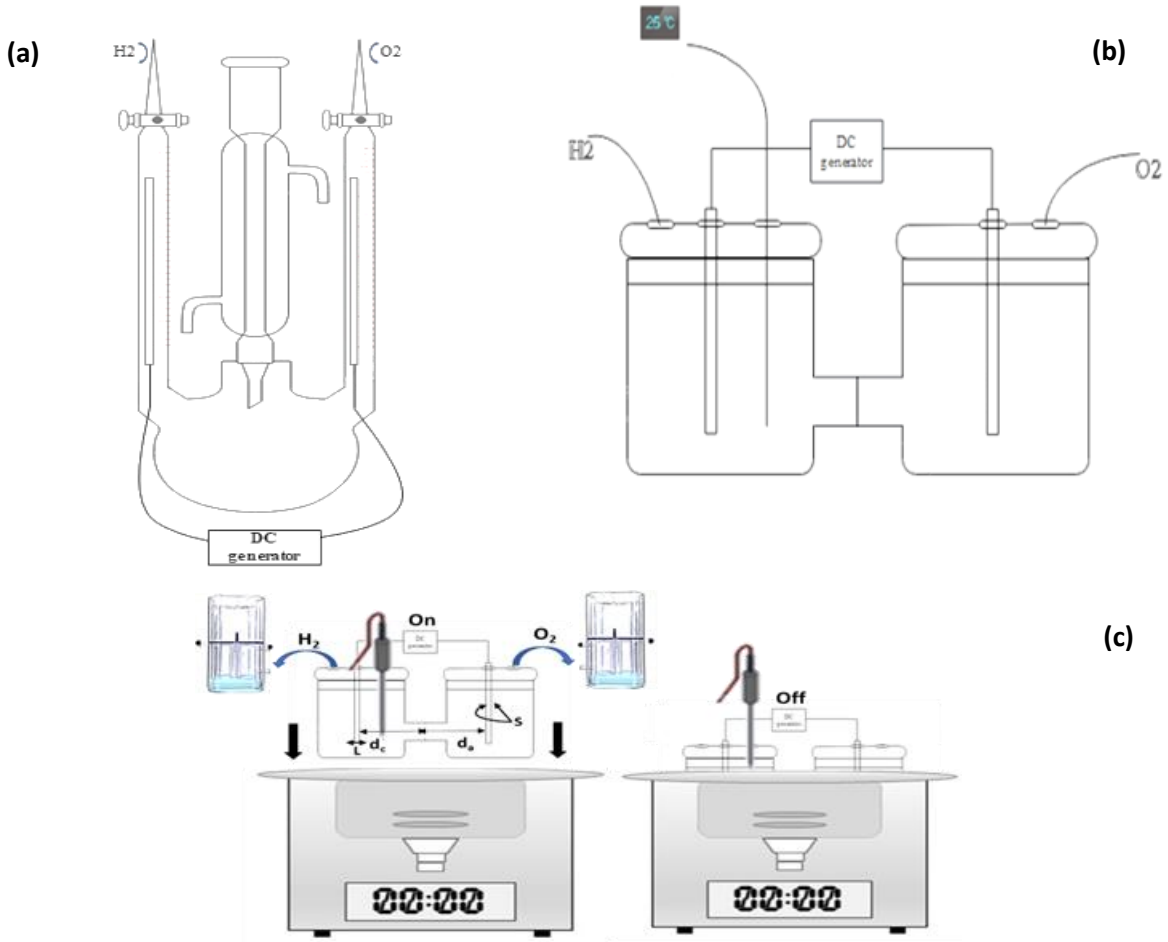

Figure 1.1 Schemas of the Hoffmann setup (a), the H-cell setup (b) and representation of the indirect sonication modes (continuous and pulsed).

1.2.1.2 Sonication setup

An ultrasonic bath of 40 kHz frequency is used as a source of indirect sonication with two modes: continuous and pulsed. The setup is shown in Fig.1.1 (c). The electric power

input of the sonicator P_e is equal to 60 W. The effectiveness of the acoustic power is assessed through a calorimetric measurement. During the sonication of the electrolyte, the temperature increases owing to the propagation of ultrasound waves and the formation of cavitation. The variation of the temperature is monitored using a thermocouple. Supposing that the acoustic energy due to the ultrasonic waves is totally dissipated as heat, the acoustic transmitted power is evaluated from the rate of temperature rise as given in Eq 1.1 [29].

$$P = m_e C_p \frac{dT}{dt} \tag{1.1}$$

Where m_e represents the mass of the electrolyte solution and C_p is the heat capacity of the electrolyte at constant pressure. Therefore, the acoustic efficiency ε_a is evaluated in continuous mode according to Eq 1. 2

$$\varepsilon_a = \frac{P}{P_e} \tag{1.2}$$

The effect of sonication on the sono-electrolysis of water is studied using both continuous and pulsed mode. The kinetics of hydrogen production and the energy efficiency of the sono-electrolysis are monitored in both cases, considering the effective time of sonication, and the On/Off periods (8s on/ 3s off) over the pulsed mode.

1.3 Modeling and simulation procedure

1.3.1 Water electrolysis

In aqueous solution, the passage of the direct current between the two electrodes (anode and cathode) leads to the dissociation of water molecules into hydrogen and oxygen [30]**.** In alkaline conditions, the reduction of water takes place at the cathode through the Eq 1. 3. While hydroxide oxidation occurs at the anode through the Eq 1. 4 [31].

Cathode: $2H_2O + 2e^- \rightarrow H_2 + 2OH^-$ (1.3)

Anode: $2OH^- \rightarrow \frac{1}{2}O_2 + 2e^- + H_2O$ (1.4)

1.3.2 Thermodynamic modelling of alkaline electrolyzer

The cell voltage presents the sum of different voltages involved in the cell and is expressed according to the Eq 1. 5 [32].

$$\mathrm{U_{cell}} = \mathrm{E_{rev}} + \mathrm{U_{act}} + \mathrm{U_{Ohm}} + \mathrm{U_{Conc}} \tag{1.5}$$

Reversible voltage

E_{rev} in the equation above represents the reversible voltage which is the lower voltage required for the electrolysis to occur theoretically, expressed via Eq 1. 6 .

$$E_{rev}(T,P) = E_{rev}(T) + \frac{RT}{ZF}\ln\left(\frac{{P_v}^*(\mathrm{P}-P_v)^{1.5}}{P_v}\right) \tag{1.6}$$

Where Z is the number of moles of electrons transferred in the reaction ($Z = 2$ for hydrogen), F is the Faraday's constant cm/mol, P_v and ${P_v}^*$ are vapor pressures of electrolyte solution and purified water, respectively, in atm as given in Table.1, and $E_{rev}(T)$ is the reversible voltage depending on the temperature that can be expressed according to Eq 1. 7. [33]

$$E_{rev}(T) = 1.5184 - 1.5423\times10^{-3}T - 9.524\times10^{-5}\,T\,ln\,T + 9.84\times10^{-8}T^2 \tag{1.7}$$

Activation voltage

The second term of the cell voltage expressed in Eq 1. 5 is the activation voltage, related to the electrochemical kinetics of the reaction [34]. The activation voltage can be obtained using the Tafel equation [35], as shown in Eq 1. 8, Eq 1. 9 and Eq 1. 10.

$$U_{act\,a} = \frac{2.3026\,RT}{ZFa_a}\log\left(\frac{I_a}{I_{0a}}\right) \tag{1.8}$$

$$U_{act\,c} = \frac{2.3026\,RT}{ZFa_c}\log\left(\frac{I_c}{I_{0c}}\right) \tag{1.9}$$

$$U_{act} = U_{act\,a} + U_{act\,c} \tag{1.10}$$

I_{0a} and refer to the anodic and cathodic exchange currents, respectively, deduced from the anodic and cathodic exchange current densities given in Table 1-3. a_a and a_c are

the anodic and cathodic charge transfer coefficient, respectively, reported in the same table.

Ohmic voltage

The ohmic voltage is due to the ohmic losses during water electrolysis, caused by the formation of the gas bubble, the wastage of electrical energy and the passage of ions in the electrolyte [36]. The ohmic voltage is given according to the ohm's law in Eq 1. 11 [36].

$$U_{ohm} = I \times R_{ohm} \tag{1.11}$$

Where I is the current passing through the cell, and R_{ohm} refers to the ohmic resistance written as the sum of ion resistance, electrical and bubbles resistance according to the Eq 1. 12 [30,36].

$$R_{ohm} = R_{cell} + R_{electrodes} + R_{electrolyte} + R_{electrical} \tag{1.12}$$

As the system is membraneless, the cell resistance refers here to the resistance induced by the geometry of the H-cell (having a passage section between the anodic and cathodic compartments of 1.5 cm diameter), while the membrane resistance involved in the cell resistance $R_{membrane}$ is zero. The three other terms of Eq 1.12 represent respectively the resistance due to the electrodes' materials, $R_{electrodes}$, the electrolyte resistance, $R_{electrolyte}$. and the resistance due to external wires responsible of the transfer of electrons throughout the external circuit,$R_{electrical}$. They are given as follows in Eq 1. 13, Eq 1. 14 and Eq 1. 15.

$$R_{electrode} = R_a + R_c = \frac{\delta_a}{\sigma_a} + \frac{\delta_c}{\sigma_c} \tag{1.13}$$

$$R_{electrolyte} = R_{bf} + R_b \tag{1.14}$$

$$R_{ele} = \frac{\rho l}{A_f} \tag{1.15}$$

In Eq. 1.14, the bubble-free electrolyte resistance R_{bf} can be obtained using Eq 1. 16 [37].

$$R_{bf} = \frac{1}{\sigma_{bf}}\left(\frac{d_a}{S_a} + \frac{d_c}{S_c}\right) \tag{1.16}$$

With S_a and S_c the anode and cathode cross sections, respectively, d_a and d_c present the distances from anode and cathode, respectively, to the membrane (if present). σ_{bf} presents the bubble-free electrolyte conductivity, which can be calculated for an aqueous solution of KOH as a function of the electrolyte molarity M (mol. L^{-1}) and the temperature T (K) according to Eq 1. 17 [37]

$$\sigma_{bf} = -204.1M - 0.28M^2 + 0.5332(M \times T) + \frac{20720M}{T} + 0.1043M^3 - 0.00003(M^2 \times T^2) \quad (1.17)$$

Bubble resistance R_b is expressed as of a fraction of the bubble free electrolyte resistance, following Eq 1. 18 [38].

$$R_b = R_{bf}\left(\frac{1}{\left(1-\frac{2}{3}e\right)^{1.5}} - 1\right) \quad (1.18)$$

Where e is the percentage of the electrodes surface covered by bubbles.

Concentration voltage

The concentration voltage is due to the variation in the concentration of reactant on the electrode surface that is caused by the mass transport. The concentration voltage is expressed according to Eq 1. 19 [32].

$$\mathrm{U_{conc}} = \frac{\mathrm{RT}}{\mathrm{ZF}}\left(\ln\left(1-\left(\frac{\mathrm{I}}{\mathrm{I_{lim}}}\right)\right)\right) \quad (1.19)$$

Where I_{lim} is the limit current of diffusion given as in Eq 1. 20 [16]:

$$I_{lim} = \frac{ZFAD_0C}{\sigma} \quad (1.20)$$

D_0 is the diffusion coefficient cm^2/s, C is the is the concentration of the species in the bulk solution mol/cm^3, σ is the diffusion layer thickness and A is the area of the working electrode given in cm^2.

Table 1-4 *Technical characteristics related to the alkaline water sono-electrolyzer*

Parameter	Value	Reference
Sonicated cell area (2 compartments' sections)	12.56 cm^2	Experiment
Cell temperature	25 °C	Experiment
Anodic exchange current	10^{-7} A/cm^2	[32]
Cathodic exchange current	10^{-1} A/cm^2	[32]
Anodic charge transfer coefficient	0.857	[30]
Cathodic charge transfer coefficient	0.214	[30]
Electrolyte type	KOH	Experiment
Electrolyte concentration C	25% w/w, 4.46 M	Experiment
Electrodes' material and structure	Nickel plate	Experiment
Anode cross section S_a	13.5×2 cm^2	Experiment
Cathode cross section S_c	13.5×2 cm^2	Experiment
Distance from anode to membrane d_a	2 cm	Experiment
Distance from cathode to membrane d_c	2 cm	Experiment
Ionic conductivity of the electrolyte σ_{el}	602.3 $mS.cm^{-1}$	Experiment
Diffusion coefficient D_0	5.1×10^{-5} $cm^2.s^{-1}$	[39]
Diffusion layer thickness σ	0.05 cm	[39]
Anodic exchange current density J_{0a}	2.82×10^{-6} A/cm^2	[40]
Cathodic exchange current density J_{0c}	3.55×10^{-5} A/cm^2	[41]
Vapor pressures of electrolyte solution P_v	0.0204 atm	[33]
Vapor pressures of purified water P_v^*	0.0309 atm	[33]
Type of sonication	Indirect	Experiment
Mode of sonication	Continuous and pulsed	Experiment
Model of the sonicator	Ultrasonic bath	Experiment
Frequency of the ultrasonic wave	40 kHz	Experiment
Electrical power of the sonicator	60 W	Experiment

1.3.3 Water sono-electrolysis

The integration of sonication in water electrolysis process contributes to the efficient detachment of bubbles from the electrodes surface, and enhances the mass transfer allowing the reduction of bubble and ion resistances [3,25]. Hence, the role of sonication will be tackled by the numerical model through the modification of the percentage of electrodes' surface covered by bubbles, e, directly affecting the bubble resistance and hence the ohmic resistance.

1.3.4 Kinetics of hydrogen production

The rate of hydrogen gas produced by water electrolysis is equivalent to the electrical charge consumed by the cell as expressed by the Faraday's law in Eq 1. 21 [42].

$$\dot{m}_{H_2} = \frac{NIM_{H_2}}{ZF}\eta_F \tag{1.21}$$

Where $\dot{m}_{H_2}$ is the mass flow of hydrogen production by the electrolyzer in g/s, M_{H_2} and N is the cells number of electrolyzer and molar mass respectively and η_F represents the Faraday efficiency.

1.3.5 Energy conversion efficiency

The energy conversion efficiency is assessed according to the Eq 1. 22 [29].

$$E_{H_2} = \frac{\dot{m}_{H_2} H_{H_2}}{U_{cell} \times I} \tag{1.22}$$

Where $H_{H2} = 142\ MJ/Kg$

1.3.6 Calorimetric characterization

In order to assess the acoustic power transferred to the bulk volume of the electrolyte, a blank test has been performed using the ultrasonic bath (40 kHz, 60 W). The electrolyzer vessel (H-cell) has been emerged within the ultrasonic bath filled of water, a temperature probe has been introduced within the sealed electrolyzer and immersed into 250 mL of KOH electrolyte (25% wt%). Continuous sonication has been turned on while the chronometer has been launched. The increase of the electrolyte temperature has been recorded as a function of time in the absence of electrolysis. This increase is supposed to originate from the sonication, with the assumption that all the energy

carried by the ultrasonic wave and implicated in acoustic cavitation phenomenon is recovered as heat [43–45]. Hence, the ultrasonic power transmitted to the electrolyte is evaluated through Eq 1. 1 [29,43,45]:

The acoustic power P is related to the acoustic amplitude P_A through Eq 1. 23 [46].

$$P = \frac{{P_A}^2 S}{2\rho_{el} c} \tag{1.23}$$

Where S is the surface of the basis of the H-cell electrolyzer crossed by the ultrasonic wave ($S = 25.12\ cm^2$).

The acoustic intensity received by the H-cell vessel is then expressed as indicated in Eq 1. 24.

$$I_{ac} = \frac{P}{S} \tag{1.24}$$

1.3.7 Microscopic effect of sonication

The integration of sonication in water electrolysis process contributes to the efficient detachment of bubbles from the electrodes surface, and enhances the mass transfer allowing the reduction of bubble and ion resistances. In order to figure out the mechanism of acoustic cavitation bubbles in the sono-electrolysis process, the dynamics of single acoustic bubble and its associated physical effects are modeled and simulated under the acoustic conditions of the experiments described in section 1.3.6 (f, P_A). The motion of the acoustic bubble wall is described by the modified Keller Miksis equation given in Eq 1. 25 , considering the flow of evaporated and condensed water molecules at the bubble interface.

$$\ddot{R} - \frac{(c+\dot{R})}{\rho_{el}\left(cR - \dot{R}R + \frac{\dot{m}R}{\rho_{el}}\right) + 4\mu}\left(P_g - \frac{26}{R} - 4\mu\frac{\dot{R}}{R} - P_\infty + P_A sin\left(2\pi f\left(t + \frac{R}{c}\right)\right)\right) \quad (1.25)$$

$$= \frac{R}{\rho_{el}\left(cR - \dot{R}R + \frac{\dot{m}R}{\rho}\right) + 4\mu}\left(\frac{dP_g}{dt} + \frac{26\dot{R}}{R^2} + 4\mu\frac{\dot{R}^2}{R^2}\right)$$

$$- \frac{\rho_{el}\left((3c - \dot{R}) + \frac{2\dot{m}}{\rho_{el}}\right)\dot{R}^2}{2\left(\rho_{el}\left(cR - R\dot{R} + \frac{\dot{m}R}{\rho_{el}}\right) + 4\mu\right)}$$

$$+ \frac{\dot{m}\left(cR - R\dot{R} + \frac{\dot{m}R}{\rho_{el}}\right)}{\rho_{el}\left(cR - R\dot{R} + \frac{\dot{m}R}{\rho_{el}}\right) + 4\mu} + \frac{\dot{m}\left(c\dot{R} + \frac{\dot{m}}{2\rho_{el}}(c+\dot{R})\right)}{\rho_L\left(cR - R\dot{R} + \frac{\dot{m}R}{\rho_{el}}\right) + 4\mu}$$

The physical kinetics of evaporation and condensation of water molecules at the bubble interface evolves in function of time during both expansion and collapsing phases according to the Hertz Knudsen equation as shown in Eq 1. 26 .

$$\dot{m} = \frac{\sqrt{M_{H_2O}}}{\sqrt{2\pi R_g}}\alpha\frac{1}{\sqrt{T}_b}(P_v - P_{H2O}) \quad (1.26)$$

Where is the accommodation coefficient [47], presented by Yasui [48] and shown in Eq 1. 27.

$$\begin{aligned} &\alpha = 0.35 \quad \text{for } T_b \leq 350 \\ &\alpha = 0.35 - 0.05\left(\tfrac{T_b}{50} - 7\right)^2 + 0.025\left(\tfrac{T_b}{50} - 7\right)\left(\tfrac{T_b}{50} - 8\right)\left(\tfrac{T_b}{50} - 9\right) \quad \text{for } 350 \leq T_b \leq 500 \text{ K} \\ &\alpha = 0.05 \quad \text{for } T_b \geq 500 \end{aligned} \quad (1.27)$$

The energy balance applied to the acoustic cavitation bubble accounts for the heat exchange due to the flow of evaporated and condensed water molecules at the bubble interface, the heat diffusion across the bubble wall and the endothermic and exothermic nature of the chemical reactions evolving inside the bubble volume at collapse. The temperature and the pressure will be governed by Eq 1. 28 and Eq 1. 29, respectively.

$$-P_g 4\pi R^2 \dot{R} - \frac{1}{3}\sum_{j=1}^{N} \Delta H_j r_j 4\pi R^3 + 4\pi R^2 \frac{\dot{m}}{M_{H_2O}} C_{V_{H_2O}} T_b = \frac{\lambda}{\xi} 4\pi R^2 (T_b - T_\infty) + \sum_{i=1}^{K} n_i \, C_V \dot{T}_b \quad (1.28)$$

$$P_g = \frac{\sum_{i=1}^{K} n_i \, R_g T_\infty}{\frac{4}{3}\pi R^3} \quad (1.29)$$

When the bubble collapses, a spherical shockwave is emitted from the bubble in the liquid, and can be responsible of dispersion in the medium, mass transfer and modification of the transport properties. The power emitted by the single acoustic cavitation bubble in the form of a shockwave P_s is expressed by Eq 1. 30.

$$P_s = \frac{4\pi\rho_L}{c}\left(R^2\ddot{R} + 2R\dot{R}^2\right)^2 \quad (1.30)$$

Besides, when the bubble collapses near to a solid surface (the electrodes in sono-electrolysis), it loses its sphericity. A change of the shape of the bubble occurs, from the original approximate sphere to a slender shape and then flattened. Finally, a microjet breaks the bubble wall near the solid and impacts towards it. According to the ultrasonic cavitation phenomenon, micro-jet velocity is given by Eq 1. 31 [49].

$$v = 8.97\left(\frac{R}{R_0}\right)^2 \sqrt{\frac{P_\infty + P_A \sin(2\pi f t) - P_v}{\rho_L}} \quad (1.31)$$

The exit jet power P_j is then given in Eq 1. 32 as a function of the jet velocity [50,51].

$$P_j = \frac{1}{8}\pi\rho_L h^2 v^3 \quad (1.32)$$

The sonochemical pathway of hydrogen production [2] under the conditions of sonication is also investigated in order to assess its contribution in the production of hydrogen. The following chemical mechanism, reported in Table 1-5, is considered to occur within the single acoustic cavitation bubble, behaving as a microscopic reactor with variable volume, temperature and pressure, described respectively in Eq. 25, 28 and 29.

Table 1-5 *Chemical scheme containing the possible elementary reactions resulting of the cleavage of water under air atmosphere inside a single acoustic cavitation bubble* [52].

i	Reaction i	Third body coefficient	A_i	b_i	E_i/R_g (K)	ΔH_i (kJ/mol)
1	$H + O_2 \rightarrow O + {}^{\bullet}OH$	-	1.92×10^{8}	0	8270	69,17
2	$O + H_2 \rightarrow H^{\bullet} + {}^{\bullet}OH$	-	5.08×10^{-2}	2.67	3166	8,23
3	${}^{\bullet}OH + H_2 \rightarrow H^{\bullet} + H_2O$	-	2.18×10^{2}	1.51	1726	−64,35
4	${}^{\bullet}OH + {}^{\bullet}OH \rightarrow H_2O + O$	-	2.1×10^{2}	1.4	200	−72,59
5	$H_2 + M \rightarrow H^{\bullet} + H^{\bullet} + M$	H_2: 2.5, H_2O: 16.0	4.58×10^{13}	−1.4	52500	444,47
6	$O + O + M \rightarrow O_2 + M$	H_2: 2.5, H_2O: 16.0	6.17×10^{3}	−0.5	0	−505,4
7	$O + H^{\bullet} + M \rightarrow {}^{\bullet}OH + M$	H_2O: 5.0	4.72×10^{5}	−1.0	0	−436,23
8	$H^{\bullet} + {}^{\bullet}OH + M \rightarrow H_2O + M$	H_2: 2.5, H_2O: 16.0	2.25×10^{10}	−2.0	0	−508,82
9	$H^{\bullet} + O_2 + M \rightarrow HO_2{}^{\bullet} + M$	H_2: 2.5, H_2O: 16.0	2.00×10^{3}	0	−500	−204,8
10	$H^{\bullet} + HO_2{}^{\bullet} \rightarrow O_2 + H_2$	-	6.63×10^{7}	0	1070	−239,67
11	$H^{\bullet} + HO_2{}^{\bullet} \rightarrow {}^{\bullet}OH + {}^{\bullet}OH$	-	1.69×10^{8}	0	440	−162,26
12	$O + HO_2{}^{\bullet} \rightarrow O_2 + {}^{\bullet}OH$	-	1.81×10^{7}	0	−200	−231,85
13	${}^{\bullet}OH + HO_2{}^{\bullet} \rightarrow O_2 + H_2O$	-	1.45×10^{10}	−1.0	0	−304,44
14	$HO_2{}^{\bullet} + HO_2{}^{\bullet} \rightarrow O_2 + H_2O_2$	-	3.0×10^{6}	0	700	−175,35
15	$H_2O_2 + M \rightarrow {}^{\bullet}OH + {}^{\bullet}OH + M$	H_2: 2.5, H_2O: 16.0	1.2×10^{11}	0	22900	217,89
16	$H_2O_2 + H^{\bullet} \rightarrow H_2O + {}^{\bullet}OH$	-	3.2×10^{8}	0	4510	−290,93
17	$H_2O_2 + H^{\bullet} \rightarrow H_2 + HO_2{}^{\bullet}$	-	4.82×10^{7}	0	4000	−64,32
18	$H_2O_2 + O \rightarrow {}^{\bullet}OH + HO_2{}^{\bullet}$	-	9.55	2	2000	−56,08
19	$H_2O_2 + {}^{\bullet}OH \rightarrow H_2O + HO_2{}^{\bullet}$	-	1.00×10^{7}	0	900	−128,67
20	$O_3 + M_1 \rightarrow O_2 + O + M_2$	M_1 O_2: 1.64; M_2 O_2: 1.63, H_2O: 15	2.48×10^{8}	0	11430	109,27
21	$O_3 + O \rightarrow O_2 + O_2$	-	5.2×10^{6}	0	2090	−396,14
22	$O_3 + {}^{\bullet}OH \rightarrow O_2 + HO_2{}^{\bullet}$	-	7.8×10^{5}	0	960	−164,92
23	$O_3 + HO_2{}^{\bullet} \rightarrow O_2 + O_2 + {}^{\bullet}OH$	-	1×10^{5}	0	1410	−121,92
24	$O_3 + H^{\bullet} \rightarrow HO_2{}^{\bullet} + O$	-	9×10^{6}	0.5	2010	−135,65
25	$O_3 + H^{\bullet} \rightarrow O_2 + {}^{\bullet}OH$	-	1.6×10^{7}	0	0	−96,2
26	$O + {}^{\bullet}OH \rightarrow H + O_2$	-	7.18×10^{5}	0.36	−342	-69,17
27	$H^{\bullet} + {}^{\bullet}OH \rightarrow O + H_2$	-	2.64×10^{-2}	2.65	2245	-8,23
28	$H^{\bullet} + H_2O \rightarrow {}^{\bullet}OH + H_2$	-	1.02×10^{3}	1.51	9370	64,35
29	$H_2O + O \rightarrow {}^{\bullet}OH + {}^{\bullet}OH$	-	2.21×10^{3}	1.4	8368	72,59
30	$^{\bullet} + M \rightarrow H_2 + M$	H_2: 2.5, H_2O: 16.0	2.45×10^{8}	−1.78	480	-444,47
31	$O_2 + M \rightarrow O + O + M$	H_2: 2.5, H_2O: 16.0	1.58×10^{11}	−0.5	59472	505,4
32	${}^{\bullet}OH + M \rightarrow O + H^{\bullet} + M$	H_2O: 5.0	4.66×10^{11}	−0.65	51200	436,23
33	$H_2O + M \rightarrow H^{\bullet} + {}^{\bullet}OH + M$	H_2: 2.5, H_2O: 16.0	1.96×10^{16}	−1.62	59700	508,82
34	$HO_2{}^{\bullet} + M \rightarrow H^{\bullet} + O_2 + M$	H_2: 2.5, H_2O: 16.0	2.46×10^{9}	0	24300	204,8
35	$O_2 + H_2 \rightarrow H^{\bullet} + HO_2{}^{\bullet}$	-	2.19×10^{7}	0.28	28390	239,67
36	${}^{\bullet}OH + {}^{\bullet}OH \rightarrow H^{\bullet} + HO_2{}^{\bullet}$	-	1.08×10^{5}	0.61	18230	162,26
37	$O_2 + {}^{\bullet}OH \rightarrow O + HO_2{}^{\bullet}$	-	3.1×10^{6}	0.26	26083	231,85
38	$O_2 + H_2O \rightarrow {}^{\bullet}OH + HO_2{}^{\bullet}$	-	2.18×10^{10}	−0.72	34813	304,44
39	$O_2 + H_2O_2 \rightarrow HO_2{}^{\bullet} + HO_2{}^{\bullet}$	-	4.53×10^{8}	−0.39	19700	175,35
40	${}^{\bullet}OH + {}^{\bullet}OH + M \rightarrow H_2O_2 + M$	H_2: 2.5, H_2O: 16.0	9.0×10^{-1}	0.90	−3050	-217,89
41	$H_2O + {}^{\bullet}OH \rightarrow H_2O_2 + H^{\bullet}$	-	1.14×10^{3}	1.36	38180	290,93
42	$H_2 + HO_2{}^{\bullet} \rightarrow H_2O_2 + H^{\bullet}$	-	1.41×10^{5}	0.66	12320	64,32
43	${}^{\bullet}OH + HO_2{}^{\bullet} \rightarrow H_2O_2 + O$	-	4.62×10^{-3}	2.75	9277	56,08
44	$H_2O + HO_2{}^{\bullet} \rightarrow H_2O_2 + {}^{\bullet}OH$	-	2.8×10^{7}	0	16500	128,67
45	$O_2 + O + M_1 \rightarrow O_3 + M_2$	M_1 O_2: 1.64; M_2 O_2: 1.63, H_2O: 15	4.1	0	−1057	-109,27

46	$N_2+O_2 \rightarrow N_2O + O$	-	6.3×10^7	0	55200	336.05
47	$O_2+N \rightarrow O + NO$	-	6.4×10^3	1	3150	133.37
48	$O+NO+ M_1 \rightarrow O + NO_2 + M_2$	M_1 NO: 20; M_2 O: 20, N_2: 20	1.1×10^3	0	-940	-311.14
49	$O+ N_2 \rightarrow N + NO$	-	7.6×10^{10}	0	38000	314.24
50	$HO^{\bullet}+ N \rightarrow H^{\bullet}+ NO$	-	4.5×10^7	0	0	202.53
51	$HO^{\bullet} + NO + M \rightarrow HNO_2 + M$	H_2: 2.3	8×10^3	0	-1000	-208.02
52	$HO^{\bullet} + NO_2 + M \rightarrow HNO_3 + M$	N_2: 2	5×10^5	0	0	-206.25
53	$HO^{\bullet} + N_2 \rightarrow N_2O + H^{\bullet}$	-	2.5×10^6	0	39000	267.32
54	$N_2O + O \rightarrow N_2+O_2$	-	1×10^8	0	14100	-336.05
55	$O + NO \rightarrow O_2+N$	-	1.5×10^3	1	19500	-133.37
56	$O + NO_2 + M_1 \rightarrow O+NO+ M_2$	M_1 NO: 20; M_2 O: 20, N_2: 20	1.1×10^{10}	0	33000	311.14
57	$N + NO \rightarrow O+ N_2$	-	1.6×10^7	0	0	-314.24
58	$H^{\bullet}+ NO \rightarrow HO^{\bullet} + N$	-	1.7×10^8	0	24500	-202.53
59	$HNO_2 + M \rightarrow HO^{\bullet} + NO + M$	H_2: 2.3	5.1×10^{11}	-1	25000	208.02
60	$HNO_3 + M \rightarrow HO^{\bullet} + NO_2 + M$	N_2: 2	1.6×10^9	0	15400	206.25
61	$N_2O + H^{\bullet} \rightarrow HO^{\bullet} + N_2$	-	7.6×10^7	0	7600	-267.32

The molar yield of hydrogen due to the sonochemical activity of a single acoustic cavitation bubble is given in Eq 1. 33 [29].

$$\frac{dn_{H_2}}{dt} = \frac{4}{3}\pi R^3 \sum_{i=1}^{N} (\vartheta'_{H_2 i} - \vartheta_{H_2 i})\, A_i e^{\left(\frac{-E_i}{RT}\right)} \prod_{k=1}^{K} (c_k)^{\vartheta_{ki}} \tag{1.33}$$

Where $\vartheta'_{H_2 i}$ and $\vartheta_{H_2 i}$ represent the stoichiometric coefficients (if existent) of H_2 appearing in the right and left sides, respectively, of the ith elementary reaction mentioned in Table 1-5. c_{ki} is the molar concentration of the kth reactant involved in the ith elementary reaction and ϑ_{ki} is its corresponding stoichiometric coefficient.

The bubble population is characterized through the number density of bubbles, described in [53,54]. The yield of hydrogen produced sonochemically within the electrolyte is then expressed as indicated in Eq 1. 34 [46], considering a bubble size distribution as reported in Table 1-6.

$$n_{H_2} = V \sum_{i=1}^{4} F_i \times N_i \times n_{i_{H_2}} \tag{1.34}$$

Table 1-6 *Size distribution if bubble population based on the ambient radius* [55].

Ambient radius R_0 (µm)	**20**	**40**	**60**	**80**
Number fraction F_i	18%	42%	22%	18%

1.4 Results and discussion

1.4.1 The Hoffmann cell sono-electrolyzer

1.4.1.1 Kinetics and repeatability

The Hoffmann configuration has been used in order to optimize the performance of the alkaline water electrolysis and demonstrate experimentally the influence of the integration of sonication, on both hydrogen production kinetics and energy conversion efficiency.

The electrolysis kinetics was evaluated through a series of repetitive experiments for both electrolyte solutions KOH and NaOH, under optimal conditions of electrolyte concentration, solution temperature, and bath temperature for each electrolyte (4.46 and 3.56 mol/L, 27°C and 50°C solution temperature, 27.5°C and 55°C of bath temperature for KOH and NaOH, respectively). The first objective of the repetitive experiments is to verify the repeatability in terms of electrochemical kinetics and hence energy conversion efficiency. Fig 1.2(a) and (b) report the three trials performed using KOH and NaOH electrolytes, respectively, and the resulting average values of mass flow rate of hydrogen production and the energy conversion efficiency percentage during electrolysis. In the case of KOH electrolysis, the relative standard deviation is estimated at 4.5%, while it attains 5.8% with NaOH, for both measures of H_2 mass rate and energy conversion efficiency. The repeatability is then demonstrated.

With both electrolyte solutions, the kinetics of hydrogen production attains its maximum at the beginning of the experience and decreases with time. Even though the potassium hydroxide is known to be a stronger electrolyte than sodium hydroxide as it is electrically more conductive for a similar molar concentration [20,56,57], the mass flow rate of produced hydrogen was higher in NaOH electrolyte reaching a value of 1.31 µg/s after 5 min of operation, and decreasing to a minimum rate of 1.13 µg/s

around 40 min, while the hydrogen production rate in KOH solution ranged between 1.09 and 1 µg/s over 40 min duration.

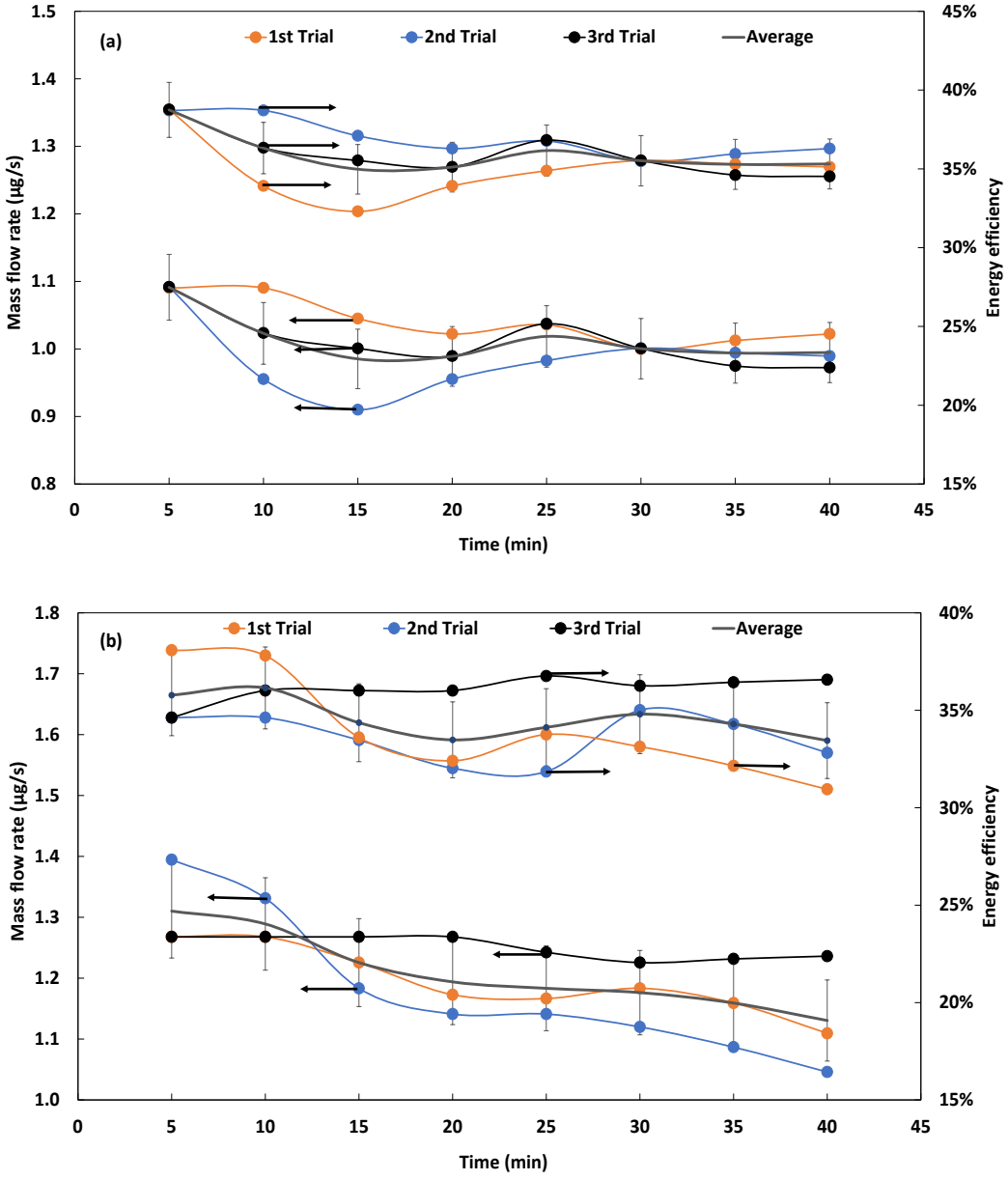

Figure 1.2 *Rate and energy conversion efficiency in KOH solution (a) and NaOH solution (b) using Hoffmann setup.*

Though unexpected, the higher rate observed in the case of NaOH electrolyte was also observed in the study of Zadeh et al.[20]. Zadeh et al.[20] attributed this observation to geometry of their electrolyzer, prevent the proper recovery of all the gases produced inside the cell and then causing defects in H_2 volume measurements. In the present experiments, the most plausible reason remains the physical properties of surface

tension, viscosity and density of both electrolyte at a given molar concentration, which results in distinguished adhesion behaviours of bubbles on the surface of the electrodes in both solutions, KOH and NaOH. The bubble resistance would then be higher when using KOH electrolyte, breaking the electrochemical kinetics. Hence, the previous observation is probably explained by the electrochemical resistances occurring in both electrolytes, specifically bubble resistance [28].

Energy conversion efficiency aims to reveal the proportion of electrical power converted actually to potential chemical energy stored in produced hydrogen. It was monitored while evaluating the kinetic of hydrogen production. Results are presented in Fig 1.2(a) and (b) for the two electrolyte solutions. Conversely to the mass flow, the energy efficiency was higher in the first 10 min using KOH solution attaining an average value of 39% within 5 min, and ranging between 39% and 35% during the whole operation time. Using NaOH electrolytic solution, the average energy conversion efficiency varied between 35% and 33%, showing a relative decrease due to the variation of the electrolyte around 9%.

1.4.1.2 Production of H_2 and energy conversion efficiency

We present here the results of the parametric study using the Hoffman setup in terms of H_2 production rate, in order to select the optimal operating conditions and explore the enhancement effect in the production of hydrogen due to sonication in the following paragraph. In Fig. 1.3, the effects of electrolyte concentration (a), solution temperature ambient temperature (b) and bath temperature (c) on the mass flow rate of produced hydrogen and the energy conversion efficiency during electrolysis are presented with both electrolytes KOH and NaOH.

Fig.1.3 clearly depicts that at low molar concentration of 2.67 mol/L, the electrolysis of sodium hydroxide solution leads to a slightly higher mass flow rate of hydrogen of 0.87 µg/s compared to the potassium hydroxide solution. At higher molar concentrations, sodium hydroxide becomes a considerably weaker electrolyte as compared to potassium hydroxide. The maximum mass flow of produced hydrogen is recorded in the case of KOH electrolyte under a concentration of 6.24 mol/L, it achieves 1.27 µg/s,

while it is attained at a concentration of 5.35 mol/L when using sodium hydroxide, with 0.99 µg/s. The smaller ions in potassium hydroxide increase the conductivity of the solution due to its lower viscous resistance [58], which explains the observed improvement in the rate of hydrogen with the increase of KOH concentration, relatively to NaOH. It is also noticeable that the mass flow rate of produced hydrogen is rather stable with the variation of the concentration of NaOH, with a largest variation of 13.8%. On the contrary, the variation of the concentration of KOH indices a significant enhancement of the produced rate of hydrogen, surrounding 74%. This observation reveals that the increase of the concentration of NaOH electrolyte is not justified in terms of the kinetic performance of the alkaline electrolysis.

Energetically speaking, the highest energy conversion efficiency of 38% was observed under an electrolyte concentration of 4.46 mol/L using KOH, which does not correspond to the optimum of hydrogen production. When this later is optimal, 37% of the feeding electrical energy is converted into potential chemical energy stored in hydrogen. Using NaOH, the energy conversion efficiency remains slightly constant around 34%.

In Fig 1.3(b) and (c), the effect of temperature is investigated using two different methodologies. In the first methodology, whose results are presented in Fig 1.3(b), the temperature of the bath is controlled over time in order to maintain the temperature of the electrolyzed solution constant at a certain value, which implicates the dissipation of the heat excess produced within the electrolyte volume due to electrolysis. This heat release is explained by the applied voltage that exceeds the thermoneutral voltage, and the exothermic nature of the electrochemical reactions occurring during electrolysis [59]. However, in order the initiate the electrolysis process, energy is required to fit the standard Gibbs free energy of formation of water, and overcome the change in entropy of the electrolysis reaction. In low-temperature water electrolysis, heat can be provided by supplementary heat sources or by Joule heating of the electric and ionic currents that flow through the cell resistances [60]. Therefore, in order to improve the energy efficiency, it is recommended to thermodynamically reduce the energy required to

separate water to produce hydrogen, for instance by increasing the operating temperature or pressure [28]. In the second methodology, whose results are reported in Fig 1.3(c), the temperature of the bath is maintained constant, which induces a permanent increase of the electrolyte's temperature owing to the accumulation of the released heat during electrolysis, as explained previously.

According to the results presented in Fig 1.3(b), the effect of the solution temperature on the mass rate of produced hydrogen follows a non-monotonous trend. Using KOH solution, it increases until reaching a maximum value of 1.29 µg/s at 45°C, while the maximum is reached at 50°C using NaOH, with a value of 1.27 µg/s.

The effect of the temperature on the energy conversion efficiency was non-monotonous and dependent of the type of the electrolyte. Fig 1.3(b) demonstrates that in potassium hydroxide solution, higher values are recorded within a range decreasing from 39% to 34% when the solution temperature is regulated increasingly between 40 and 60°C. Using NaOH, the energy efficiency varies between 33% and 35%, which is the maximum achieved with a solution temperature maintained at 50°C. Overall, the electrolyte temperature does not considerably affect the energy conversion efficiency during electrolysis using NaOH electrolyte.

On the other hand, Fig 1.3(c) shows the effect of bath temperature on the performance of the electrolysis. Using potassium hydroxide electrolyte, the mass rate of produced hydrogen increases with the increase of the bath temperature, reaching a maximum value of 1.34 µg/s at 60°C, whilst the maximum rate of H_2 is achieved using sodium hydroxide at 55°C with a value of 1.2 µg/s.

Besides, Fig 1.3(c) demonstrates that regulating the temperature of the bath instead of that of the solution leads to a quasi-constant value of energy conversion efficiency using KOH solution, stable around 37% to 38%. Whilst using NaOH electrolyte, the energy efficiency presents a non-monotonous trend, with a maximum of 34% attained at 55°C, which corresponds to the performance of the electrolysis under ambient temperature using the same electrolyte. Moreover, as the control of the bath

temperature prevents the evacuation of the released heat during the electrochemical reactions, the temperature of the solution increases due to the accumulation of heat, which slightly increases the flow rate of hydrogen, due to the increase of the ionic conductivity of the electrolyte and the rates of electrochemical reactions at the electrode surfaces [61]. The improvement is more significant with KOH solution, which can be attributed to the pronounced effect of the temperature on the conductivity of KOH solution, as demonstrated by Gilliam et al. [62] and reported by Allebrod et al. [57].

Summing up, with both electrolytes, varying the temperature of the solution demonstrated quasi-similar energetic performance as when operating at ambient temperature. It is assumed that the increase in temperature improves the electrochemical reactions and decreases the cell voltage [63]. Thus, for a given operating voltage, when increasing the temperature, the corresponding current density becomes greater. Although the increase of the current is supposed to improve the kinetics of hydrogen production, it also results in an increased power consumption of the electrolyzer, the compromise resulting of both variations explains the observed non monotonous variation of the energy efficiency, which we can fairly qualify of slightly fluctuating and relatively stable [64].

According to the obtained results, optimal conditions are different according to either energy efficiency or rate of produced hydrogen are optimized. It can be noticed that a greater energy efficiency was recorded for both electrolytes at low electrolyte concentration, and low temperature of electrolyte solution and bath. Thus, the optimization of the energy conversion aspect requires the use of relatively low operating parameters (3.56 to 4.46 mol/L of electrolyte concentration and ambient temperature). However, in terms of mass flow rate of hydrogen, the optimum was observed under high salt concentration as well as high temperatures of solution and bath. It is worthy to note, that increasing the operating temperature would have no action of the energy efficiency improvement, but may improve the kinetics of hydrogen production, by improving the kinetic parameters, accelerating the transport

phenomena and reducing the overpotentials [28]. The effect of the temperature seems to be more pronounced when using KOH solution, inducing a more important augmentation of H_2 rate in function of the increasing temperature, but also a higher rate of hydrogen at high temperature, as compared to NaOH.

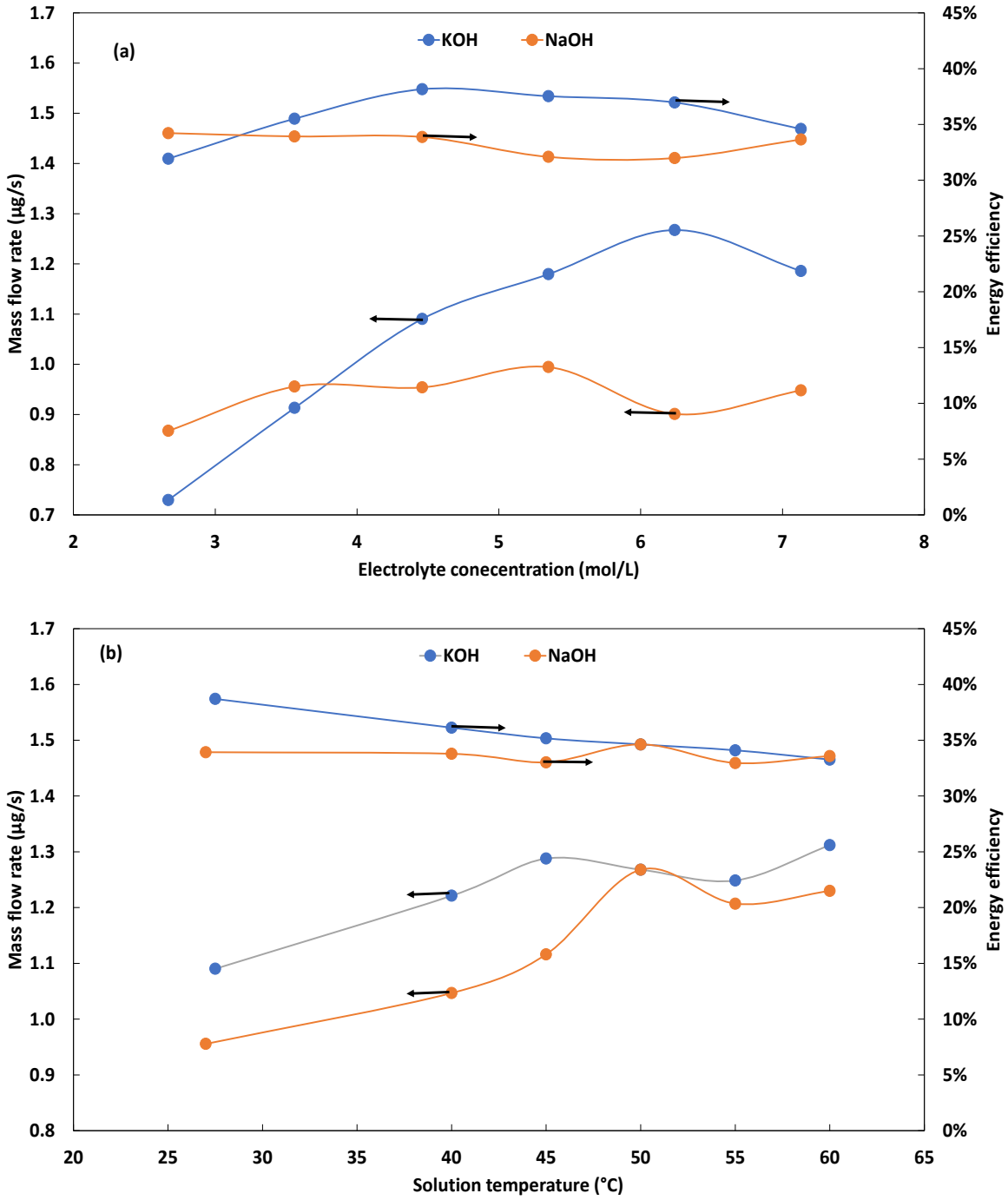

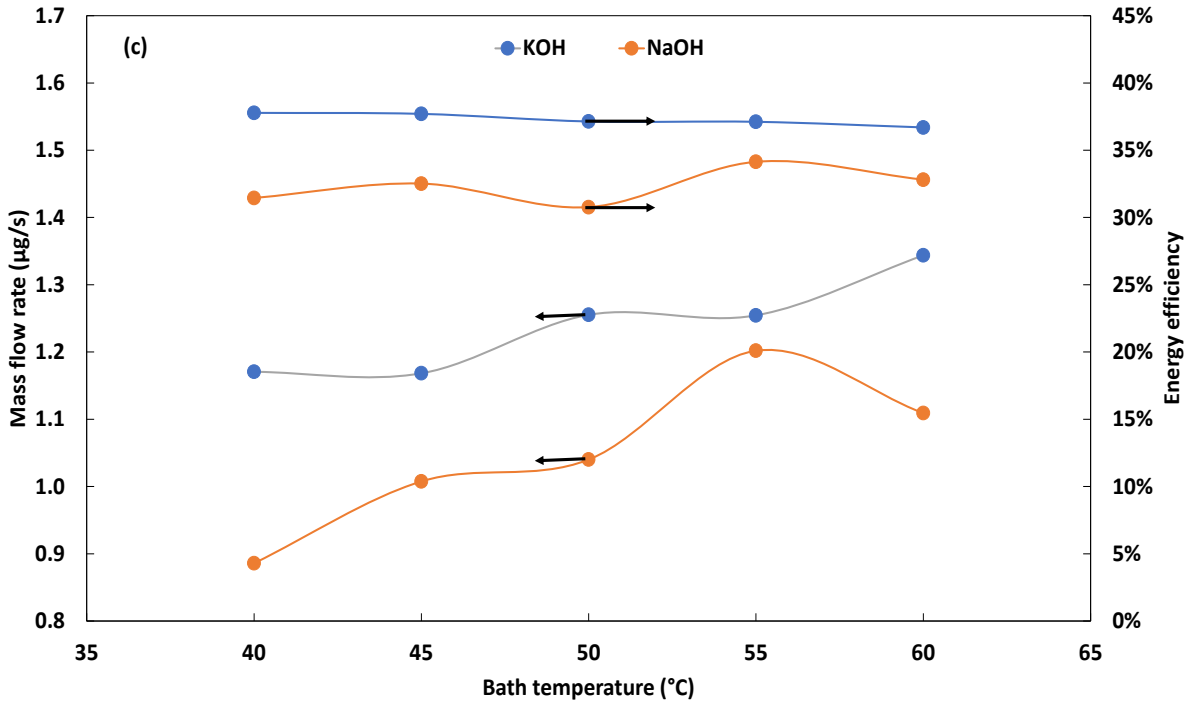

Figure 1.3 *Parametric study of water electrolysis for hydrogen production based on the concentration of KOH/NaOH electrolyte solutions (a), the solution temperature (b) and the bath temperature (c) using Hoffmann setup*

1.4.1.3 Preliminary sono-electrolysis results

The mass flow rate of hydrogen produced using the sono-electrolytic process is reported on Fig 1.4(a) and (b) for both KOH and NaOH solutions, respectively, at ambient conditions and optimal concentrations of the electrolytes.

The experimental results confirm the improvement of the mass flow rate of hydrogen due to sonication, in comparison with water electrolysis under silent conditions. Indeed, the mass flow rate of produced hydrogen through water sono-electrolysis was enhanced by 9.92% to 18.57% in KOH electrolyte and 14.28% to 26.6% in NaOH electrolyte. For instance, the average H_2 rate passed from 1.164 µg/s to 1.4 µg/s in KOH electrolyte, as illustrated in Fig 1.4(a), with an average standard deviation of 3.28%.

In Fig 1.4(c) and (d), the effect of ultrasound on the energy conversion efficiency of the electrolyzer is illustrated graphically, and a similar trend as in Fig 1.4(a) is observed. The integration of ultrasound field increases the energy efficiency by 5% to 11.9% in KOH solution and 2.7% to 15% in NaOH solution.

Overall, the effect of indirect continuous sonication was more pronounced using NaOH solution, which would be explained by the particularity of the acoustic cavitation phenomenon occurring in NaOH solution, as compared to KOH. For similar molar concentration, KOH solution is characterized by a higher surface tension [65], a higher viscosity [66] and a higher density [67]. According to Nazari-Mahroo et al. [68], the liquid bulk viscosity slightly affects the bubble dynamics in collapse phase. The effect of viscosity becomes significant only at high ultrasonic amplitudes and high viscosities, which is not the case in the present study. Interestingly, Wu et al. [69] found that low surface tension reduces the stability of the bubbles in the liquid medium. Meanwhile, the bubbles collapse earlier and farther from the rigid wall in the liquids with lower surface tension. The surface tension would be the major physical property impacting the degassing process in the studied alkaline solutions, KOH and NaOH. Its value, being lower with NaOH, the formed bubbles of hydrogen and oxygen are less stable and then more easily degassed at the surface of the liquid to the gas storage tanks. This interpretation is also valid in the absence of ultrasound, though the process would be slower than with ultrasound, the values of the surface tension explain the higher H_2 rate under silent conditions observed previously in section 1.4.1.2. Besides, in the presence of ultrasound, the acoustic streaming created parallelly to the electrodes' surface accelerates the ascension movement of the bubbles to the surface of the electrolyte, and consequently their degassing [70]. Micro streaming and shockwaves contribute as well in the enhancement of transport phenomenon within and between the anodic and cathodic compartments, which facilitates the ionic transport [71] and reduces the ohmic resistance [18,24].

In the next section, the same approach is followed with the H-cell configuration, where the cathode and the anode are disposed in two separated chambers, increasing the purity of produced gases in each compartment. The H-cell setup was adopted in our experiments due to its simple geometry, and the possibility to set a membraneless or membrane configuration, making it upgradable and suitable membrane sono-electrolysis, intended as a perspective of the study.

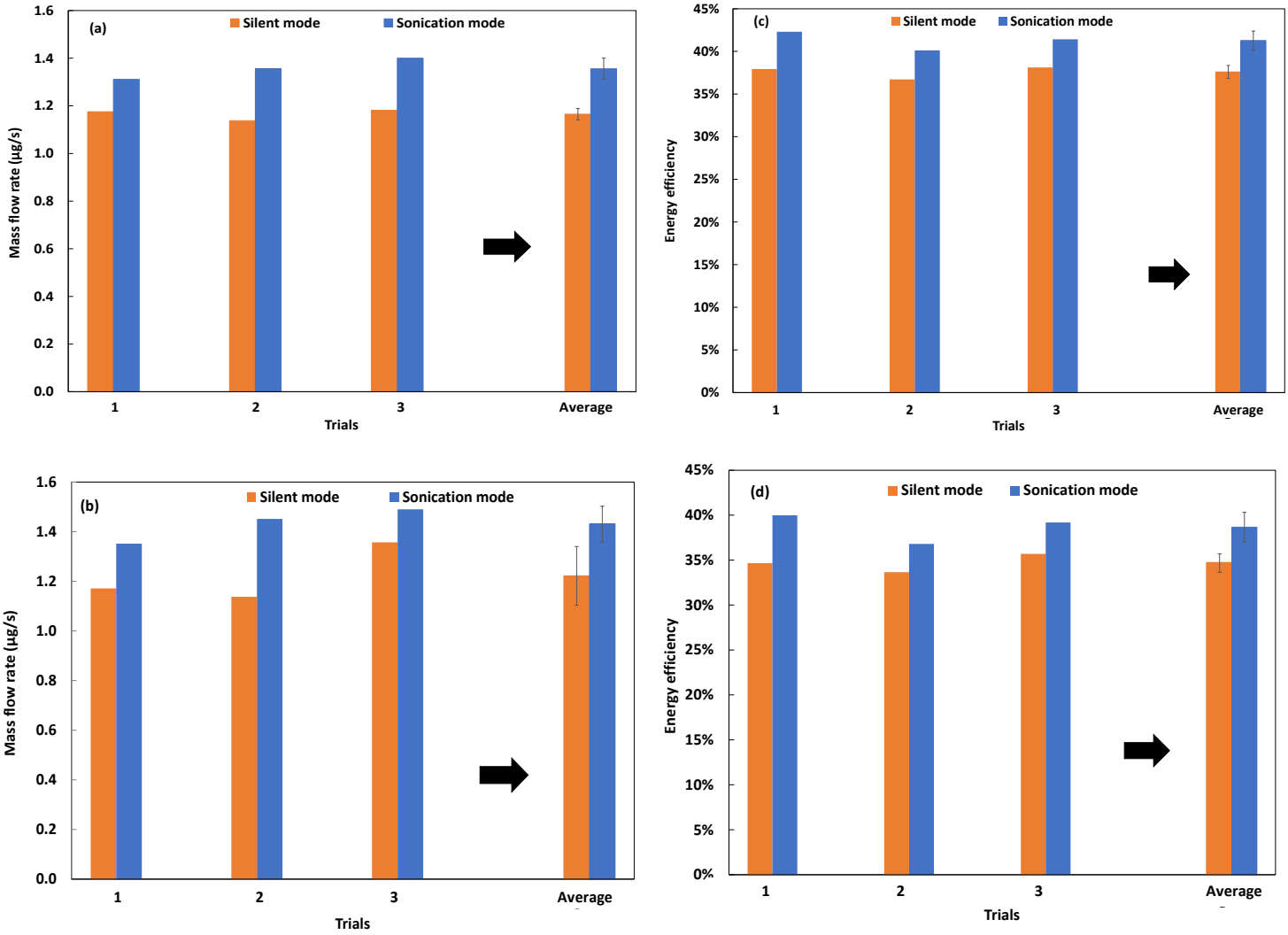

Figure 1.4 Comparison of water electrolysis and water sono-electrolysis processes for hydrogen production in function of mass flow rate in KOH (a) and NaOH (b) electrolytes and energy conversion efficiency in KOH (c) and NaOH (d) electrolytes, using Hoffmann setup.

1.4.2 The H-cell sono-electrolyzer

1.4.2.1 Kinetics of hydrogen production

In the present section, repeated experiments aiming to monitor the kinetics of the mass flow rate of produced hydrogen using the membraneless H-cell electrolyzer are presented in Fig 1.5 (a) and (b), with KOH and NaOH electrolytes, respectively, and nickel electrodes. This case is presented for illustration purposes, the repeatability was verified with all the other electrodes, namely stainless steel, nickel foam and graphite. The discussion first focuses on repeatability by mentioning the average standard deviation obtained in both aforementioned cases.

Fig 1.5 also demonstrates that the production of hydrogen is faster in KOH electrolyte as compared to NaOH. The duration of the experiments was set as the necessary time to fill a tank of 30 mL of hydrogen, this has been achieved within 9 min using KOH solution, and 12 min using NaOH. In both cases, the kinetics tend to attain a stable value versus time, however, using KOH electrolyte, the trend is initially increasing, while it is rather decreasing with NaOH.

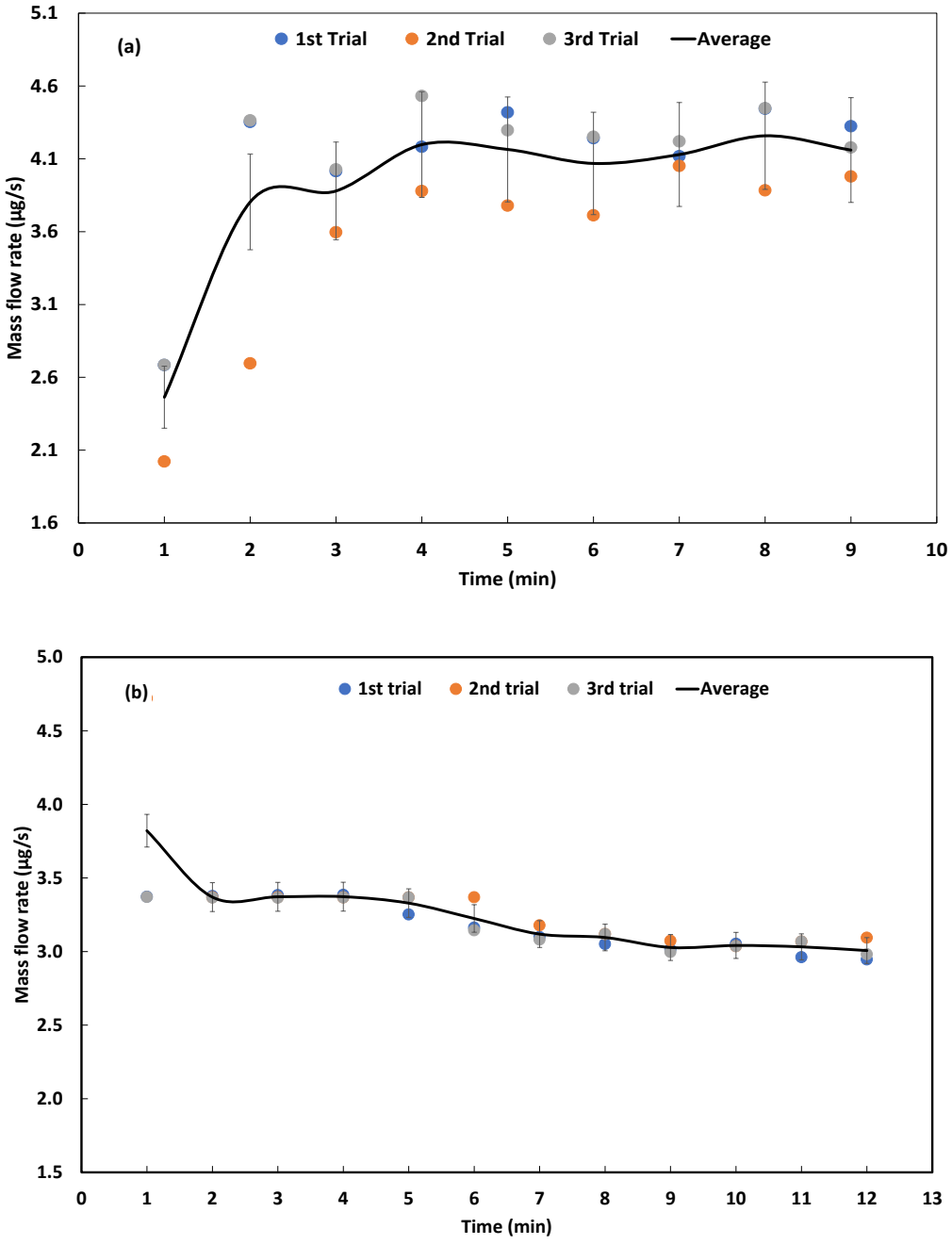

Figure 1.5 *Kinetic of hydrogen production using electrolysis of KOH solution (a) and NaOH solution (b), and nickel electrodes in a membraneless H-cell configuration*

The curves corresponding to the average mass rate of hydrogen production using KOH electrolyte reveal a maximum value of 4.1 µg/s attained after 4 minutes of operation, which remains quasi-stable. For the NaOH electrolyte, according to the curve of average rate of H_2, a maximum of 3.9 µg/s is reached after 1 minute of operation, and it decreases to a value of 3 µg/s by the end of 12 minutes.

Once the repeatability is verified, the configuration of the H-cell electrolysis will be optimized in silent conditions for the same parameters that have been monitored using the Hoffmann configuration, namely the electrolyte concentration, the solution temperature, and the bath temperature, in addition to the electrode's material, in order to integrate ultrasounds using the optimal configuration.

1.4.2.2 Optimization in silent conditions

a) Effect of electrolyte concentration

Figure 1.6 (a) shows the effect of KOH and NaOH concentrations in the electrolyte solutions on the mass flow rate of hydrogen produced and the energy efficiency of the process, with the aim of selecting the optimal electrolyte concentration, as the first parameter to be optimized, before integrating the ultrasonic power under optimal conditions.

The highest mass flow rate of hydrogen was obtained under higher concentration of KOH electrolyte of 7.13 mol/L using the four types of electrodes. The results of Fig 1.6 demonstrated that increasing the concentration of electrolyte does not show a monotonous effect on the mass flow rate. Using nickel foam and graphite, the amount attained 4.69 µg/s and 4.37 µg/s, respectively, while with stainless steel and nickel electrodes, H_2 rate attained 4.37 µg/s and 4.03 µg/s, respectively.

With NaOH electrolyte solution, 5.35 mol/L was the optimal concentration using nickel foam, nickel and stainless-steel electrodes, resulting in mass flow rates of hydrogen of 3.54 µg/s, 3.4 µg/s and 3.8 µg/s for each electrode material, respectively. Using graphite electrodes, the highest H_2 rate was recorded under a higher concentration of 6.24 mol/L. The average mass flow rate of produced hydrogen under this concentration is

estimated at 3.51 µg/s. At the opposite of what has been observed with the Hofmann cell configuration, KOH presents a better performance in terms of production H_2 rate in the case of the H-cell configuration. The explanation would come from the opposite and competitive effects of the ionic conductivity, in one hand, and the surface tension, in the other hand. The geometry of the H-cell facilitates the ions transport between both compartments; thus, the higher ionic conductivity of KOH solution becomes the controlling parameter of the electrochemical kinetics occurring in the cell, leading to an accelerated kinetics of hydrogen production, and consequently, a higher rate. The comparison of both examined cell geometries confirms the results of Zadeh et al.[20] who explained the observed differences in terms of hydrogen production using both KOH and NaOH electrolytes by the geometry of the cell. Based on the present results, the cell design offering a less complex pattern for ions displacement between the anodic and cathodic compartments would give the ionic conductivity of the electrolyte the upper hand in terms of the electrochemical kinetics, over the effect of the surface tension, which is the main parameter responsible for the degassing of the gaseous bubble at the surface of the electrolyte.

In terms of energy efficiency, the influence of the electrolyte concentration, using both KOH and NaOH salts, was non monotonous as well. NaOH electrolyte results in slightly higher values of energy conversion efficiency with the different concentrations, as compared to KOH. It is readily apparent that the optimal concentration of NaOH electrolyte is 5.35 mol/L using nickel foam, nickel and stainless-steel electrodes, corresponding to energy efficiencies of 47.77%, 50.20% and 52,96%, respectively. While in KOH solution, 4.45 mol/L was the optimal concentration of the electrolyte, at which energy efficiencies of 48.36%, 48.36%, and 48.71% were achieved using nickel foam, nickel and stainless-steel materials, respectively. Higher electrolyte concentrations of 6.24 mol/L and 5.35 mol/L with NaOH and KOH, respectively, were required for an optimal energy conversion efficiency using graphite as an electrode material. In alkaline water electrolysis, the salt concentration in the solution is usually up to 40% to ensure maximum electrical conductivity in the electrolyte [59]. While 25% to 30% potassium

hydroxide is commonly used for commercial electrolyzers [28]. This is in good agreement with the optimal concentrations recorded in the present study, ranging from 25% to 35% of mass.

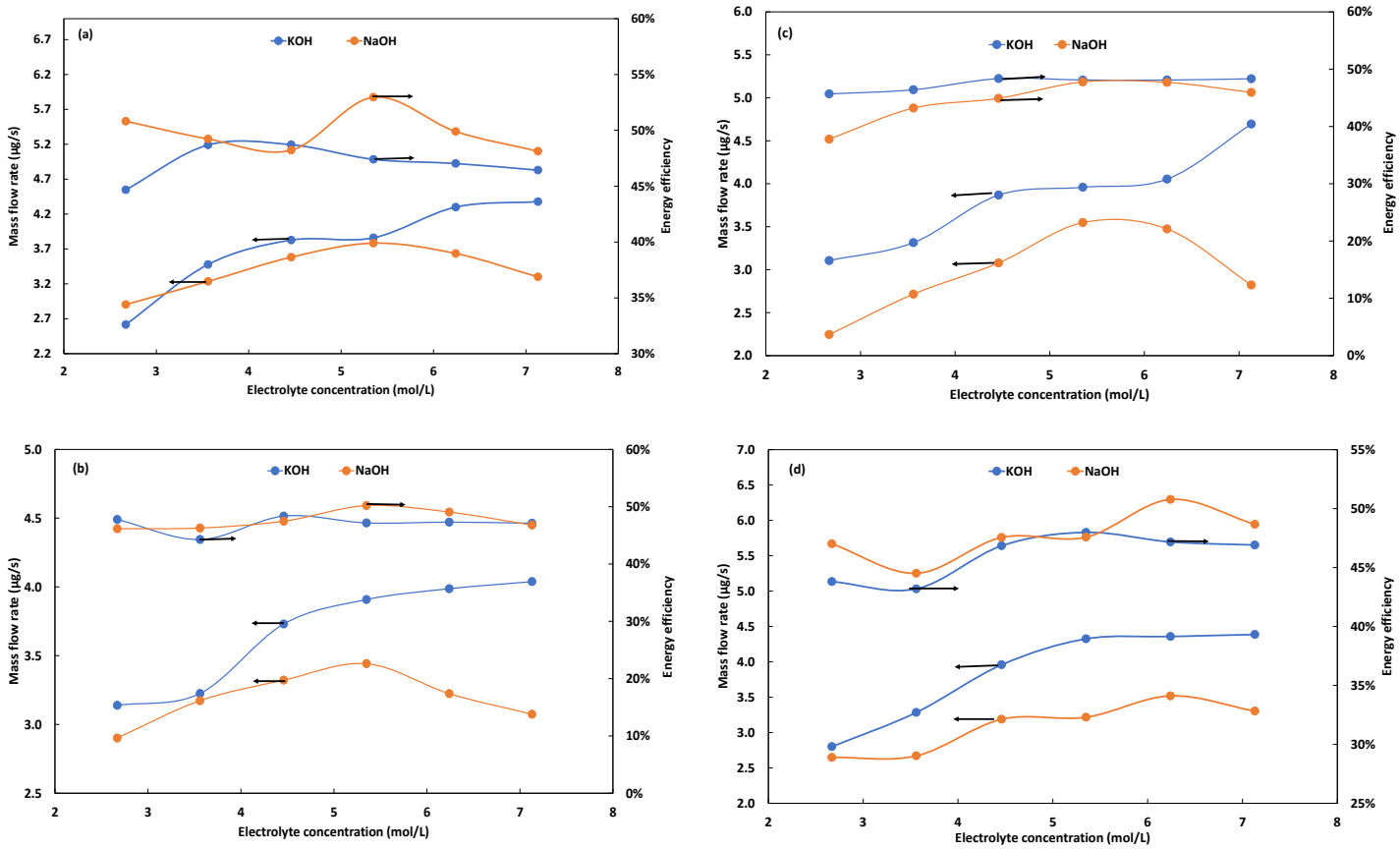

Figure 1.6 *Effect of KOH/NaOH concentrations on hydrogen production via water electrolysis in function of mass flow rate and energy conversion efficiency using stainless steel (a), nickel (b), nickel foam (c) and graphite (d) electrodes and using H-cell setup.*

It is assumed that increasing electrolyte concentration leads to a higher conductivity of the electrolyte solution which in turn improves the ionic transfer [28]. However, adding more conductive salt to the electrolyte would result in corrosion of the cell and damage the membrane in membrane electrolyzers. From a techno-economic point of view, it would also be associated with additional costs. Furthermore, during the electrolysis of water, the dispersion of bubbles in the electrolyte lowers the electrical conductivity in the electrolyte and increases bubble resistance and consequently ohmic resistance [27]. Using the H-cell configuration, KOH, being more conductive than NaOH, results in a faster electrochemical kinetics, induced at its turn by the higher current density feeding

the electrolysis cell. This double effect leads to a compromise between the power consumed by the electrolyzer and the potential chemical energy of the produced rate of hydrogen. Clearly, the acceleration in the electrochemical kinetics using KOH electrolyte does not compensate the increase in power consumption, resulting in a slightly higher energy conversion observed with NaOH.

b) Effect of the electrolyte temperature

The determination of the optimum temperature is a crucial step to investigate the hydrogen production improvement effect due to sonication. The effect of electrolyte temperature (ambient temperature, 40°C, 45°C, 50°C, 55°C and 60°C) on the mass flow of produced hydrogen and energy efficiency of the electrolyzer is depicted in Fig 1.7 (a), (b), (c) and (d) using the four electrodes' materials.

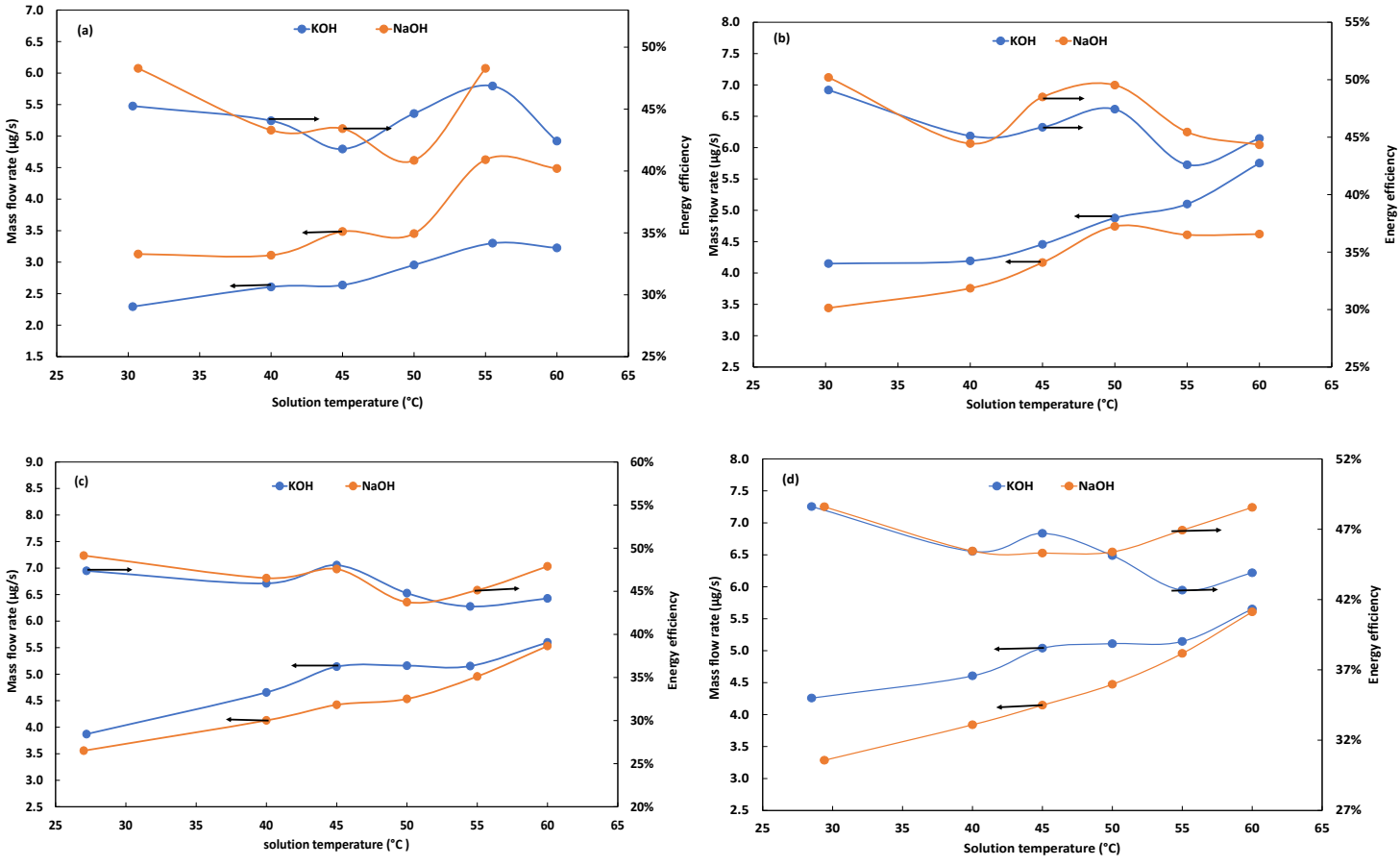

Figure 1.7 *Effect solution temperature on hydrogen production via water electrolysis in function of mass flow rate and energy conversion efficiency using stainless steel (a), nickel (b), nickel foam (c) and graphite (d) electrodes and using H-cell setup.*

The figures demonstrate that the solution temperature has a significant effect on the mass flow rate of H_2. Overall, raising the solution temperature increases the mass flow rate of hydrogen. The highest rate of hydrogen was recorded at 60°C with both KOH and NaOH electrolytes as predicted, since the increase of temperature enhances the electrochemical activity of water electrolysis process by increasing the overall kinetic of hydrogen production [59]. However, the rate of H_2 was optimal at 50°C in NaOH solution using nickel material, and at 55°C using stainless steel in KOH and NaOH solutions.

Fig 1.7 reports also the effect of the solution temperature on the energy efficiency of the process. In this case the increasing of operating temperature does not show a constant variation in energy efficiency. The highest energy conversion efficiency was recorded under the ambient temperature with all the electrodes' materials using NaOH electrolyte. At the opposite, this behavior was observed only with graphite and nickel electrodes when using KOH electrolyte, while 45 and 55 °C were the optimal temperatures in terms of energy efficiency using nickel foam stainless steel electrodes, respectively.

c) Effect of the bath temperature

Fig 1.8 (a), (b), (c) and (d) present the variation of mass flow and energy efficiency in function of bath temperature (40°C, 45°C, 50°C, 55°C, 60°C) as a second scenario for the temperature effect study. Regarding the mass flow of produced hydrogen, increasing bath temperature increases mass flow rate of hydrogen as it was observed previously in section 1.4.2.2 (b). The highest rate of mass flow of produced hydrogen was recorded under a temperature of 60°C using nickel foam, graphite, nickel and stainless-steel electrodes both in KOH and NaOH solutions. However, even though the highest rate was recorded at 60°C using stainless steel in KOH electrolyte, the variation was non-monotonous.

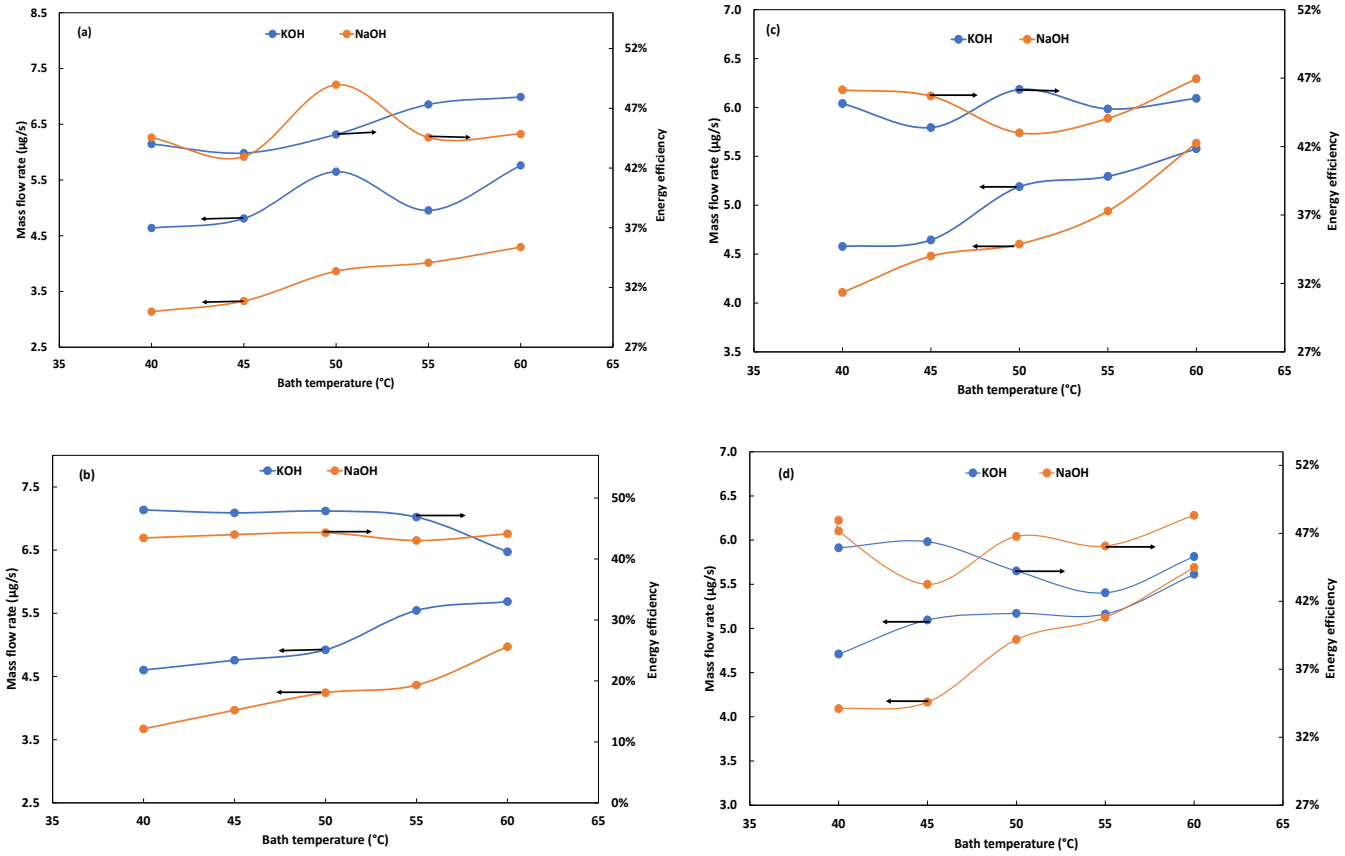

Figure 1.8 Effect bath temperature on hydrogen production via water electrolysis in function of mass flow rate and energy conversion efficiency using stainless steel (a), nickel (b), nickel foam (c) and graphite (d) electrodes and using H-cell setup

In terms of energy, the curves showing the energy efficiency for the four types of electrode materials in Fig 1.8 (a), (b), (c) and (d) show almost the same trend. The effect of bath temperature on the energy conversion efficiency of the process does not show a monotonous variation. For instance, in KOH electrolyte, 50°C and 45°C were the optimal temperature using nickel foam and graphite electrodes, while using nickel and stainless steel, the highest rates were attained at 40°C and 60°C respectively. Regarding NaOH electrolyte, the amount of produced hydrogen was greater under a temperature of 60°C using nickel foam, graphite and nickel electrodes, while using stainless steel, the highest efficiency was recorded at 50°C. analyzing the energy balance resulting from the excess of thermal energy consumption required for the temperature increase, and the gain in terms of energy efficiency demonstrates that the engaged heat increase is more important than the percentage of gained chemical potential energy stored in H2. In addition, it is admitted in the literature that from energetic perspective, an

efficiency of about 50% for low temperature alkaline water electrolysis is regarded as good [28]. Thus, the increase of the temperature of the solution through the control of the temperature of the bath appears to be energetically unjustified.

d) Effect of electrodes' material

In the present study, four types of electrodes' materials were selected based on the electrode structure (flat and porous), the availability and popularity of the materials for industrial electrolyzers (nickel and stainless steel), and finally the material feed stock cost (graphite). We analyze here the variation of hydrogen mass flow rate and energy conversion efficiency of water electrolysis according to the nature of electrode material, the results are reported in Fig 1.9 (a) and (b).

With regard to the electrode material, nickel foam was found to be the optimal material in terms of mass flow rate of produced hydrogen, followed by stainless steel, graphite and finally nickel. In KOH electrolyte, the highest mass flow rate recorded using nickel foam electrode was at 5.78 µg/s, while with stainless steel 304, it reached a value of 5.6 µg/s. Using graphite and nickel electrodes, the hydrogen mass flow rate increased over time reaching values of 4.8 and 4.6 µg/s, respectively. However, in terms of energy efficiency, the highest energy conversion efficiency was achieved using the nickel material with a value of 47.74%, followed by stainless steel 304, with 46.11%, then graphite and finally nickel foam. Nevertheless, the recorded values of energy conversion efficiency were very close with the four types of electrodes' materials.

With NaOH electrolyte, the same trend of the kinetics of H_2 production was observed. The nickel foam material leads to the highest rate reaching a value of 4.1 µg/s, followed by nickel, then stainless steel, then graphite. The kinetics of hydrogen production using graphite and stainless-steel electrodes were roughly similar, with mass flow rates ranging from 2.7 to 3.5 µg/s with graphite and from 2.7 to 3.4 µg/s with stainless steel. This observation was attributed to the fact that the porous structure of nickel foam allows the creation of more active sites for the electrochemical reactions under silent conditions [72].

In terms of energy conversion efficiency, the highest performance of the electrochemical cell was recorded using nickel electrodes, with a value of 54.79%, followed by nickel foam electrodes, with 50.97%. Finally, stainless steel and graphite showed the same performance with an energy efficiency of 49.94%. It is widely assumed that the nickel is a highly conductive material, resistant to corrosion in alkaline mediums [24], and widely used in industrial water electrolysis processes [3,73]. Furthermore, graphite electrodes made of carbon material demonstrate a great energy conversion performance and a low-cost available solution, which makes it a good alternative in water electrolysis systems for hydrogen production.

The electrodes have been described through the material constituting them with its proper microstructure. In the case of nickel plate, the structure consists of a crystalline plate while the nickel foam electrodes have a porous structure. The advantage of the porous structure of nickel foam is the creation of more surface for bubbles or electrochemical reactions to occur inside the pores of the electrode. These electrodes possess a very large effective (internal) surface area, compared to the apparent (external) surface area [74]. However, it was observed in silent conditions that bubbles tend to be stuck within the pores which prevents the upward movement of gas bubble from the electrode surface. After the integration of ultrasound power, the problem tends to be solved as the propagation of ultrasounds favours the detachment of bubbles from the pores and liberates the surface for new electrochemical reactions to occur. The rest of the electrodes used in this study have a plate structure namely stainless-steel 304, nickel and graphite. Nickel and stainless steel are known to have acceptable corrosion resistance as well as their considerably low price [75]. The propagation of the ultrasonic wave, as in the case of nickel foam electrodes, effectively removes the bubble from the electrode surface. Similarly, in the case of graphite plates, however, the aggressive action of ultrasound results in a noticeable deposition of graphite in the electrolyte solution.

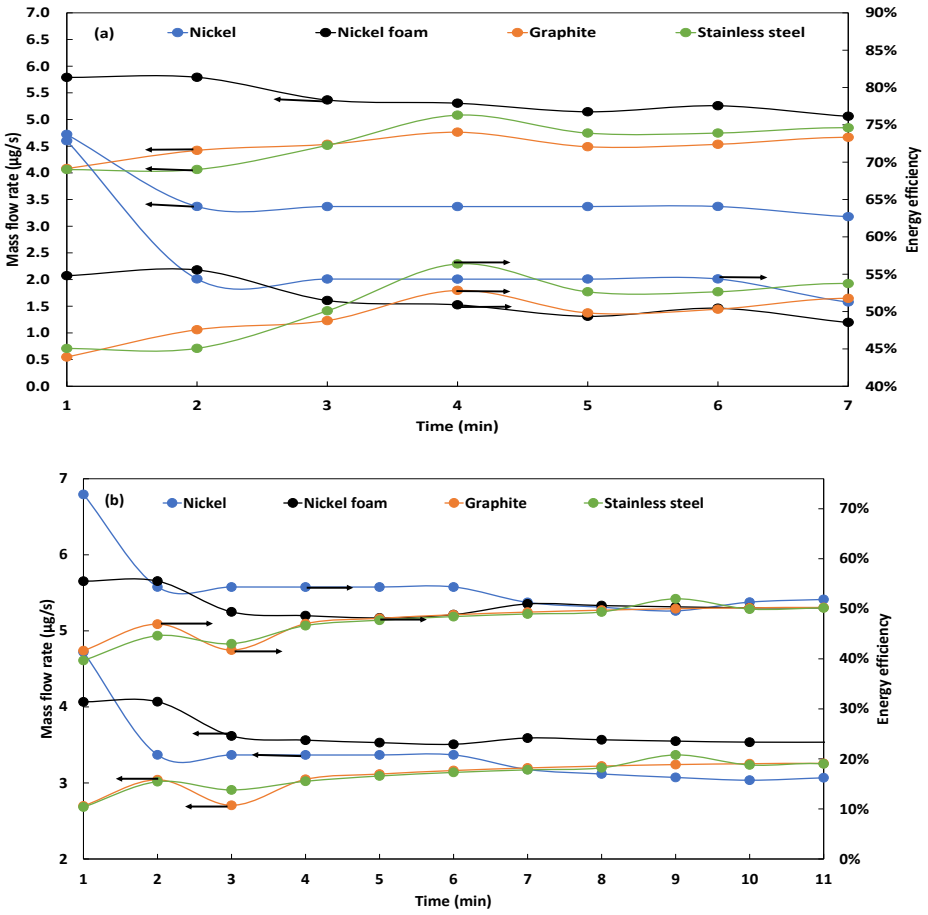

Figure 1.9 *Effect of electrode's material on hydrogen production via water electrolysis in function of mass flow rate in KOH (a) and NaOH (b) solution using H-cell setup*

e) Effect of electrolyte type

The previous experiments were carried out using the H-cell configuration and two types of electrolyte solutions KOH and NaOH. The parametric study applied to the electrolyte concentration, the solution temperature, and the bath temperature demonstrated that the highest rate of produced hydrogen was recorded within potassium hydroxide electrolyte, except in the case of high solution temperature using stainless-steel electrodes. For a given voltage, the current density produced using KOH electrolyte was higher than with NaOH. This is because potassium hydroxide is more electrically conductive and has a higher molecular mobility where electrons can flow more easily compared to sodium hydroxide, which allows current to be transferred more effectively [76], and enhances the mass transport, facilitated between the anodic and cathodic compartments by the geometry of the H-cell. However, it is worthy to mention that higher mass transfer does not mean higher hydrogen rate. Although

higher mass transport results in higher reaction rates, But the large number of gas bubbles formed due to the increased reaction rate can interfere with the contact between the electrodes and the electrolyte [28], leading to the apparition of a bubble resistance, increasing the ohmic resistance and dropping the current density. The observations established with the H-cell prove that the gain in the ionic conductivity when using the KOH solution compensates the associated increase of the ohmic resistance and leads to an accelerated kinetics of hydrogen production.

Regarding the energy conversion efficiency, both electrolytes demonstrated close values, with slightly higher efficiency recorded with NaOH, particularly at high electrolyte concentrations and high temperatures of the solution or the bath. Although it was verified that the use of KOH solution conducts to a higher current density, a compromise is created between the power consumed by the electrolyzer and the potential chemical power stored in the produced hydrogen. This balance results in a quite similar energetic performance of the electrolyzer with both electrolytes.

In summary, the parametric study of the preliminary observations has shown that higher concentrations of KOH give the highest hydrogen flow rates. Conversely, NaOH shows slightly better energy conversion efficiencies over a range of concentrations, while the optimal concentrations of both electrolytes, 25-35%, were in good agreement with industrial applications. In terms of electrolyte temperature, it was observed that higher temperatures generally lead to higher production rates due to increased electrochemical activity. Peak hydrogen production rates were observed at 60°C for both KOH and NaOH electrolytes. In terms of energy efficiency, the relationship with temperature is less straightforward. In particular, ambient temperature gave the highest energy efficiency with the NaOH electrolyte of all the electrode materials, and close results were observed with the KOH electrolyte. Similarly, the investigation of the effect of bath temperature on hydrogen production and energy efficiency reveals notable trends. Increasing the bath temperature generally increases the mass flow rate of produced hydrogen, with peak rates observed at 60°C across different electrode materials and electrolytes. However, the relationship between temperature and energy

efficiency is not monotonic. The analysis suggests that, from an energy point of view, increasing the temperature is not justified as the energy required to increase the temperature exceeds the gains in chemical potential energy stored in hydrogen. Finally, the study of the electrode material showed that nickel foam emerged as the optimal material for the kinetics of hydrogen production. This was attributed to its porous structure, which creates more active sites for electrochemical reactions. On the other hand, nickel showed the highest energy conversion efficiency. This is probably due to its conductivity and resistance to corrosion in alkaline solutions, making it widely used in industrial electrolysis processes.

In order to overcome the eventual bubble resistance limitation, sonication can be introduced to mechanically accelerate the removal of the bubbles. The combination of electrolysis and indirect sonication, namely sono-electrolysis, is studied using the H-cell configuration in the following section, with both continuous and pulsed modes.

1.4.2.3 Integration of sonication

This part of the study aims to highlight the effect of ultrasound power on the performance of water electrolysis process for hydrogen production by promoting the mass transfer and bubble removal from the electrodes surface. The H-cell was indirectly irradiated using continuous and pulsed modes. The results are presented in the next sections.

a) Continuous mode

Fig 1.10 presents the polarization curves under silent and sonicated conditions using continuous mode and four types of electrodes at ambient temperature and optimal concentrations corresponding to each electrodes' material and electrolyte, aiming to study the effect of ultrasonic irradiation on the evolution of the current in function of the electrolysis voltage.

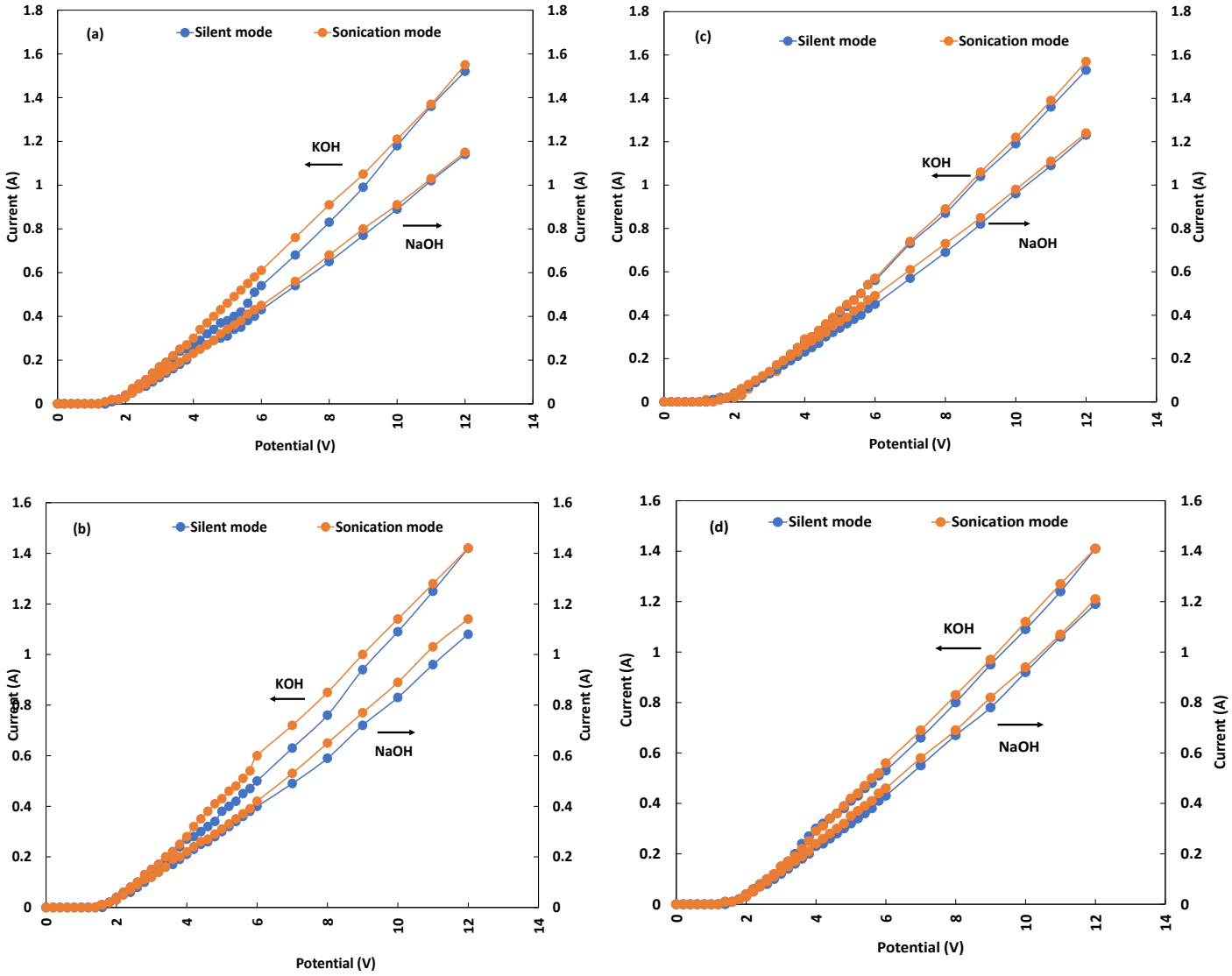

Figure 1.10 Comparison of I-V curves during water electrolysis and water sono-electrolysis for hydrogen production using stainless steel (a), nickel (b), nickel foam (c) and graphite (d) electrodes and using H-cell setup.

The comparison of both curves obtained under silent and ultrasound conditions demonstrates that sonication increases the value of the current travelling the electrolyzers for a given voltage. The improvement was more pronounced in KOH electrolyte using stainless steel, nickel foam and nickel electrodes, with improvement rates reaching 8.07%, 7.78% and 1.78%, respectively. This can be attributed to the efficient enhancement in mass transport due to propagation of ultrasonic power in the electrolyte solution, which in turn increases the electron transport and thus improves the cell current.

Fig 1.11 (a), (b), (c) and (d) present the average mass flow rate of produced hydrogen and energy efficiency under silent and continuous ultrasound using the four electrodes' materials in KOH and NaOH solutions. The reported results refer to the experiments performed under ambient temperature and optimal concentration related to each material and electrolyte, according to the findings of the previous parametric study. Other experiments of sonication integration at optimal solution temperatures have been carried out, their results will be discussed in the present section. The experiments were also repeated three times each, and the average efficiency as well as the relative standard deviation were calculated in order to verify the repeatability.

Based on mass flow rate of produced hydrogen, Fig 1.11 (a) and (b) show that the effect of ultrasound on the electrochemical kinetics of H_2 production is dependent of the type of the electrolyte as well as the electrode material. For instance, using KOH solution, the continuous sonication leads to a higher kinetic performance with nickel, nickel foam and graphite electrodes, with improvement rates in the order of 3.8%, 2.5% and 2.8%. Using NaOH solution, the continuous sonication leads to the enhancement of hydrogen production with all the electrode materials. The highest improvement is recorded with stainless steel electrodes, with a rate of 9.8%, followed by nickel, with a rate of 7.6%, then graphite electrodes and finally nickel foam, with respective rates of 4.4% and 2.4%. The observed dependency of the indirect continuous sonication on the type of the electrolyte can be attributed to the lower surface tension of NaOH, as compared to KOH, facilitating the formation of unstable bubbles and enhancing consequently the degassing, with all the tested electrodes. Besides, nickel foam revealed to lowest improvement due to sonication, which may be explained by the penetration of the formed bubbles, mainly by heterogeneous solid-liquid cavitation process, in the pores of the material, making more complex their desorption and degassing.

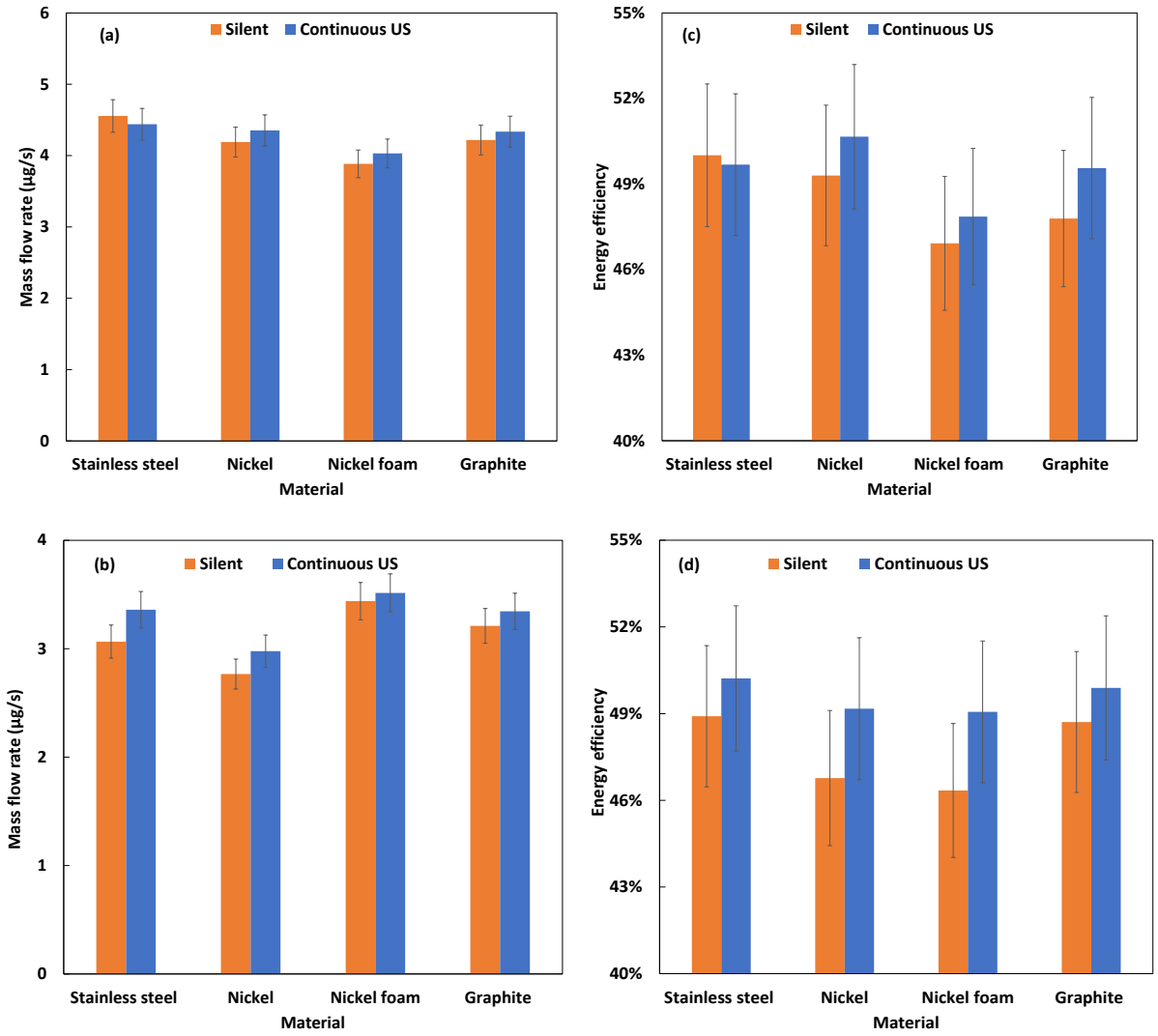

Figure 1.11 *Comparison of silent and continuous modes effects on the mass flow rate of H_2 energy efficiency for hydrogen production in function of electrodes material in KOH (a, c) and NaOH (b, d) using H-cell setup.*

In all experiments, the ultrasonic bath was placed below the cell, thus the propagation of the wave is longitudinal i.e. parallel to the electrodes' surfaces, which directs the formed cavitations upwards (rather than hitting the electrodes' surface). This is explained by the fact that ultrasonic actions promote the desorption of atomic species from the electrode's surface through the microjets and the shockwave as well as the degassing effect that reduces the accumulation of gas bubbles at the electrode's surface [16] (this is mainly supported by the acoustic amplitude, averaging 0.99 bar according to the experiments). This leads to a lower cell voltage and thus reduces the energy consumption [16].

The energy of US is released at the bubble collapse in the form of mechanical power through the aforementioned mechanisms, helping the gas bubbles to desorb from the electrode surface and move to the gas reservoir (positive energetic process), then all the released power in transformed to heat, which is evacuated across the anodic and cathodic compartments walls to the water bath (which is regulated in terms of temperature)

In terms of energy conversion efficiency, Fig 1.11 (c) and (d) demonstrate that with stainless steel sono-electrolysis system, the effect of ultrasound application is not noticeable in KOH electrolyte, while an increase in the energy efficiency from 48.91% to 50.20% is observed in NaOH. In the case of nickel, the effect of ultrasound power was more pronounced in sodium hydroxide solution, where the energy efficiency passed from 46.77% to 49.17%. Using graphite material, the recorded improvements in the energy efficiency in KOH and NaOH electrolytes were in the order of 3.7% and 2.4%. The largest difference is recorded with nickel foam electrodes, where the integration of sonication leads to an improvement of 2.00% using KOH electrolyte, whilst 5.87% is achieved in NaOH. Overall, NaOH demonstrated a more significant effect of sonication in terms of energy conversion during electrolysis.

The integration of sonication to electrolysis configuration with higher solution temperature was analyzed as well, a particular attention is paid to the nickel foam case, using KOH electrolyte. The optimization of the operating conditions using nickel foam electrodes with KOH electrolyte demonstrated in the previous section that 45°C is the optimal solution temperature for the improvement of the energy conversion efficiency of the electrolysis. The effect of incorporating sonication in this particular case was rather negative as the energy efficiency passed from 47.48% to 46.34%, while a considerable improvement in energy efficiency, in the range of 1.63% to 5.07%, was observed using sono-electrolysis at room temperature, as compared to silent conditions. It is also noticeable that the performance of the sono-electrolysis in the case of nickel foam electrodes and KOH electrolyte at ambient temperature results in an average energy efficiency of 47.86%, which is higher than the performance of the

electrolysis under silent conditions and high temperature operation. The negative effect of ultrasound at high operating temperature would be explained by the attenuation of the acoustic cavitation effects at single bubble scale [77]. Therefore, we may conclude that the integration of the ultrasonic field in the case of nickel foam electrodes and KOH electrolyte would compensate the enhancement due of the temperature increase under silent conditions, and lead to a gain in the energy supplied to the heating module.

Overall, the enhancement due the integration of sonication to the electrolysis system is mainly attributed to the role acoustic streaming and physical effects associated with acoustic cavitation on the detachment of the bubbles from the surface of the electrodes [3], which accelerates the degassing process and liberates active reactional sites on the electrode surface. This was clearly observed in our experiments, bubbles clouds created in the solution and around the surface of the electrodes under silent conditions were considerably decreased after the integration of ultrasound power. It is widely accepted that the propagation of ultrasound wave results in the increase of the transport phenomena in the electrolyte, particularly mass transfer. This effect of sonication lowers the ohmic resistance by decreasing the bubble resistance, and enhances the performance of the alkaline electrolyzer through the reduction of the overall cell voltage [25]. In the present study, the action of ultrasound was confirmed through the overall reduction of the initial current I_0 and the cell current I when using ultrasound, compared to silent condition at ambient temperature as presented in Table 1-7. The measurements of the initial and permanent values of the electrolysis and sono-electrolysis current allowed the evaluation of the bubble resistance.

The calculation of the cell resistance at the initial instant and under permanent operating conditions allows the determination of the resistance increase due to the apparition of the bubbles in the liquid and around the surface of the electrodes. The bubble resistance was estimated under silent and continuous sonication, and the drop in bubble resistance due to ultrasound was calculated for the different configurations of electrodes' material and electrolyte solutions reported in table 1-7. The highest

decrease was observed with Nickel foam electrodes using KOH electrolyte, where the bubble resistance passed from 1.29 to 0.46 Ω, presenting a reduction rate of 64%. An equal rate was retrieved with graphite electrodes using NaOH solution, then with Nickel using the same electrolyte, with a rate of 55%. The sonication did not show any improvement in terms of bubble resistance using Nickel electrodes with KOH solution, though the kinetics and energetic performances presented an observable improvement when integrating ultrasound to this configuration. The improvement would be explained in this case by the enhancement of the ions transport between the anodic and cathodic compartments, rather than the bubbles removal.

Table 1-7 *Initial and cell current variation with and without ultrasound power*

	Current (A)	**Electrolyte**	**Nickel foam**	**Nickel**	**Graphite**	**Stainless steel**
Silent mode	I_0	KOH	0.32	0.34	0.34	0.34
		NaOH	0.28	0.22	0.26	0.23
	I	KOH	0.29	0.31	0.31	0.325
		NaOH	0.242	0.21	0.232	0.22
Continuous ultrasound mode	I_0	KOH	0.3	0.33	0.33	0.34
		NaOH	0.27	0.22	0.25	0.25
	I	KOH	0.29	0.30	0.308	0.33
		NaOH	0.243	0.215	0.24	0.24

Finally, it is worthy to note that the integration of indirect sonication is associated with the intrinsic energy conversion efficiency from the electrical form to the acoustic form, measurable using the calorimetric method, applied to the electrolyte solution in the absence of any electrical field. The monitoring of the temperature of the solution over time allowed the estimation of the dissipated power due to the acoustic cavitation event and its related physical (and eventually chemical) effects, deeming that all the energy implicated in the acoustic cavitation phenomenon is recovered after the collapse of bubbles in the form of heat dissipated in the liquid [29,78]. The calorimetric

measurements established according to Eq 1.23 demonstrate that the acoustic energy conversion efficiency is comprised between 7.97% and 13.7%. The improvement of the energy conversion efficiency of the sonication process remains one of the main challenges of the overall sonoelectrolysis process, although some studies revealed that the scaling up of the combined process compensates the energy consumption related to sonication. For instance, Lin and Hourng [24] demonstrated that at normal temperature, the difference in current density between sonoelectrolysis and silent electrolysis is estimated at 240 mA/cm^2 (4 V of electrolysis potential, 40 wt% of electrolyte concentration, 225 W of sonication power and 2 mm of electrodes gap). Deducting the power needed for sonication, a power saving of 3.5 kW and an economical power efficiency of 15% were recorded.

b) Pulse mode

The pulsed sonication mode was combined to the electrolysis, and kinetics and energetic performances were analyzed and compared to the sono-electrolysis. Fig 1.12 (a), (b), (c) and (d) report the mass flow rate of produced hydrogen and the energy conversion efficiency obtained with the different electrodes' materials and both KOH and NaOH electrolytes, under the optimal conditions of concentration and ambient temperature.

Clearly, the electrochemical kinetics of hydrogen production is better enhanced using continuous mode, as compared to pulsed ultrasound mode in sono-electrolysis. The average values of both parameters were calculated after three repetitive trials to verify the repeatability of the results. For instance, in the case of nickel electrodes, relative standard deviations of 0.91% and 2.26% were obtained in KOH and NaOH, respectively, which guaranties the repeatability. Overall, the energy efficiency was negatively impacted when replacing continuous sonication by pulsed one, though pulsed sonication was still effective compared to silent conditions. To illustrate, in the case of graphite electrodes, energy efficiency was promoted with 4.22% in KOH and 0.38% in NaOH solution when using pulsed sonication, as compared to pure electrolysis. The intrinsic acoustic energy conversion efficiency related to the pulsed mode is slightly

identical to that of the continuous sonication. In this context, Al-Juboori et al. [79] demonstrated that the measured efficiency of the pulsed ultrasonic system in converting electrical energy into calorimetric energy was found to be constant for all the ratios of on/off periods of pulsed mode, and equivalent to that for continuous operation. Thus, continuous sonication is proved to be the optimal mode to adopt in the sono-electrolysis system, both kinetically and energetically speaking.

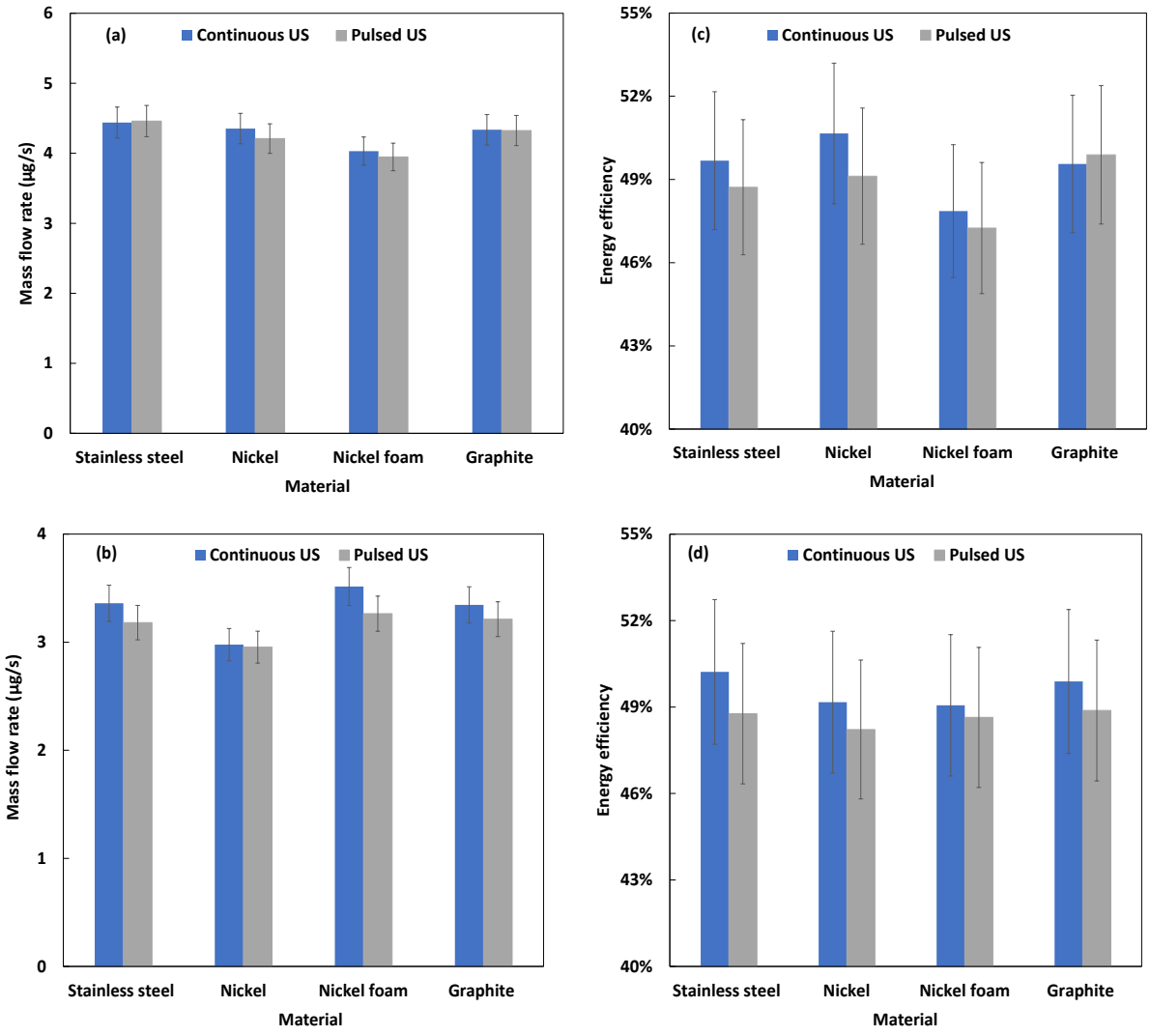

Figure 1.12 *Comparison of pulsed and continuous modes effects on the energy efficiency for hydrogen production in function of electrode material in KOH (a) and (c) and NaOH (b) and (d) using H-cell setup*

1.4.3 Modelling reading of the kinetic and energetic performance

1.4.3.1 Calorimetric characterization

In order to link the modelling and simulation to the experiments, the actual acoustic power received by the electrolyte is determined using calorimetric measurements, the acoustic pressure is then calculated and used as a simulation condition. Fig 1.13 presents the variation of the temperature of the electrolyte due to sonication, as well as the corresponding evolution of the acoustic power in function of time over 10 min of continuous sonication. The evolution of the temperature is quasi-linear, resulting in an average acoustic power of 8.13 W received by the 300 mL of electrolyte solution. Considering the receiving area of the electrolyzer, corresponding to the bases of both anodic and cathodic compartments, perpendicular to the travelling wave, the calculated acoustic power corresponds to an acoustic intensity of 3263.6 W/m^2, and an acoustic amplitude of 98.95 kPa.

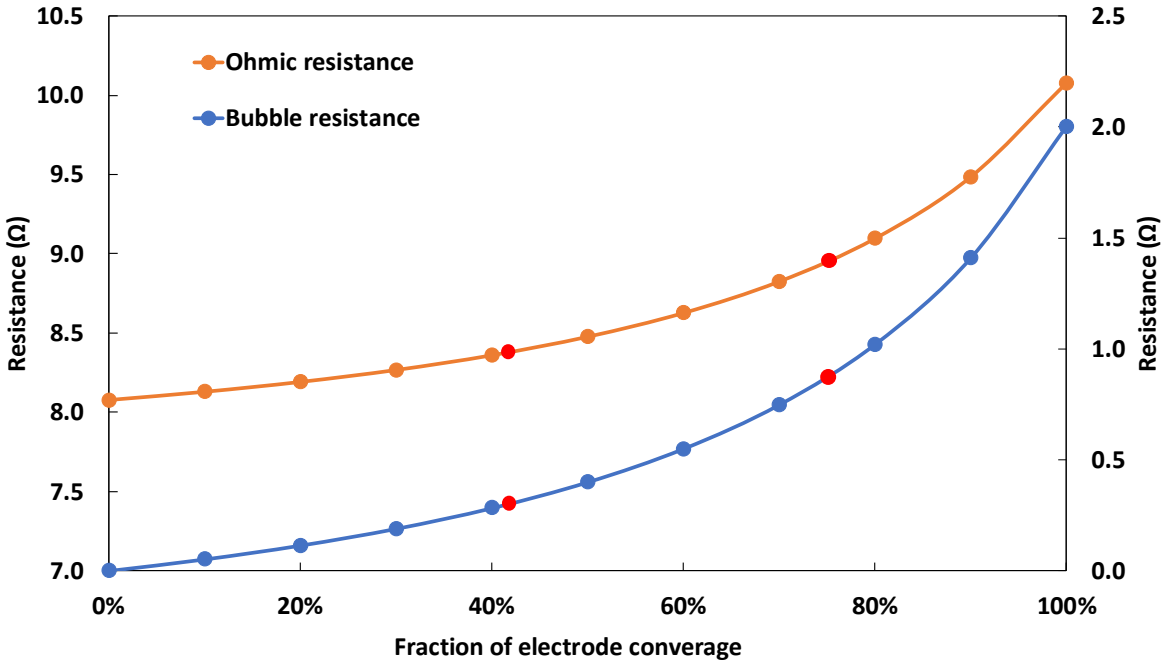

Figure 1.13 *Evolution of the electrolyte temperature and acoustic power due to indirect sonication as a function of time (40 kHz, 60 We, 300 mL).*

Considering the electrical power feeding the sonicator, i.e., 60 W, the effective energy conversion efficiency is equivalent to 13.7%. As the studied setup of sono-electrolysis relies on indirect sonication, the 86.3% of the electrical power supplying the sonicator

are dissipated in the form of heat at the transducer itself, the bath vessel, and the sonicated water in which the electrolyzer is immersed.

The acoustic amplitude of 99.95 kPa is adopted in the simulation of acoustic cavitation and its associated effects, presented in section 1.4.3.4.

1.4.3.2 Kinetics of hydrogen production and energy conversion efficiency

The volumes of produced hydrogen and oxygen have been monitored over time during the electrolysis operation under an applied voltage of 4 V. The mass flow rates have been then assessed, we focus here on the mass flow rate of hydrogen, under silent and ultrasound conditions, Fig 1.14 (a) reports the obtained values. The figure shows an average improvement in H_2 rate of 3.93%. On the other hand, Fig 1.14 (b), which reports the energy conversion efficiency in both cases, demonstrate a relative gain of 2.76%.

The improvement of hydrogen flow rate is attributed to the increase in the cell current, due to the drop in the ohmic resistance. The decrease of the ohmic resistance can be explained by the surface cleaning of the electrodes in the presence of ultrasounds, accelerating the removal of bubbles and freeing the electrochemical reactional sites on the electrodes' surfaces. This increases the electron transport and thus improves the cell current and the kinetics of hydrogen production. The energy conversion efficiency results of the competitive phenomena accompanying the increase of hydrogen flow, namely the increase of the consumed power (due to the increase of the cell current for a constant potential), and the augmentation of the potential chemical energy stored in the flow of produced hydrogen. As the effect of sonication is positive, the observed increase is attributed to the predominance of the increase of the flow of recovered hydrogen, as compared to consumed power.

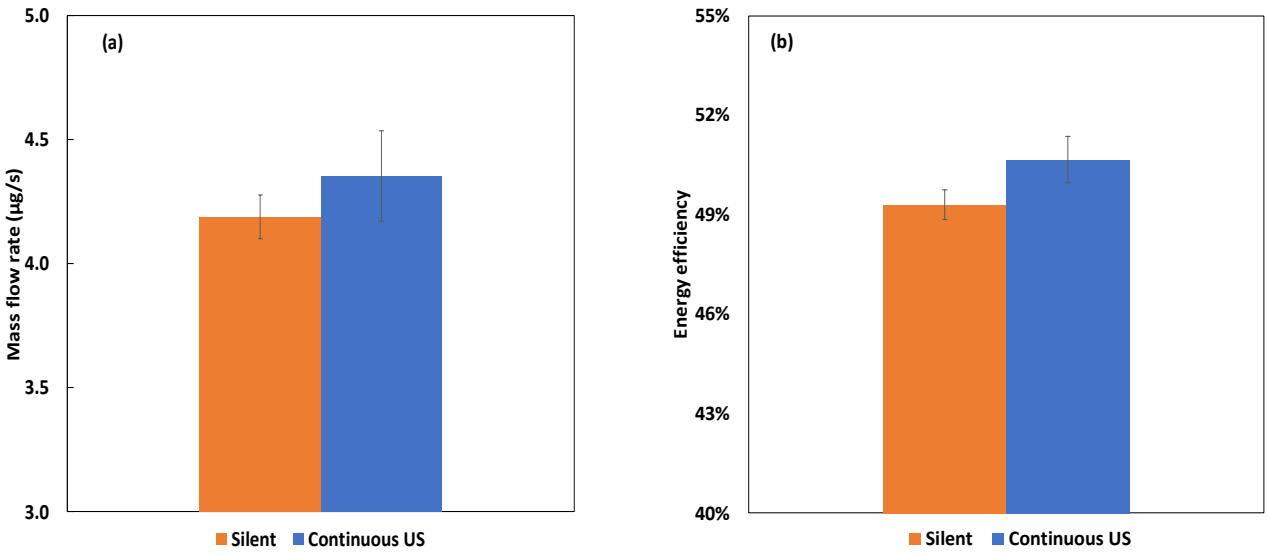

Figure 1.14 *Mass flow rate of hydrogen (a) and energy conversion efficiency (b) under silent and ultrasound conditions.*

1.4.3.3 Cell resistance

Polarization curves are plotted under silent and ultrasound conditions by varying the applied voltage from 0 to 12 V, and recording the corresponding current density. The results are reported in Fig 1.15 (a), to highlight the noticed variation in the absence and presence of indirect continuous sonication.

The decomposition voltage method has been adopted to estimate the cell resistance in both cases. The decomposition voltage is defined as the minimum potential difference that must be applied between a pair of electrodes before decomposition occurs and a current flows [80]. The extrapolation of the second portion of the curve back to zero current reveals a decomposition voltage value of 1.6 V under silent and ultrasound conditions. Considering a reversible potential of 1.23 V, according to Eq 1.6, the activation overpotential is then experimentally estimated at 0.37 V. Sonication has no effect on the activation overpotential.

Besides, the obtained curves demonstrate quasi-linear evolutions, and no third portion is distinguishable within the covered range. Hence, the second portion concerns the ohmic overpotential, the ohmic resistance is then deduced from the slop of the curves.

The average ohmic resistance is estimated at 9.03 Ω under silent conditions, and 8.38 Ω under ultrasounds, which is equivalent to a drop of 7.2%.

Fig 1.15 (b) reports the variation of the resistance of the cell as a function of the cell potential. It is noticed that at low cell potential within the range from 2 to 2.6 V, ultrasounds have no effect and similar values are recorded under silent and ultrasounds conditions. However, a difference is observed starting from 2.8 V, with lower resistance under continuous sonication. The highest gap is attained at 4.8V, with a relative decrease of 17.11% under ultrasound treatment. Overall, the induced difference in terms of the cell resistance in the presence of ultrasounds is observable over the interval 3 to 12 V, which corresponds to the portion of the ohmic overpotential as shown in Fig 1.15 (a).

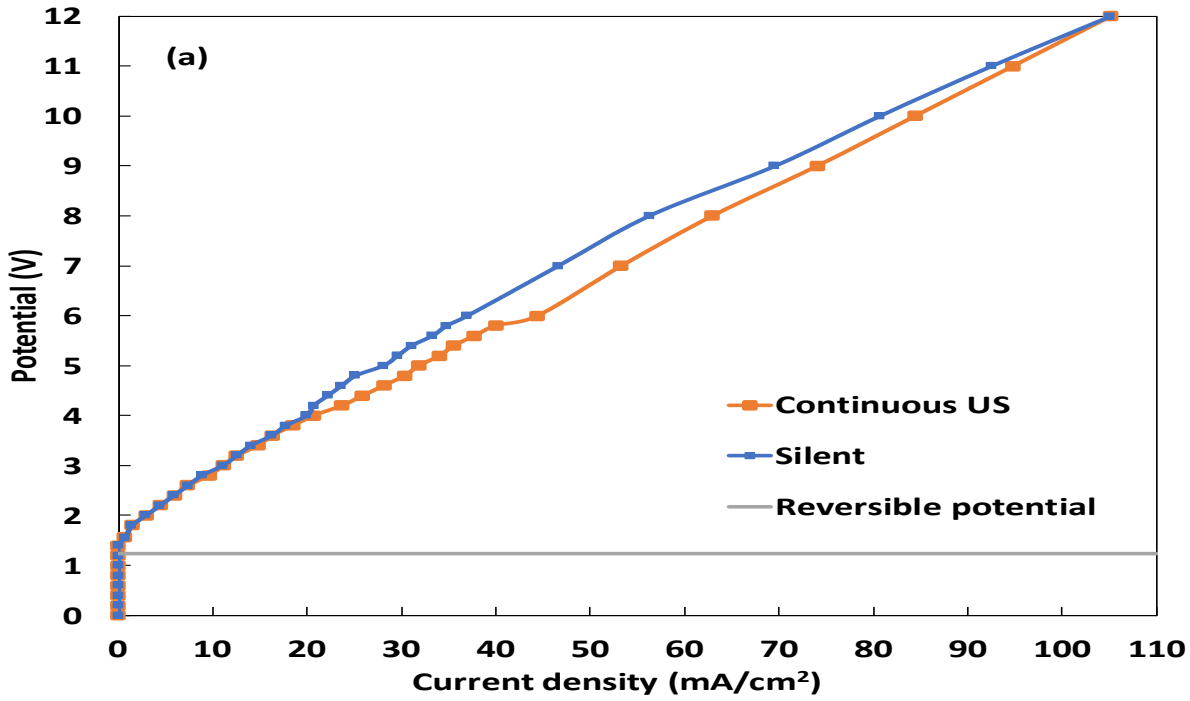

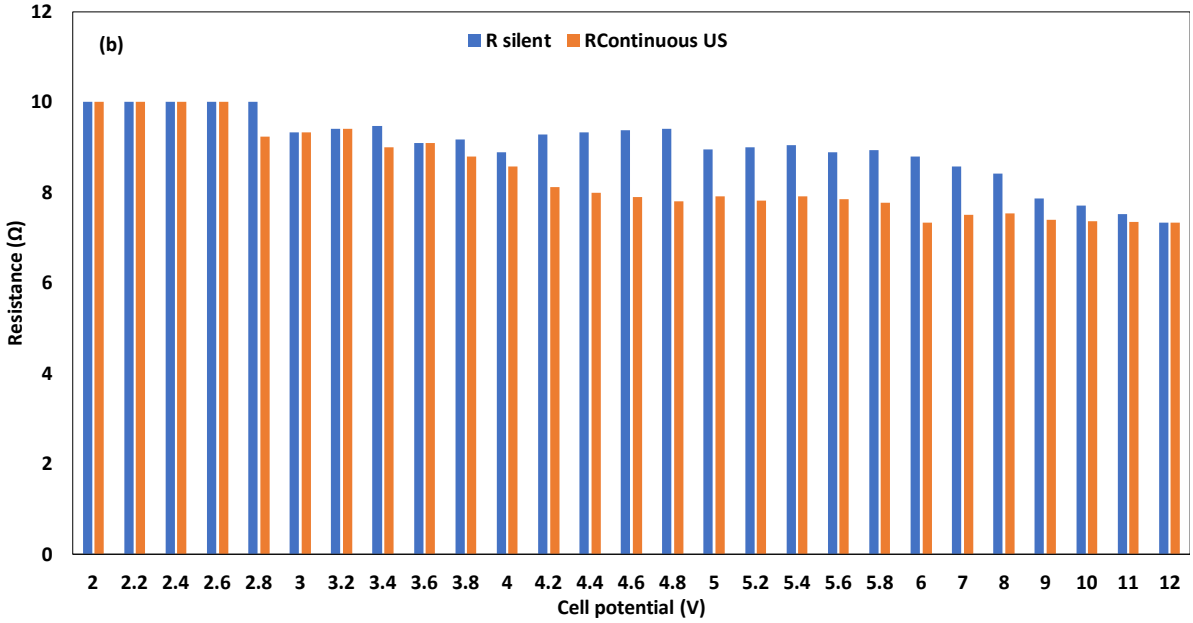

Figure 1.15 *Polarization curves under silent and ultrasound conditions (a), and variation of the experimental ohmic resistance vs. the cell potential (b).*

1.4.3.4 Acoustic cavitation in sono-electrolysis

The macroscopic effect of ultrasounds in the sono-electrolysis process being observed and measured in the previous sections, we suggest here to simulate the acoustic cavitation bubble evolving in the electrolyte, in order to assess the chemical and physical effects associated to it and elucidate the mechanism of action of ultrasounds at the microscopic scale. The calorimetric characterization presented in section 1.4.3.1 allowed the calculation of the effective acoustic amplitude of the wave travelling across the electrolyte, estimated at 98.95 kPa. The simulation of the oscillation of the single acoustic cavitation bubble is performed through the resolution of the system of non-linear differential equations presented earlier in section 1.3.6, considering the corresponding acoustic conditions (40 kHz, 98.95 kPa), the initial molar yields of oxygen, nitrogen, and water vapor, and the initial conditions:

$$\frac{dR}{dt}(t=0)=0$$

$$R(t=0)=R_0$$

Oxygen and nitrogen (forming air) are 27 and 12 folds more soluble in water than hydrogen, respectively, so the acoustic cavitation bubbles under consideration are assumed to form from gas nuclei composed of water vapor and air.

The numerical simulations over one acoustic cycle, i.e., 25 µs, consider the various ambient radii R_0 of the bubbles appearing in the population under 40 kHz, fairly represented by 20, 40, 60 and 80 µm, as shown in Table 1-6. Fig 1.16 presents the variation of the bubble radius as a function of time for the representative ambient radii.

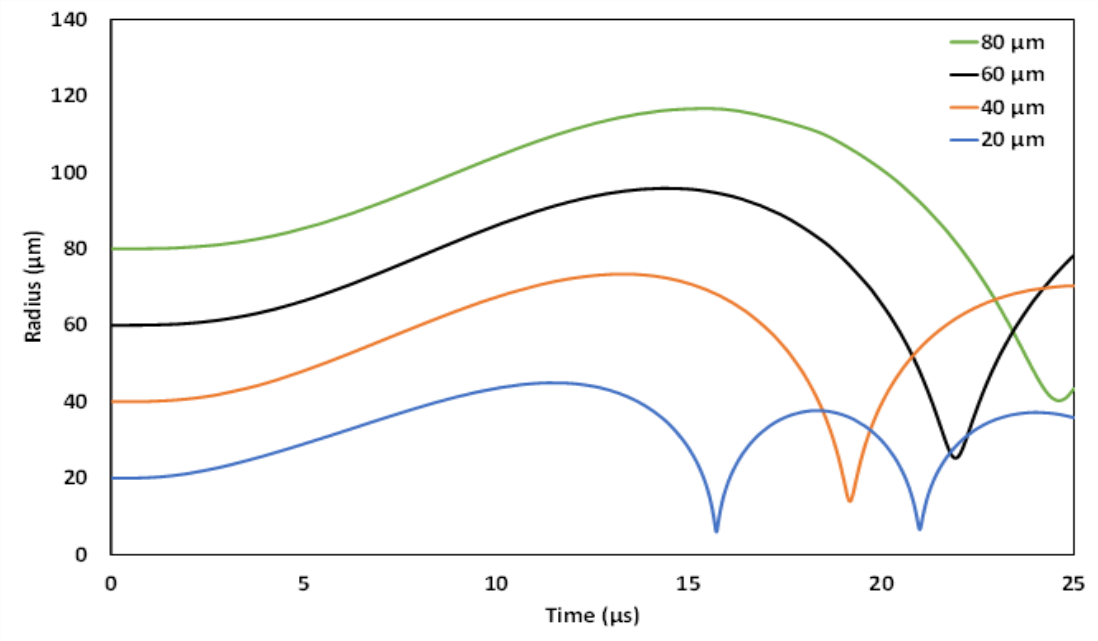

Figure 1.16 *Variation of the bubble radius vs. time over one acoustic cycle under 40 kHz and 98.95 kPa, for ambient radii of 20, 40, 60 and 80 µm.*

It is observed that the small bubbles having an ambient radius of 20 µm have a harsher oscillation with multiple bounces. The oscillation of the bubble becomes softer as the ambient radius increases from 20 to 80 µm. For instance, the expansion ratio decreases from 2.25 to 1.46 when the ambient radius increases from 20 to 80 µm. similarly, the compression ratio is reduced from 7.57 to 2.89. The maximum and minimum radii achieved during one acoustic cycle, and the related expansion and compression ratios are reported in Table 1-8 for the treated ambient radii.

Table 1-8 *Maximum and minimum radii and expansion and compression ratios in function of the ambient radii.*

R_0 (µm)	20	40	60	80
R_{max} (µm)	44.97	73.13	95.79	116.56
R_{min} (µm)	5.94	13.90	25.20	40.27
Expansion ratio	2.25	1.83	1.60	1.46
Compression ratio	7.57	5.26	3.80	2.89

The compression ratio is an indicator of the severity of the thermodynamic conditions attained inside the bubble volume, which allows an acceptable prediction of the extent of the chemical activity within the bubble as a microscopic reactor. This aspect will be investigated later in order to estimate the yield of hydrogen produced sonochemically at single bubble level and within the cathodic compartment. However, the physical effects, supposed to be main responsible of the observed reduction in the ohmic resistance under ultrasounds, require specific simulations, based on Eqs. 32, 33 and 34. Fig 1.17 reports the maximum powers associated to the radiated shockwave and the emitted microjet at the bubble collapse. The simulations are performed for each ambient radius in order to elucidate the overall behaviour of the bubble population. Fig 1.17 reveals that the exit microjet power increases with the increase of the ambient radius. To illustrate, it equals 0.56 W for an 80 µm bubble, while it is limited to 0.01 W at 20 µm. In contrast, the power associated to the radiated shockwave exhibits a maximum value of 0.18 W attained with bubbles of 40 µm of ambient radius. The comparison of the orders of magnitude of the powers of microjets and shockwaves demonstrate that relatively small bubbles are mainly concerned by the shockwave process and its contribution to the creation of turbulence within the electrolyte, which facilitates the hydrogen bubble detachment from the electrode surface, promotes the degassing process and liberates the reactional sites. Relatively large bubbles, i.e., having ambient radii of 60 and 80 µm, are more concerned by the microjetting process. The exit power of microjet is 1.76 times higher than the power of the radiated shockwave for bubbles of 60 µm of ambient radius, and 11.26 times higher when the ambient radius increases to 80 µm. considering the distribution of the number density of bubbles shown in Table 1-6, the bubbles population is mainly composed of 40 µm bubbles, the shockwave process is then predominant.

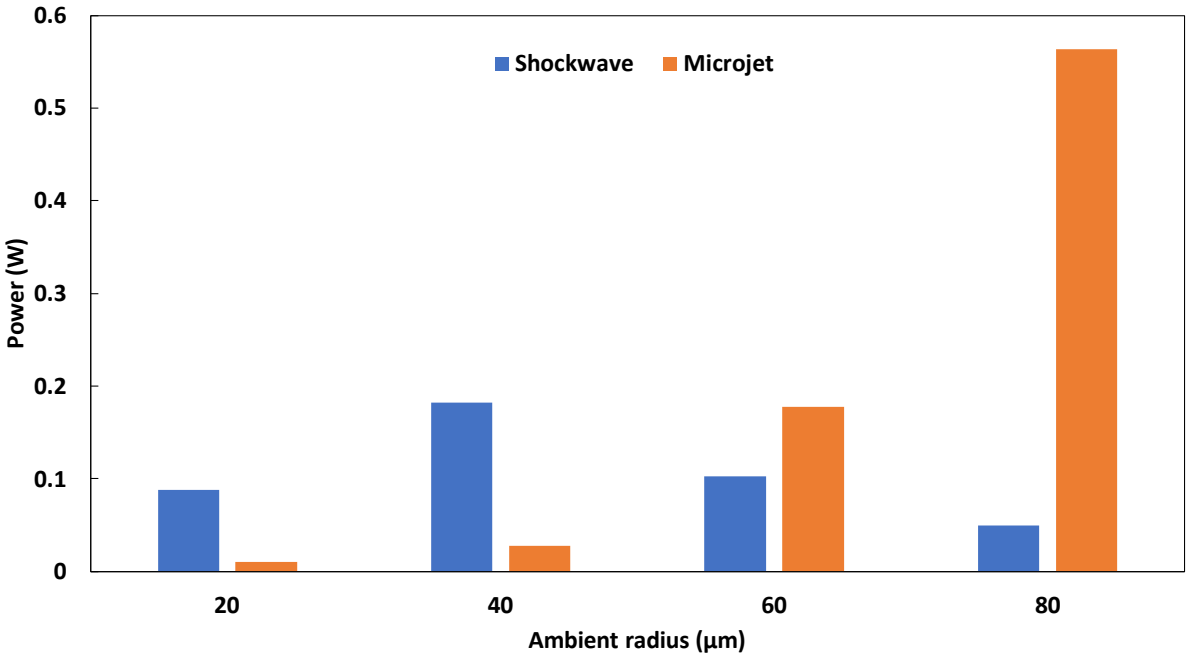

Figure 1.17 *Exit power of microjet and power of radiated shockwave at the bubble collapse according to the ambient radius.*

The contribution of the sonochemical pathway in the production of hydrogen is investigated through the simulation of the sonochemical production at the single bubble scale considering the covered ambient radii. Fig 1.18 (a) presents the evolution of the yield of hydrogen produced sonochemically over one acoustic cycle within a single acoustic cavitation of 20, 40, 60 and 80 µm. Although the small bubbles know the highest production, the yields remain negligible and do not exceed the sonochemical activity threshold fixed conventionally at 10^8 molecules/s [81,82]. Considering the number density of bubbles corresponding to each ambient radius, and the size distribution reported in Table 1-6, Fig 1.18(b) shows the yield of hydrogen produced by the end of the acoustic cycle for each ambient radius, it is clearly observed that the macroscopic sonochemical activity is negligible [52], and thus, the mass flow rate of hydrogen retrieved experimentally is only due to the electrochemical reaction presented in Eq 1.3.

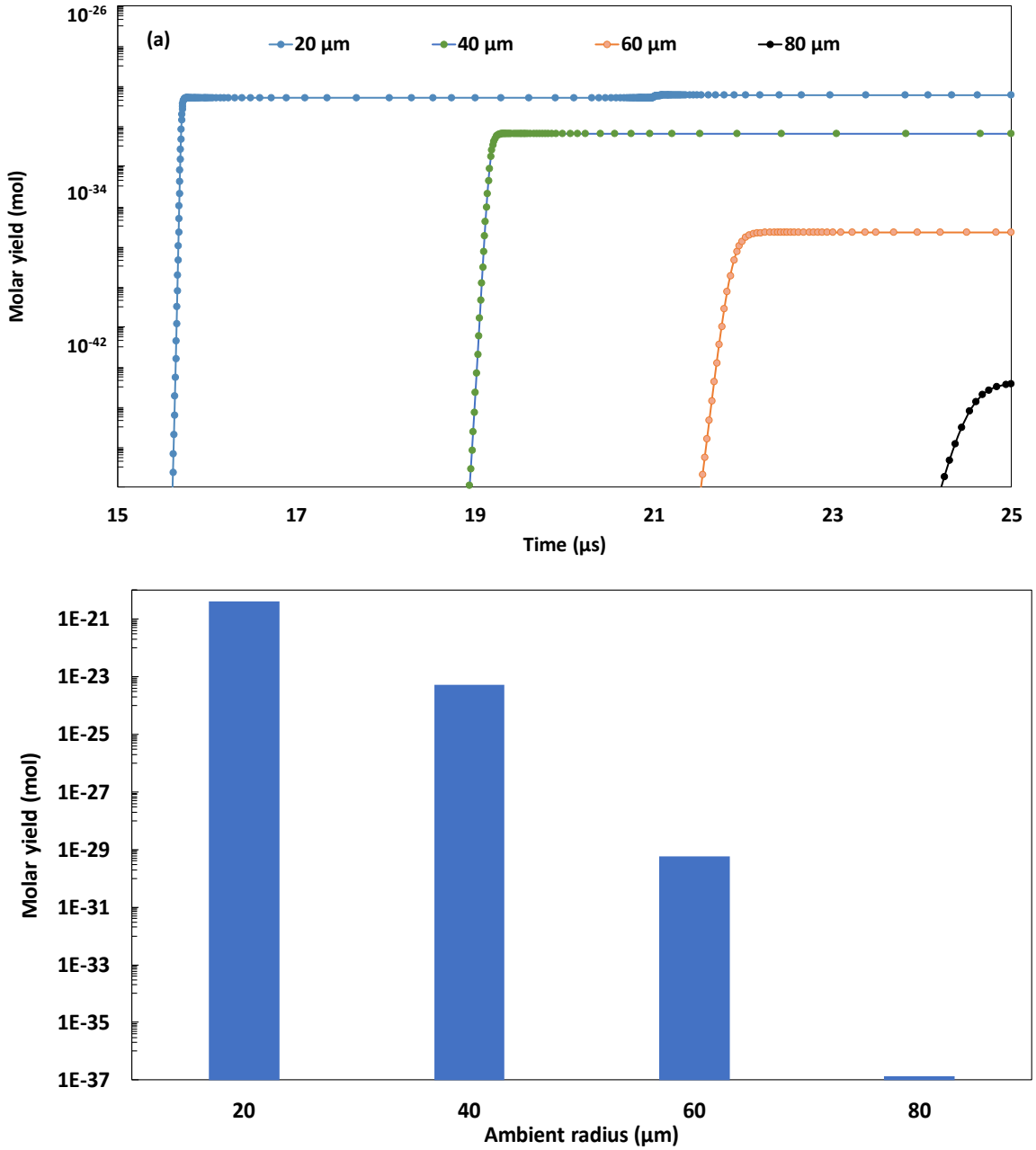

Figure 1.18 *Sonochemical production of hydrogen at the single bubble scale (a) and within the cathodic compartment (b) over one acoustic cycle according to the ambient radius.*

1.4.3.5 Effect of sonication in sono-electrolysis process

The microscopic analysis of the activity of the single acoustic cavitation bubbles composing the population demonstrated that the physical effects contribute exclusively to the reduction of the ohmic resistance in the sono-electrolysis process, while the sonochemical activity remains negligible. We suggest in the present section the examination of the impact of the reduction of electrodes coverage by bubbles on the value of the ohmic resistance, in order to make the link between the microscopic

events associated with the acoustic cavitation bubble and its macroscopic role in electrodes' cleaning. Fig 1.15(a) allowed, through the voltage decomposition method, to observe that the Ohmic resistance is predominant within the interval ranging from 3 to 12 V. Lower operational voltages lead to a cell operation governed by the activation overpotential, while higher voltages conduct to the predominance of concentration overpotential (which manifests with high current densities). On the other hand, sonication, through the physical effects induced by the acoustic cavitation bubble (mainly microjet and shockwaves), induces the desorption of bubbles from the electrodes surfaces and hence facilitates the gas recovery and liberates active sites for the electrochemical reactions. The action of ultrasounds concerns then the bubble resistance given in Eq 1.18, which is part of the ohmic resistance as seen in Eq 1.12. This explains the observable action of ultrasounds in the potential range from 3 to 12 V in Fig 1.15(b), corresponding to the ohmic resistance.

Fig 1.19 reports the results of the numerical simulation of the Ohmic and bubble resistance as functions of the fraction of electrode surface coverage.

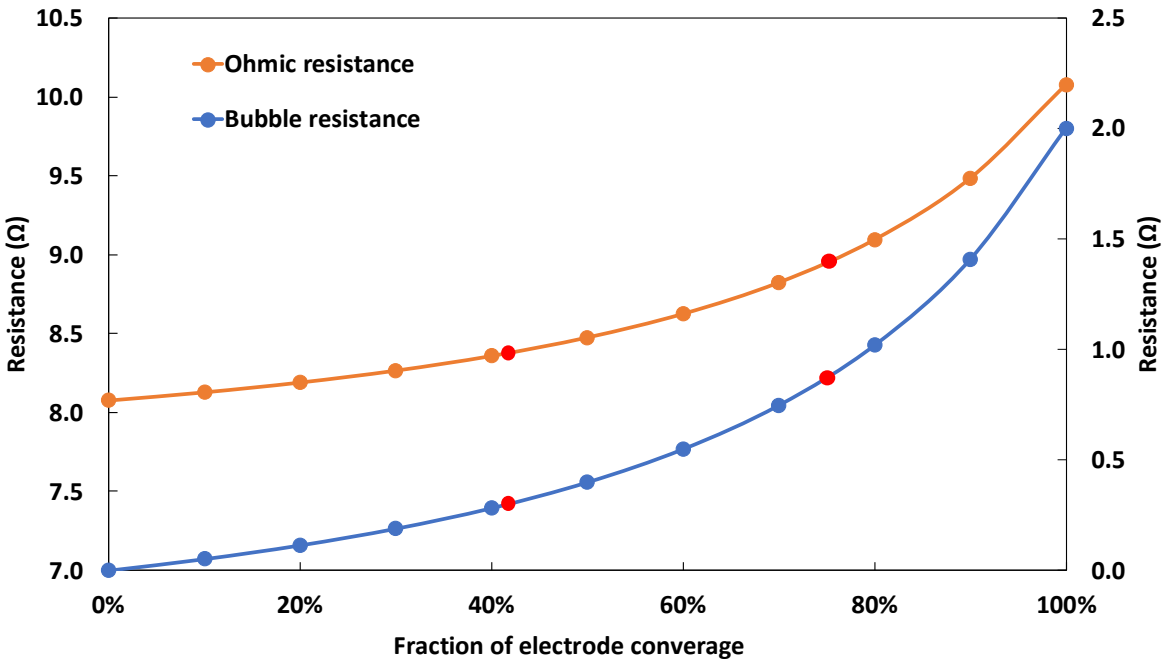

Figure 1.19 *Simulated evolutions of the Ohmic and bubble resistances in function of the fraction of electrodes' coverage*

The simulation demonstrates that when the electrodes' surfaces are totally accessible (in the absence of bubble coverage), the average ohmic resistance of the cell equals 8.08 Ω. It increases gradually to 10 Ω when the total surface is supposed to be covered by the bubbles, the bubble resistance neighbours in this case a value of 2 Ω. The highest increase in the bubble resistance, and consequently the ohmic resistance, is observed starting from a coverage of 60%.

On the other hand, the experiments returned the values of the ohmic resistances under silent conditions (9.03 Ω), and under ultrasounds (8.38 Ω), as mentioned in section 1.4.3.3. These values have been projected on the curve of ohmic resistance in Fig 1.19 to retrieve the corresponding fractions of electrodes' coverage. This projection (black triangles) returns 76% and 42%, respectively. It is then revealed that the integration of sonication reduces the electrodes' coverage by the bubbles from 76% to 42%, which corresponds to a decrease of 7.2% in ohmic resistance and 62.35% in bubble resistance.

Table 1-9 *Simulation results (potential in V and current in A)*

	$E_{rev}(T,P)$	U_{Ohm}	U_{Conc}	U_{act}	P_{cell}	I
0%	1.23	2.395	0.00033	0.37010	1.186	0.297
10%	1.23	2.396	0.00032	0.36979	1.179	0.295
20%	1.23	2.396	0.00032	0.36941	1.170	0.293
30%	1.23	2.397	0.00032	0.36896	1.160	0.290
40%	1.23	2.397	0.00031	0.36841	1.147	0.287
50%	1.23	2.398	0.00031	0.36772	1.132	0.283
60%	1.23	2.399	0.00030	0.36686	1.112	0.278
70%	1.23	2.400	0.00030	0.36574	1.088	0.272
80%	1.23	2.401	0.00029	0.36424	1.056	0.264
90%	1.23	2.403	0.00028	0.36218	1.014	0.253
100%	1.23	2.406	0.00026	0.35919	0.955	0.239

The simulation returns as well the values of the overpotentials and their variations with the electrodes' coverage by the bubbles. The results are in good agreement with the values retrieved experimentally, the activation voltage remains constant around 0.36 to

0.37 V, which is the value reported earlier in section 1.4.3.3.the power consumed by the cell decreases with the increase of the bubble coverage, due to the drop of the cell current at a fixed feeding potential. According to the previous analysis of Fig 1.19, the current passes from 0.268 to 0.286 when integrating sonication, which is equivalent to an increase of 6.72%.

1.5 Conclusion

The preliminary observations of the effect of the integration of ultrasound to the electrolysis system were performed using a Hoffmann cell design. The parametric study focused on the effects of the electrolyte concentration, the electrolyte type, and the temperatures of the electrolyte solution and the bath tempering the electrolyzer. With both KOH and NaOH electrolytes, varying the temperature of the solution demonstrated quasi-similar energetic performance as when operating at ambient temperature.

This was attributed to the compromise resulting of both kinetics improvement and power consumption increase, inducing a non-monotonous variation of the energy efficiency, which we can fairly qualify of slightly fluctuating and relatively stable with the Hofmann cell design. According to the preliminary tests, the integration of continuous sonication to the Hoffmann electrolysis system proved that using ultrasound avoids high temperature operation.

The experiments performed using the H-cell demonstrated that the geometry of the cell plays a major role in transport phenomenon of ions between the anodic and the cathodic compartments, creating a compromise between the effect of the surface tension, responsible of the degassing, and the ionic conductivity.

The analysis of the effect of the nature of the electrolyte revealed that NaOH leads to a better energetic performance using the H-cell. The acceleration in the electrochemical kinetics using KOH electrolyte, being more conductive than NaOH, proved to be insufficient to compensate the increase in power consumption, resulting in a slightly higher energy conversion observed with NaOH. However, the gain in the

ionic conductivity when using the KOH solution compensates the associated increase of the ohmic resistance and leads to an accelerated kinetics of hydrogen production.

In terms of electrodes' materials, the nickel foam leads to the highest rate reaching a value of 4.1 µg/s, followed by nickel, then stainless steel, then graphite. This observation was attributed to the fact that the porous structure of nickel foam allows the creation of more active sites for the electrochemical reactions. The sono-electrolytic configuration revealed a dependency of the indirect continuous sonication on the type of the electrolyte, which can be attributed to the lower surface tension of NaOH, as compared to KOH, facilitating the formation of unstable bubbles and enhancing consequently 37 the degassing, with all the tested electrodes. Besides, nickel foam revealed to lowest improvement due to sonication, which may be explained by the penetration of the formed acoustic cavitation bubbles, mainly by heterogeneous solid-liquid cavitation process, in the pores of the material, making their desorption and degassing more complex. Besides, the integration of the ultrasonic field in the case of nickel foam electrodes and KOH electrolyte would compensate the enhancement due of the temperature increase under silent conditions, and lead to a gain in the energy supplied to the heating module.

The drop in bubble resistance due to ultrasound was estimated under silent and continuous sonication. The highest decrease was observed with Nickel foam electrodes using KOH electrolyte, with a reduction rate of 64%. An equal rate was retrieved with graphite electrodes using NaOH solution, then with Nickel using the same electrolyte, with a rate of 55%. Overall, the energy efficiency was negatively impacted when replacing continuous sonication by pulsed one, though pulsed sonication was still effective compared to silent conditions. Thus, continuous sonication was proved to be the optimal mode to adopt in the sono-electrolysis system, both kinetically and energetically speaking.

Regarding the modelling part, in the investigation of a sono-electrolytic process based on membraneless alkaline electrolysis using an H-cell configuration, and indirect continuous sonication, with numerical modeling and simulation of physical and

chemical microscopic acoustic cavitation events and their macroscopic consequences on electrolysis in terms of electrodes' coverage by bubbles. The experiments demonstrated an average improvement in H_2 rate of 3.93% and a relative gain of 2.76% in energy conversion efficiency when integrating sonication. The polarization curves obtained experimentally under silent and ultrasounds conditions presented quasi-linear evolutions, related to the ohmic overpotential. The retrieved average ohmic resistance was estimated at 9.03 Ω under silent conditions, and 8.38 Ω under ultrasounds, which is equivalent to a drop of 7.2%.

Besides, the calorimetric characterization led to an acoustic intensity of 3263.6 W/m^2, and an acoustic amplitude of 98.95 kPa. This value was used in the numerical simulation of the acoustic cavitation bubble.

The simulations revealed that the exit microjet power increases with the increase of the ambient radius, while the power associated to the radiated shockwave exhibits a maximum at 40 µm. Moreover, the relatively small bubbles are mainly concerned by the shockwave process and its contribution to the creation of turbulence within the electrolyte, which facilitates the hydrogen bubble detachment from the electrode surface, promotes the degassing process and liberates the reactional sites. In contrast, relatively large bubbles are more concerned by the microjetting process.

The simulation of the sonochemical activity of the single bubble and bubble population proved that the yields of the sonochemically produced hydrogen remains negligible and do not exceed the sonochemical activity threshold fixed conventionally at 10^8 molecules/s.bubble.

The microscopic analysis of the activity of the single acoustic cavitation bubbles composing the population demonstrated that the physical effects contribute exclusively to the reduction of the ohmic resistance in the sono-electrolysis process.

Finally, the macroscopic simulation revealed through the projection of the experimental ohmic resistances retrieved under silent and ultrasound conditions on the simulated curve of the ohmic resistance as a function of the fraction of electrodes'

coverage, that the integration of sonication reduces the electrodes' coverage by the bubbles from 76% to 42%, which corresponds to a decrease of 7.2% in ohmic resistance and 62.35% in bubble resistance.

CHAPTER 2

"Membrane sono-electrolysis for hydrogen production"

CHAPTER 2: MEMBRANE SONO-ELECTROLYSIS FOR HYDROGEN PRODUCTION

2.1 Introduction

For the production of hydrogen, the electrolysis of water has several advantages such as being a non-polluting process when renewable energy sources are used, with a high degree of purity, a very simple process and a large number of resources [83]. At present, electrolysis can be classified as alkaline, solid oxide, PEM, AEM, acid-alkaline amphoteric, microbial and photoelectrochemical [84]. The use of polymer electrolytic membranes in fuel cell technology (PEM-FC) has become an interesting research topic because of its advantages of minimal pollutant generation, high power density and excellent conversion [85]. Other benefits of PEM electrolyzer include the ability to operate at high current densities at high voltages, reduced gas permeability, high ionic conductivity (0.1 ± 0.02 $S.cm^{-1}$), reduced thickness (20-300 μm) and possibility for high pressure processing to generate very pure hydrogen gas up to 99.995% [85,86]. However, the high cost of the catalyst, the need for an expensive membrane with only average durability and the expensive stack materials are the disadvantages of using a PEM electrolyser [84]. The membranes are supplied in a solid polymer exchange strip which separates the two electrodes from each other, acts as an ionic conductor and prevents any fuel from diffusing through. Good quality membranes are essential for durable operation and sufficient purity of the output [84]. Currently, perfluorosulphonic acid polymer membranes such as Nafion are accepted as the most widely used membrane, however, the cost of Nafion is relatively high, and its proton conductivity decreases at operating temperatures above 100°C.

Alkaline electrolysis is the simplest technique among the current available ones, usually a 30% w/w KOH (that is known to have a greater conductivity among other alkalis) solution or a 25% w/w NaOH solution is used and operated at 30-80°C. These units have efficiencies of around 60-80% and can produce hydrogen up to 99% pure [84]. Alkaline electrolysis uses porous separators between the two electrodes to ensure ionic

conductivity between the electrodes and to isolate the evolved gases at the anode and the cathode. This is particularly important when the cell is operated at a high pressure and/or under an asymmetrical pressure [87]. Polymer electrolyte membranes can be used as well as the electrolyte in alkaline electrolysis. Nevertheless, the thickness of the membrane, the ionic conductivity and the gas permeability are critical characteristics for the efficiency of water electrolysis, because they determine the ohmic drop and the gas permeability [62,88,89].

Operating at high current densities is an essential key for energy and performance enhancement of water electrolysis systems. Notably, there are plans for the development of electrolysis systems for commercial applications with a high current density in the future [90]. It should be noted, though, that the achievement of high current densities in low temperature electrolysis is hindered by the formation of hydrogen and oxygen bubbles within the electrolyte and on the electrodes surface. Bubbling on electrode surface decreases active reaction surface, hinders further electrochemical reaction and increases electrode potential. Therefore, the released gas should be timely removed from the active sites to release the available electrode surface area for the gas evolution reaction in order to carry out the effective electrolysis process [90].

Research on water electrolysis systems includes several strategies for the energy efficiency enhancement, namely by applying magnetic, light energy, ultrasonic and pulsed electric fields [91]. These later were the subject of numerous research work for the enhancement of membraneless alkaline electrolysis performances [4,20,23,92]. It was revealed that integration of ultrasound waves may contribute to increasing the energy conversion efficiency of hydrogen production up to 18% [18]. The mechanism of improvement was explained by the increase in mass transfer and electrode cleaning due to acoustic cavitation, microjets and shockwaves, which are the physical effects of the ultrasonic wave [16,25]. Kerboua et al.[93] performed a theoretical and experimental approach in order to elucidate the mechanism of acoustic cavitation in alkaline water electrolysis, concluding that sonication reduces the percentage of

electrode coverage by bubbles from 76% to 42%, resulting in a 7.2% reduction in ohmic resistance and a 62.35% reduction in bubble resistance through the physical effects of microjets and shockwave.

The aim of this chapter is to test a range of commercially available membranes and diaphragms, namely FAS-50, AMX, AEM, ME-11 and Zirfon UTP 500. The experiments were carried out using 25% KOH electrolyte at ambient temperature. Ultrasound was then integrated in water electrolysis to test its effect in the presence of membrane on the energy conversion efficiency and kinetics of hydrogen production. In the second part, a modelling approach was carried out in the case of optimal membrane in terms of energy efficiency, kinetics of hydrogen production and membrane stability, in order to assess the stability of the membrane under the experimental conditions, the ion exchange capacity study was also performed.

2.2 Experimental procedure

The same configuration used in section 1.2.1 (b) regarding the H-cell configuration was adopted in the present chapter at optimal conditions presented in Table 2-1. Commercial available membranes and diaphragm were used as follow: Zirfon diaphragm, AEM, AMX, FAS-50 in addition to ME-11 developed by ITM institute.

Table 2-1 *Adopted parameters and their variation in the setup*

Parameter	Variations
Electrolyte type	KOH
Electrolyte concentration (mol/L)	4.46
Temperature of the electrolyte (°C)	Ambient
Temperature of the bath (°C)	Ambient
Electrodes' material	Nickel
Membranes	AMX, FAS-50, AEM, Zirfon, ME-11
Sonication mode	Continuous

For each experiment, the membrane was immersed in a 25% KOH solution at 25°C for 1 h and the solution was changed twice every 30 min to prepare it for use in the alkaline electrolysis.

Similar to the electrolysis setup, sonication was performed using the 40 kHz, 60 W_e ultrasound bath, which is the same bath used in our previous studies [93,94]. For each configuration, the experiments were repeated several times in order to ensure the repeatability of the results.

Ionic exchange capacity

Ion exchange capacity is the molecular weight of the ion exchange membrane per unit weight. The membrane was immersed in a 25% KOH aqueous solution for 2 days at 40 ±2°C with agitation to replace the ion exchangers in the membrane with OH groups. The ion-exchanged membrane was then washed in distilled water for 4 hours. The cleaned membrane was placed in 50 mL of 0.1M HCl aqueous solution, sealed and left for 24 hours. During this time, ion exchange takes place between the acidic aqueous solution and the ion exchange membrane.

The ion exchange capacity (IEC) was measured by taking a certain amount of the above aqueous solution and titrating it with 1M NaOH aqueous solution. The IEC was then calculated according to Eq 2. 1 [95].

$$IEC = \frac{M_{i,HCl} - M_{e,HCl}}{Wm} \tag{2.1}$$

2.3 Modeling and simulation procedure

The model used in the numerical modeling is the same model that has been used in section 1.3 based on the voltage source. In the case of membrane electrolysis, the resistance of the membrane is involved in the ohmic voltage and is generally related to the thickness σ_{dia}, the active area A_{dia} the porosity P_{dia} and the tortuosity τ of the diaphragm/membrane and the conductivity of the electrolyte. The resistance of the diaphragm/ membrane can be expressed according to Eq 2. 2 [96]

$$R_{mem} = \frac{\delta_{dia}}{A_{dia}\sigma\mathrm{el}} \times \frac{\tau}{P_{dia}} \tag{2.2}$$

It is worthy to mention that the mathematical model will be simulated with the most performant membrane/diaphragm according to the experimental results.

2.4 Results and discussion

2.4.1 Experimental results

The results of the energy conversion efficiency (a) and kinetics of hydrogen production (b) of membrane water electrolysis under silent and sonicated conditions are plotted in Fig.2.1 (a) and (b). As the experiments were repeated several times, the average result for each series of experiments is shown for each membrane type.

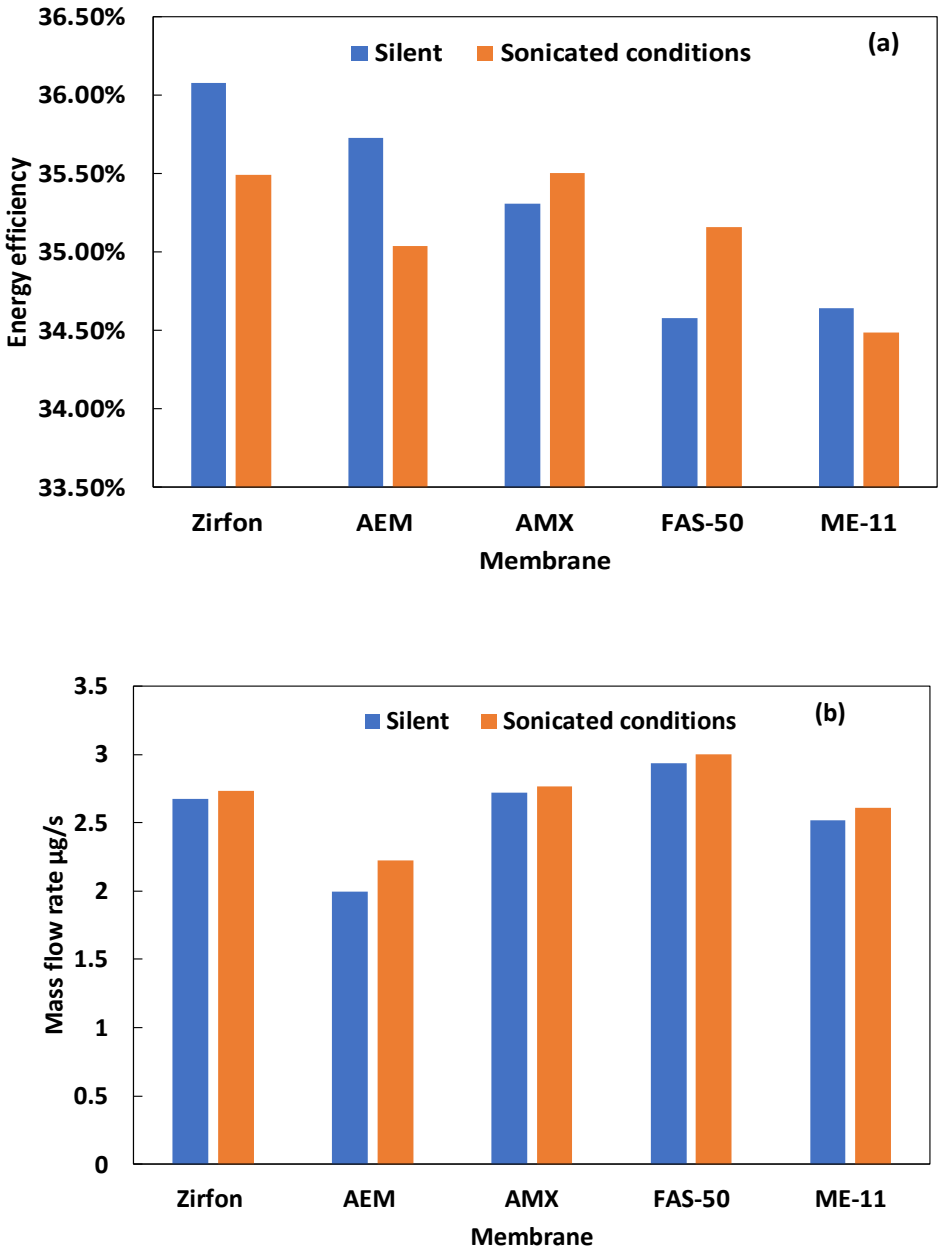

Figure 2.1 *Experimental results of silent and sonicated membrane electrolysis hydrogen production in terms of (a) energy efficiency and (b) kinetics of hydrogen production*

It can be seen from Fig. 2.1 that the highest energy efficiency of the process was achieved according to the following order: Zirfon membrane> AEM> AMX> ME-11 >FAS-50. However, the integration of ultrasounds did not show any improvement in most cases, e.g., with Zirfon, AEM and ME-11 membranes, the energy efficiency was shown to be 0.5% - 2% higher under silent conditions. For AMX and FAS-50 membranes, however, slight improvements of 0.6% and 1.6%, respectively, were observed under sonicated conditions.

In terms of hydrogen production kinetics, ultrasounds brought a slight enhancement in all cases of the used membranes. While the highest mass flow rate was recorded using the FAS-50 membrane, with 3 µg/s and 2.9 µg/s under sonicated and silent conditions, respectively. This was followed by AMX and Zirfon that showed close values of mass flow rate in the range of 2.68 and 2.72 µg/s and 2.73 and 2.77 µg/s under silent and sonicated conditions, respectively.

2.4.2 Modeling results

The results of the simulation of membrane electrolysis under the optimal conditions in terms of membrane, temperature and electrode material are shown in the following figures. Fig. 2.2 (a) shows the variation of the main resistances as a function of the electrode coverage by the bubbles. It can be seen that the ohmic resistance is mainly determined by the membrane resistance, which accounts for 54.98% - 86.39% of the ohmic resistance. Whereas the bubble resistance reaches a maximum of 36.36% of the ohmic resistance value when the coverage of the electrodes is 100%. In addition, the ohmic resistance increases as the bubble coverage of the electrodes increases, from 0.37 Ω to 0.58 Ω at the maximum bubble coverage coefficient.

In order to understand the effect of the increase in the ohmic resistance on the ohmic voltage, the simulation results have been plotted in Fig. 2.2 (b). It can clearly be seen that the increase in the ohmic resistance, and therefore the increase in the coefficient of coverage of the electrode by the bubble, leads to a variation in the ohmic voltage. However, this variation is not significant and does not exceed 0.02% when the bubble coverage reaches its maximum.

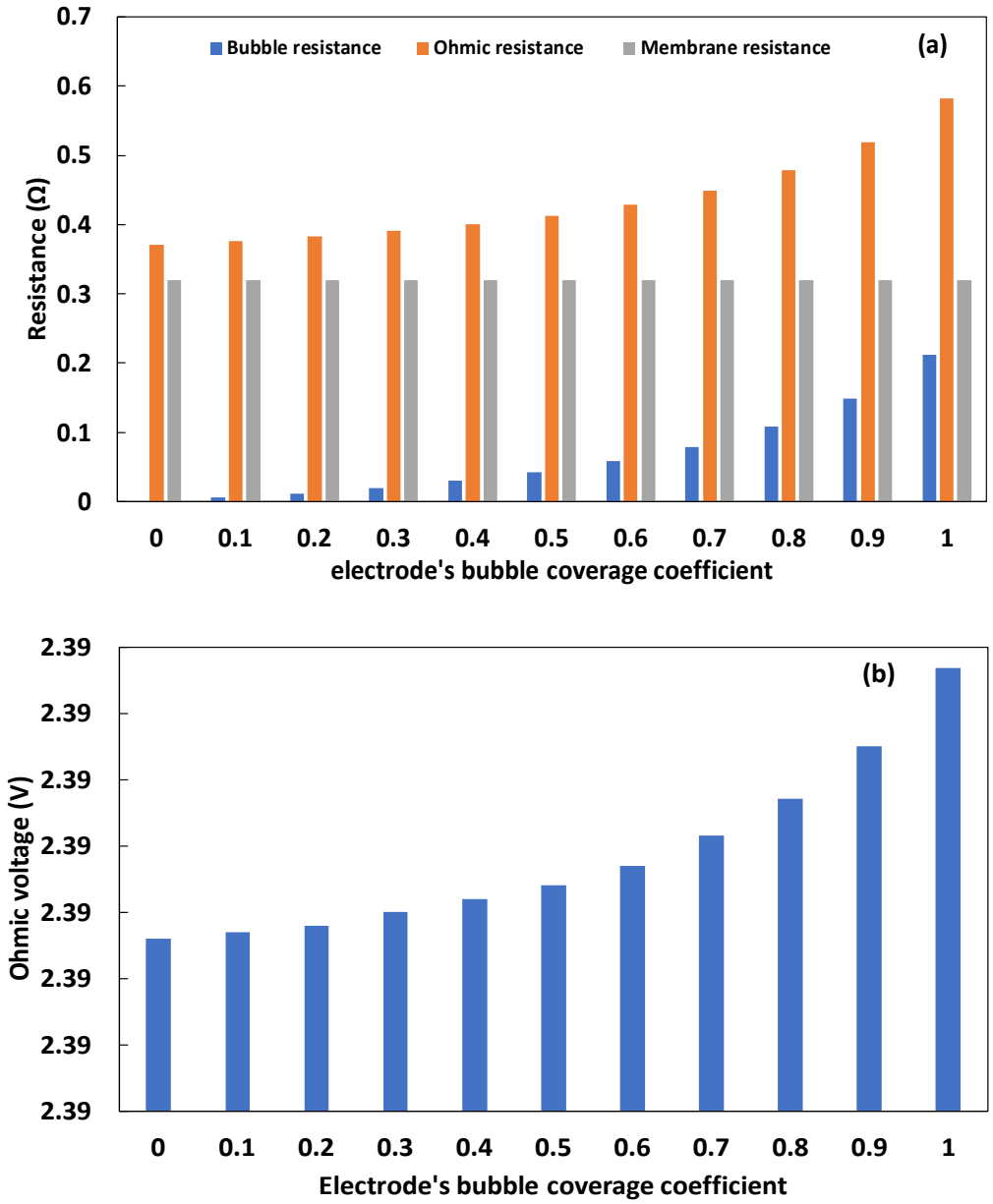

Figure 2.2 *Simulation results of the variation of ohmic, bubble and membrane resistances (a) and ohmic voltage (b) in function of electrode's bubble coverage coefficient.*

It was reported in our earlier studies [93,97] that the integration of sonication in a membraneless electrolysis reduces the bubble and ohmic resistances by reducing the bubble coverage on the electrode surface, thereby increasing the energy efficiency of the electrolysis. However, in the presence of the Zirfon diaphragm, the effect of bubble coverage reduction was ignored due to the high value of diaphragm resistance in the system. Therefore, the effect of sonication on the energy efficiency of membrane electrolysis could not be considered, which is in good agreement with the experimental results obtained.

The effect of sonication on the kinetics of hydrogen production was also simulated. Fig 2.3 shows the variation of the mass flow rate of hydrogen produced as a function of the bubble coverage of the electrode. As it can be seen, the rate of gas production is affected by the increase in bubble coverage, as the total coverage of the electrode reduces the gas production rate by a percentage of 2.7% compared to the free bubble electrode. It has been reported in the literature [16,25] that ultrasound induces a stirring effect within the electrolyte and a cleaning and degassing effect on the electrode surface, leading to a more free surface for more electrochemical reactions to occur, which in turn results in a slight improvement in the kinetics of hydrogen production.

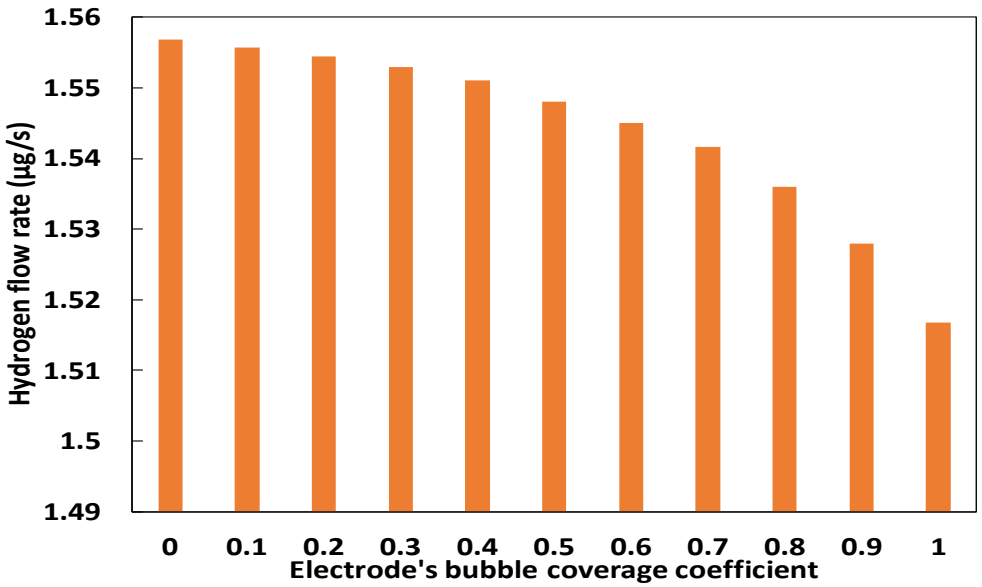

Figure 2.3 *simulation results of the variation of the mass flow rate of hydrogen production in function of the electrode's bubble coverage coefficient.*

2.4.3 Ionic exchange capacity

The ion-exchange capacity (IEC) represents the total of active sites or functional groups responsible for ion exchange in polymer electrolyte membrane. The results of the ionic exchange capacity for the different membranes/diaphragms used in the study are presented in Table 2-2. In our study, the stability of the commercially used membranes in 25% KOH electrolyte was evaluated based on the decrease of the ionic exchange capacity of each membrane. The reduction in the ionic exchange capacity was considerable for the four types of membranes AMX, FAS-50, AEM, and ME-11 as

compared to the values announced by the manufacturers. Zirfon UTP 500 was the only membrane adapted for alkaline electrolysis, as it was originally manufactured for water electrolysis in 25-30% of alkaline solutions. Moreover, this separator proved its efficiency in the present study.

Table 2-2 *Ionic exchange capacity of the membranes*

Membrane	Ion exchange capacity (meq/g dry membrane)
Zirfon®	0.028
AMX	0.07
FAS-50	0.28
AEM	0.02
ME-11	0.1

2.5 Conclusion

In this chapter, the effect of sonication on the membrane electrolysis for hydrogen production was studied. The experimental results showed that the Zirfon separator performed the best among the other membranes used in alkaline water electrolysis in terms of energy efficiency and hydrogen production kinetics, in addition to its stability at high alkaline conditions among the other membranes/diaphragms.

Furthermore, the integration of sonication in the presence of the membrane does not show any improvement on the energy efficiency of the process. However, the propagation of ultrasound within the electrolyte has shown a better kinetics of hydrogen production.

The modelling results showed that the effect of ultrasound in reducing the bubble coverage of the electrodes and thus reducing the ohmic resistance was not significant compared to the high resistance of the Zirfon diaphragm. On the other hand, the desorption and stirring effect resulting from the propagation of ultrasound within the electrolyte resulted in an improvement of the hydrogen production kinetics despite the presence of the diaphragm.

CHAPTER 3

"PV supplied sono-electrolysis for green hydrogen production"

CHAPTER 3: PV SUPPLIED SONO-ELECTROLYSIS FOR GREEN HYDROGEN PRODUCTION

3.1 Introduction

As the storage and transport of hydrogen is proved to be environmentally friendly with negligeable effects, it can be assumed that the production of hydrogen is an important criteria to define its environmental sustainability of the whole hydrogen chain [98]. Consequently, hydrogen is a green energy carrier only if it is produced from renewable sources [98]. One of the best options to produce green hydrogen and reduce water electrolysis costs is to couple photovoltaic panels with electrolyzers. The combined photovoltaic-electrolysis systems for hydrogen generation first appeared in 1970 [99], and is currently considered as a mature technique [100]. In such systems, the main source of energy is the solar radiation available at the sites, the electrolyzer is powered by photovoltaic panels that produce direct current [101]. The output of the photovoltaic panels is related to the solar radiation, ambient temperature and humidity while the system's performance depends mainly on the PV power conversion efficiency. The output current generated from the PV system is directly injected to the electrolyzer in order to split water into hydrogen and oxygen [98]. Numerous investigations and researches have been conducted based on both mathematical modelling and experimental studies of the PV and the electrolyzer system [102].

Nowadays, commercial electrolyzers achieve an efficiency range from 60% to 85%, while photovoltaic cells reach 18%, thus, the overall photovoltaic-electrolysis system's efficiency may be higher than 10% [103]. Since the system efficiency depends mainly on the efficiency of both the PV generator system and the electrolyzer, there have been several studies that concentrated on the optimization of these key parameters [104]. For instance, the literature counts numerous studies of the direct and indirect combination of solar PV-electrolysis. In a typical photovoltaic electrolysis system, the photovoltaic generator and the electrolyzer can be directly connected to each other without additional components, or by means of MPP trackers, regulator and batteries [105]. Generally, in directly connected systems, there is a time lag between the MPP

characteristic of the output PV and the I-V characteristic of the input electrolyzer [100]. Furthermore, one of the major disadvantages of solar-hydrogen hybrid systems is the inadequacy of the current efficiency which makes it hard to be economically competitive with hydrogen produced from fossil fuels [101]. Therefore, additional MPP trackers are added in order to solve this problem while the integration of batteries seems to be a promising solution in order to make the use of off-grid renewable energy easier by avoiding the instabilities induced by the intermittency of PV outputs [105]. However, from a techno-economical perspective, battery-assisted system causes a power loss owing to the DC/DC convertor, in addition to the sensitivity of DC/DC convertor and batteries to temperature changes, which increases the capital and maintenance costs [104].

A key performance indicators shows that proton exchange membrane may be a better technology for solar-assisted system owing to its short start-up, full load range and fast dynamics [105]. It is possible to achieve a power transfer efficiency as high as 99% by connecting the electrolysis cells in series and in parallel [106]. This method allows to align the polarization curve of the electrolyzer closely with the curve connecting the maximum power points of the PV system at different radiation intensities [100,105].

Literature counts tens of studies that treated experimentally the sono-electrolysis for hydrogen generation, while to the best of our knowledge, no research studies explored the performance of sono-electrolysis supplied by PV, using mathematical modelling and simulation associated to experiments. Thus, the main objective of the current study is to investigate numerically the action mechanism of ultrasounds in sono-electrolysis, with a focus on green hydrogen production based on PV power supply. The experiments are carried out using an H-cell membraneless electrolyzer and indirect continuous sonication. The electrochemical cell was coupled to the photovoltaic module at optimal conditions, and results under silent and ultrasounds modes were compared and analysed both experimentally under real solar radiation conditions, and numerically. The integrated operation of the PV-sono-electrolysis system is approached based on the solar radiation, which allows a predictive real time follow up of the performance of the combined process.

The main objective of this chapter is to numerically investigate the mechanism of action of ultrasounds in sono-electrolysis with a focus on green hydrogen production based on PV power supply under static and dynamic conditions. The approach is based on a parametric study of the effect of sonication on the electrolyte resistance, the concentration overpotential and the mass flow rate of produced hydrogen. The experiments are carried out using a membraneless H-cell electrolyzer and indirect continuous sonication. The electrochemical cell was coupled and fed with a photovoltaic module under optimal conditions of dissolved salt, electrolyte concentration and temperature bath temperature and electrode material in terms of kinetics of hydrogen production and energy conversion efficiency, which are retrieved from our previous study, and the results under silent and ultrasonic modes were compared and analysed both experimentally under real solar radiation conditions, and numerically. The integrated operation of the PV-sono-electrolysis system is approached on the basis of solar radiation, which allows a predictive real-time follow-up of the performance of the combined process.

3.2 Experimental procedure

The electrolyser used in this study is the glass H-cell. The experiments are carried out using a membraneless configuration. at optimal conditions of temperature, electrolyte concentration and electrodes' material and structure.

The power supply consists of a photovoltaic panel connected to a Maximum Power Point Tracking regulator MPPT. A 30 W monocrystalline solar panel is used with the characteristics reported in Table 3-1. The MPPT regulator is connected to a solar battery of a capacity of 90 Ah. The detailed schematic of the solar sono-electrolysis system for hydrogen production is presented in Fig 3.1.

Table 3-1 *Parameters related to the PV panel*

Parameter	Value	Reference
Solar cells type	Monocrystalline	ET Solar
Short circuit current (Isc)	1.8 A	ET- M53640
Open circuit voltage (Voc)	21.52 V	
Maximum output current (Imp)	1.69 A	
Maximum output voltage (Vmp)	17.72 V	
Maximum power (Pmax)	30 W	
Number of serie connected cells (Ns)	36	
Number of parallel connected cells (Np)	1	
Diode ideality factor	1.3	[32]
Serie resistance (Rs)	0.25 Ω	
Shunt resistance (Rp)	198.1 Ω	
Current coefficient	+ 0.065 %/ °C	[107]
Voltage coefficient	-0.5 %/°C	[107]

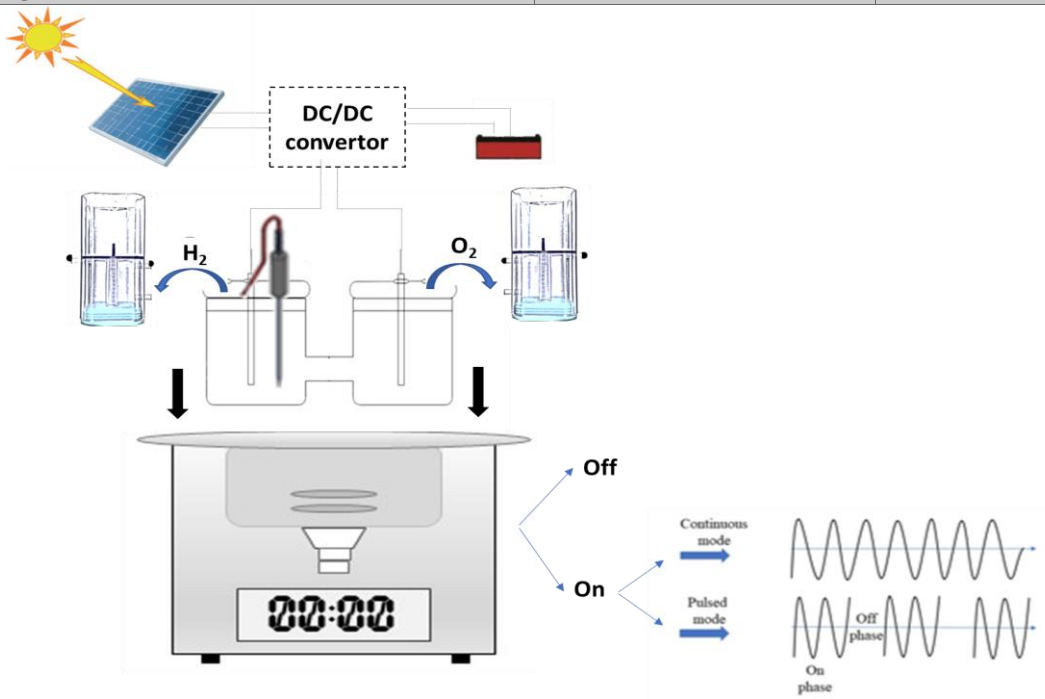

Figure 3.1 *Schematic of the experimental setup of the sono-electrolyzer supplied by PV*

3.3 Semi-empirical modelling and simulation procedure

3.3.1 PV supply

The current I produced from the PV generator can be given by the Eq 3. 1 [108].

$$I = I_{pv} - I_d - I_{sh} \tag{3.1}$$

Where I_{pv} is the light-generated current of the PV cell I_d and I_{sh} are the current of the diode and current crossing shunt resistance respectively [108,109]. These parameters can be expressed through Eq 3. 2, Eq 3. 3 and Eq 3. 4 [108,109]:

$$I_{pv} = \frac{(I_{pv0} + K\Delta T)G}{G_0} \tag{3.2}$$

$$I_d = I_0\left(\exp\left(\frac{R_s I + V}{V_t a}\right) - 1\right) \tag{3.3}$$

$$I_{sh} = \frac{V + R_s I}{R_p} \tag{3.4}$$

I_0 and ΔT are the diode saturation current and the variation in temperature at real and standard conditions that are given according to the Eq 3. 5 and Eq 3. 6 [108]:

$$I_0 = \frac{I_{sc,n} + K_I \Delta T}{\exp\left(\frac{V_{ocn} + K_V \Delta T}{a V_t}\right) - 1} \tag{3.5}$$

$$\Delta T = T_p - T_n \tag{3.6}$$

Here, V_{ocn}, K_I and K_V are the nominal open circuit voltage, current and voltage coefficient %/°C respectively.

$I_{sc,n}$ is the nominal short circuit current and V_{tn}presents the thermal voltage at standard temperature and is given by [32] in function of Boltzmann constant K_B, the charge of the electron q and the temperature at standard conditions T_n, as indicated in Eq 3. 7.

$$V_{tn} = \frac{K_B T_n}{q} \tag{3.7}$$

The equations related to the PV power supply and the sono-electrolysis response are implemented into a MATLAB code. The simulation is then performed considering the real incident solar radiation measured using a luxmeter.

3.3.2 Dynamic solar radiation conditions

Solar radiation model

The global radiation on tilted surface G is calculated according to Eq 3. 8 [110].

$$G = D_\beta + B_\beta + R_{ra} \tag{3.8}$$

Where D_β is the diffuse radiation, B_β and R_{ra} are the beam and reflected radiation in the adopted model, the diffused radiation D_β is estimated according to the anisotropic model of Hay [110] as shown in Eq 3. 9 and Eq 3. 10.

$$D_\beta = D_d(f_{Hay}\left(\frac{cos\theta}{cos\theta_z}\right) + (\frac{1+cos\beta}{2})(1 - f_{Hay}) \tag{3.9}$$

$$f_{Hay} = \frac{D_b}{E_{xt}} \tag{3.10}$$

R_{ra} is the reflected radiation which is the fraction of global radiation that is reflected by the Earth's surface and any other obstructing object and is calculated according to Eq 3. 11.

$$R_{ra} = H\rho_A\left(\frac{1-cos\beta}{2}\right) \tag{3.11}$$

The direct beam irradiance on a tilted surface can be calculated using Eq 3. 12.

$$B_\beta = r_\beta D_b \tag{3.12}$$

Where r_β represents is the ratio of the hourly radiation received by an inclined surface to that received by a horizontal surface outside the Earth's atmosphere and is calculated using Eq 3. 13 [110]:

$$r_\beta = \frac{E_{0\beta}}{E_{xt}} \approx \frac{cos\theta}{cos\theta_z} \tag{3.13}$$

In the previous equations, E_{xt}, θ and θ_z are the extraterrestrial radiation, the incidence angle and the zenith angle that are calculated according to a specific equations [110].

3.3.3 PV supplied electrolysis

PV-supplied electrolysis is mathematically simulated by introducing the experimental or theoretical value of global radiation as indicated by Eq.3.8, based on the components detailed in Eqs. 3.9, 3.11 and 3.12, to the algorithm dedicated to the study of the static or dynamic response of the considered PV panel. In both cases, this relies on the resolution of the non-linear Eq. 3.1 to retrieve the unknown value of delivered current, accounting for Eqs.3.2 to 3.4, by scanning the range of potentials from 0 to V_{oc}. Under

dynamic meteorological conditions, the procedure is repeated as a function of time for all the covered time interval.

3.3.4 Integration of sonication

The numerical approach takes into account the effect of sonication on the electrolyte resistance, the concentration overpotential and the mass flow rate of hydrogen produced. This has been done by considering the variation of the bubble coverage of the electrode, the diffusion coefficient and the Faraday efficiency under different values of solar radiation. The numerical approach of sono-electrolysis is based on the equations presented in section 1.3.

3.4 Results and discussion

3.4.1 Static conditions

3.4.1.1 Experimental kinetics of hydrogen production

In order to verify the repeatability in terms of feeding currents and resulting cell voltages under PV power supply, the experiments have been repeated three times each and the results are reported in Fig 3.2, with an estimation of the relative standard deviations. The same procedure was followed under silent under ultrasounds conditions (with both continuous and pulsed modes).

Fig 3.2 (a) and (b) depict the feeding current and resulting cell voltage of the three repeated experiments of PV supplied alkaline electrolysis conducted under silent, continuous and pulsed ultrasounds. The average values are also shown for each case in the same figure. The experiments were performed by exposing the photovoltaic panel to normal solar radiation around solar noon during the last week of May 2022. Each series of experiment was repeated under identical conditions, while experiments performed under silent, then continuous then pulsed conditions were carried out under slightly different incident solar radiation due to climate change. However, the reported results were selected so as the cell voltage remains similar, around 5.95 to 5.96 V, as shown in fig 3.2 (b). The corresponding incident solar radiations were measured using a luxmeter and converted into W/m^2. Accordingly, the silent alkaline electrolysis was

performed under 827 W/m^2, while continuous and pulsed sono-electrolysis were carried out under 938.5 and 899 W/m^2, respectively.

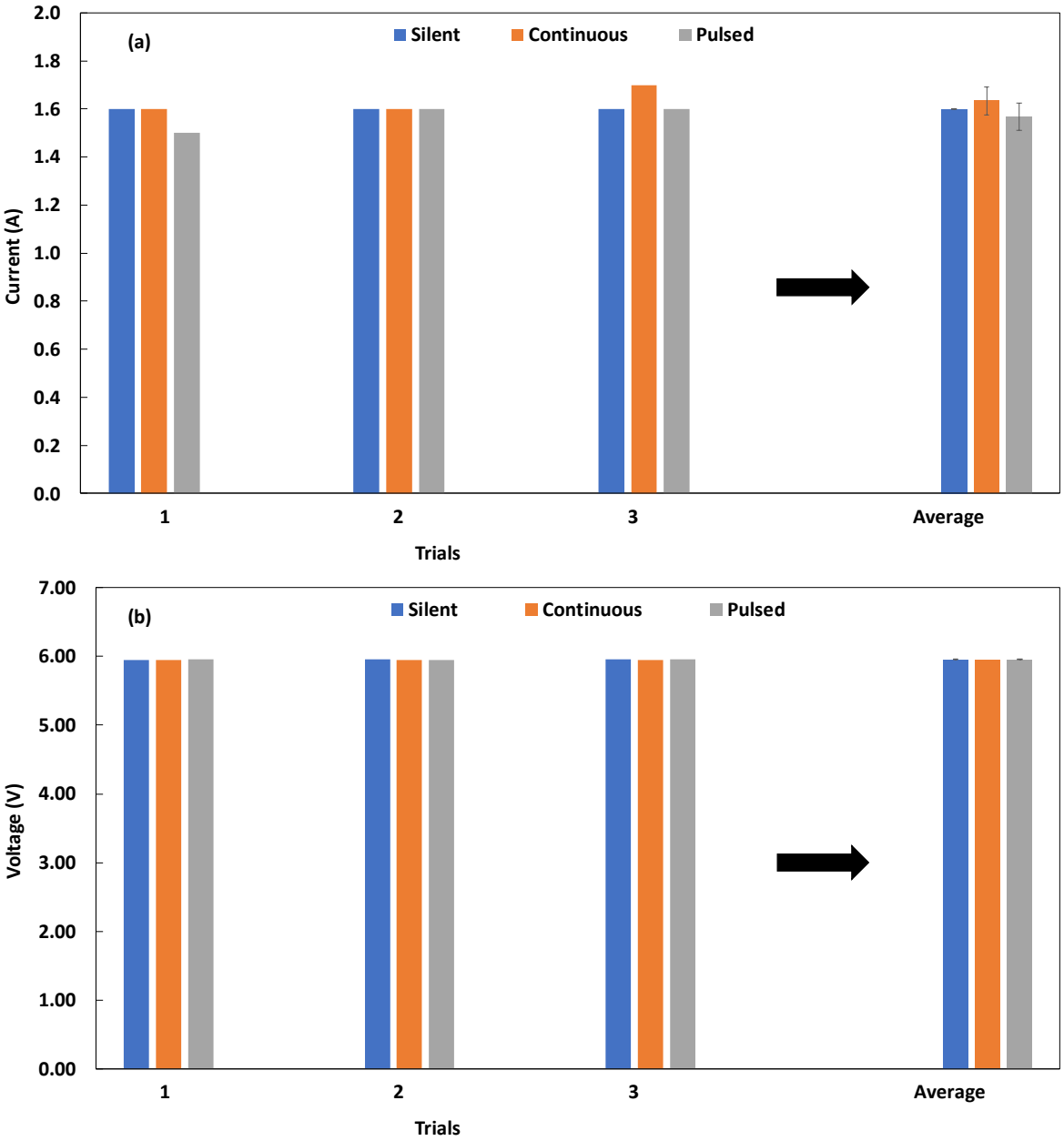

Figure 3.2 *Comparison of PV-solar supplied water electrolysis and water sono-electrolysis processes for hydrogen production in function of mass flow rate (a) and PV's output voltage (b) using nickel electrodes and 25% of KOH electrolyte (wt%).*

In terms of feeding current, the relative standard deviations resulting from the series of repeated experiments were estimated at 0.1%, 3.53% and 3.63% under silent, continuous and pulsed ultrasounds, respectively. The input cell voltage resulting from the PV power supply under the aforementioned global solar radiations has been measured experimentally over the repeated experiments, the recorded relative

standard deviations were estimated at 0.1%, 0% and 0.1%. The repeatability is then demonstrated for both key parameters.

The average cell resistance in each case has been determined from the previous average measurements using the Ohm law. Under silent conditions, the electrolysis cell manifest a total resistance of 3.72 Ω. The integration of continuous sonication results in a total cell resistance of 3.65 Ω, while pulsed ultrasounds lead to a value of 3.79 Ω. These average experimental values will be analysed using the mathematical model, based on an electrical equivalent approach.

The application the kinetic equation for one cell, with the average values of the cell currents measured experimentally under silent, continuous and pulsed ultrasounds conditions, reveals that the Faraday efficiency defined as the ratio of the experimentally detected amount of hydrogen gas to the amount of theoretically generated gas equals 1 [111], with quasi similar values around 16 µg/s. This finding is in good agreement with the literature reporting high Faradic efficiencies neighboring 100% at relatively low current densities [112].

Fig 3.2 (b) reports the values of the cell voltage resulting from the PV power supply. The PV supply acts as a current source [113], and the outputs resulting from the MPPT generator are considered in the analysis of the experimental and simulation results. Fig 3.2(b) indicates that similar cell potentials are retrieved under the three studied cases, although incident solar radiation and feeding direct current are not identical. Hence, for similar overpotentials, the highest solar radiation received by the panel was recorded with the continuous sono-electrolysis experiment, inducing a higher cell current and consequently a more important electrochemical kinetics and a higher mass flow rate of hydrogen. This will be analyzed in the mathematical modeling and simulation.

3.4.1.2 Numerical comprehension of the sono-electrolysis performance

a) Silent conditions

The parameters of the ET- M53640 solar panel and the measured incident solar radiation corresponding to the electrolysis experiment under silent conditions have been adopted in the numerical model in order to simulate the behaviour of the PV panel under the conditions of the experiment. The performance of the PV panel is first discussed based on the polarisation curve of the panel, controlled by an MPPT regulator. The current- voltage I-V and power-potential P-V curves obtained numerically are reported in Fig 3.3, the maximum power point and its equivalent current and potential are marked in red on the same Fig. 3.3. For a global incident radiation of 827 W/m^2, it can be observed that the short circuit current value is 1.49 A. The maximum delivered power equals 19.48 W, which corresponds to a voltage of 14.7 V and a current of 1.33 A. The use of the MPPT solar regulator enables to sustain the input current at a constant value during the electrolysis to avoid the effect of intermittency of PV outputs.

The mathematical modelling and instantaneous simulation of the PV power supply and the electrolyzer operation allowed the determination of the overpotentials and resistances governing the performance of the electrolyzer. Under a direct current of 1.325 A supplied by the PV panel under 827 W/m^2, a mass flow rate of hydrogen of 13.8 µg/s is expected, considering 100% of faraday efficiency, according to the previous experimental result. The values obtained from the simulation are shown in Table 3-2. The reversible activation voltage for the studied electrochemical system under the considered thermodynamic conditions equals 1.23 V, while the activation and concentration overpotentials equal 0.295 V and 0.739 mV. Obviously, the ohmic resistance is the key player on the response of the electrolyzer. Due to the geometry of the H-cell, and the existence of a physical separation limiting the contact between the two compartments, a resistance value of 2.5 Ω was measured due to the cell itself. Other than the "physical" cell resistance, the electrodes and the electrolyte contribute to the ohmic resistance. Table 3-2 shows that the contribution of the cathode and

anode in the overall resistance of the cell, and specifically the Ohmic resistance is negligible, with a value 9.07 nΩ. This is due to the high conductivity of the nickel material used in the electrodes. The electrolyte resistance is due to the electrolyte solution nature and concentration, the temperature, and the formed bubbles covering the electrodes surfaces and lowering the area of the active sites. The simulation results indicate that the bubble-free electrolyte resistance under the experimental conditions equals 250.36 mΩ, while the resistance due to the formed bubbles depends of the percentage of electrodes coverage. The resulting ohmic overpotential and then the electrolyzer potential are both dependent of the electrodes coverage percentage, it is suggested to inspect their variations in function of the *e* percentage, as shown in Fig.24(a).

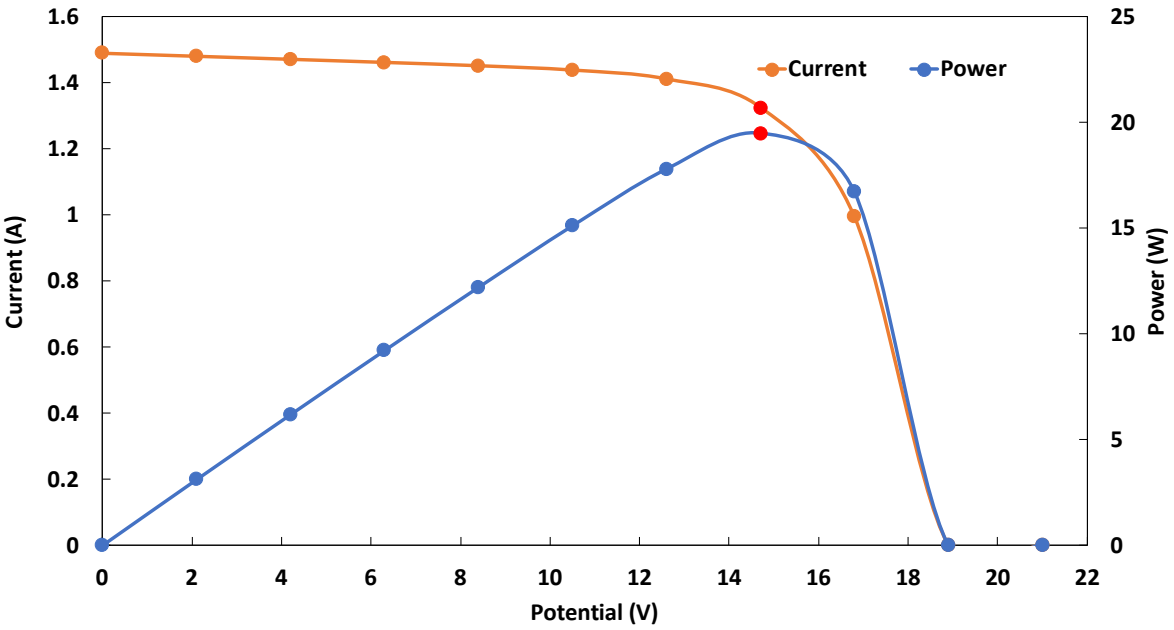

Figure 3.3 *Simulated I-V and P-V characteristics of the solar panel feeding the electrolyzer under real solar radiation (827 W/m^2).*

Table 3-2 *Results of the electrolysis parameters from simulation*

Symbol	Description	Values
I_{max}	Maximum current (A)	1.325
$\dot{m}_{H_2}$	Hydrogen production (µg/s)	13.8
E_{rev}	Reversible voltage (V)	1.2342
U_{Conc}	Concentration voltage (mV)	0.739
U_{act}	Activation voltage (V)	0.295
R_{cell}	Cell resistance (Ω)	2.5
R_{bf}	Free-bubble resistance (mΩ)	250.36
R_a	Anodic resistance (nΩ)	9,065
R_c	Cathodic resistance (nΩ)	9,065
$R_{electrical}$	Electrical resistance (mΩ)	21.04

Fig 3.4 (a) demonstrates that the studied electrolysis cell develops an overall potential ranging from 5.24 to 6.60 V (equivalent to an increase of 25.88%) when the electrodes coverage percentage varies between 0 and 100%. The ohmic overpotential increases, with the aforementioned variation of the *e* factor, from 3.67 to 5.07 V, which constitutes 68.93% to 76.81% of the overall potential value. In order to meet the experimental conditions, the measured cell potential of 5.96 V is identified in the simulated evolution, it is highlighted in red in Fig 3.4 (a). a corresponding electrodes' coverage percentage of 81.98% is then retrieved. Accordingly, the Ohmic overpotential characterizing the studied configuration equals 4.43V.

As assumed in the literature [38], the attachment of the bubbles to the electrode surface creates a resistance that occurs between the metal surface and the bubbles that is called the bubble resistance. The expression of ohmic resistance is a sum of the resistance that occurs in the electrolyte as well as in the entire cell configuration, including the bubble resistance [21]. Thus, the electrodes' coverage percentage controls the ohmic overpotential through the bubble resistance. In Fig 3.4 (b), we propose to visualize the evolution of the ohmic and bubble resistances as a function of the *e* factor. Visibly, when a bubble-free electrolyte is assumed, the bubble resistance is null and the ohmic resistance is at its lowest value of 2.77 Ω. At the opposite, if the

bubbles cover "hypothetically" the whole electrodes' surface, the bubble resistance reaches 1.05 Ω, constituting 27.49% of the Ohmic resistance and increasing its value to 3.82 Ω. If excluding the resistance due to the physical separation related to the geometry of the H-cell, the bubble resistance would constitute 79.46% of the developed ohmic resistance. The literature reports that the proportion of bubble resistance to ohmic resistance is particularly noticeable when bubble coverage is high. For instance, bubble resistance represents more than 60% of the total ohmic resistance for a complete bubble coverage [21], which is in good agreement with the retrieved result. It is also reported that the bubble resistance proportion decreases to only 3.8% for a 10% of bubble coverage [21].

Energetically speaking, the energy efficiency of the electrolysis system is directly related to the bubble resistance, as the increase of the overpotential induces an increase in the consumed power without any compensation in terms of hydrogen flow rate in the case of a current power supply. Thus, with a PV supplied electrolysis, the decrease of the electrodes' coverage percentage results directly in an improvement in the energetic response of the system. Fig 3.4 (c) reports the values of the consumed power, which are directly proportional to the values of the overall voltage presented in Fig 3.4 (a). The consumed power corresponding to the 7.89 W, which is equivalent to 40% of the maximum deliverable power by the PV panel in the studied conditions.

It is believed that the integration of the ultrasonic action reduces the percentage of the electrode surface covered by bubbles through the physical actions of sonication. This will be investigated numerically in the following section, in the particular case of a current source power supply, namely the PV panel.

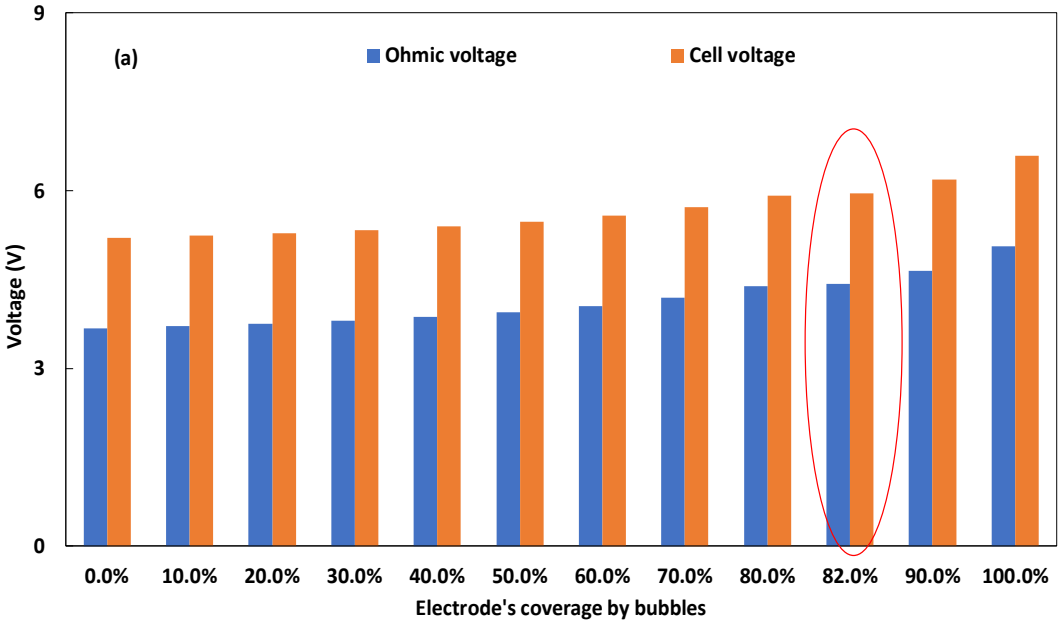
(a)
Ohmic voltage
Cell voltage
Voltage (V)
9
6
3
0
0.0%
10.0%
20.0%
30.0%
40.0%
50.0%
60.0%
70.0%
80.0%
82.0%
90.0%
100.0%
Electrode's coverage by bubbles

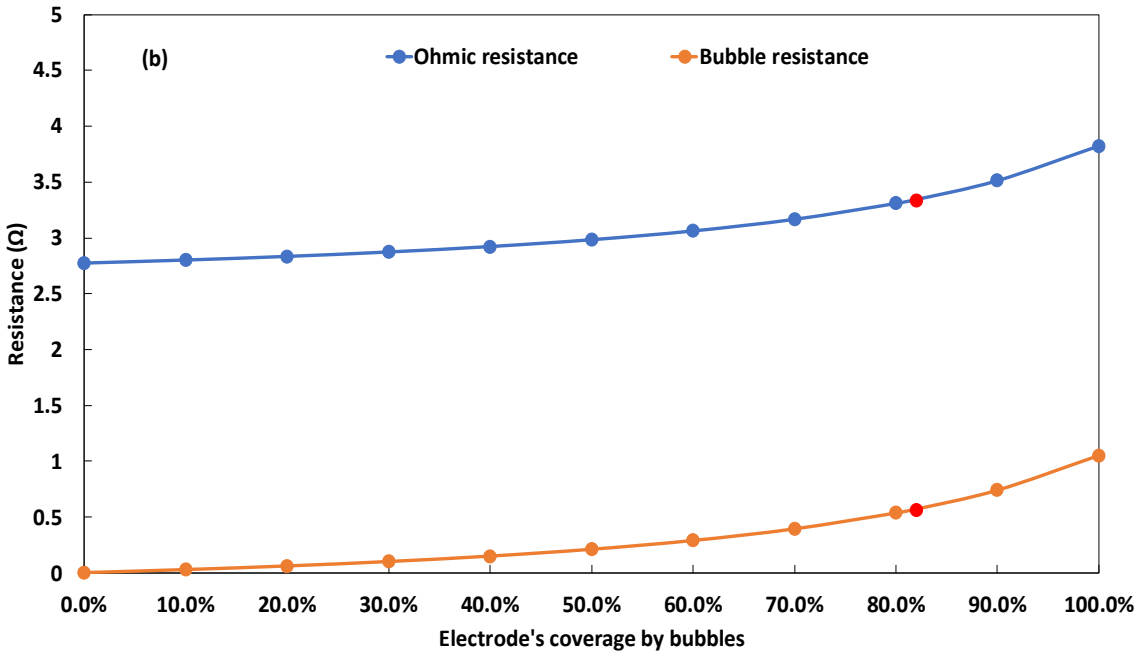
(b)
Ohmic resistance
Bubble resistance
Resistance (Ω)
5
4.5
4
3.5
3
2.5
2
1.5
1
0.5
0
0.0%
10.0%
20.0%
30.0%
40.0%
50.0%
60.0%
70.0%
80.0%
90.0%
100.0%
Electrode's coverage by bubbles

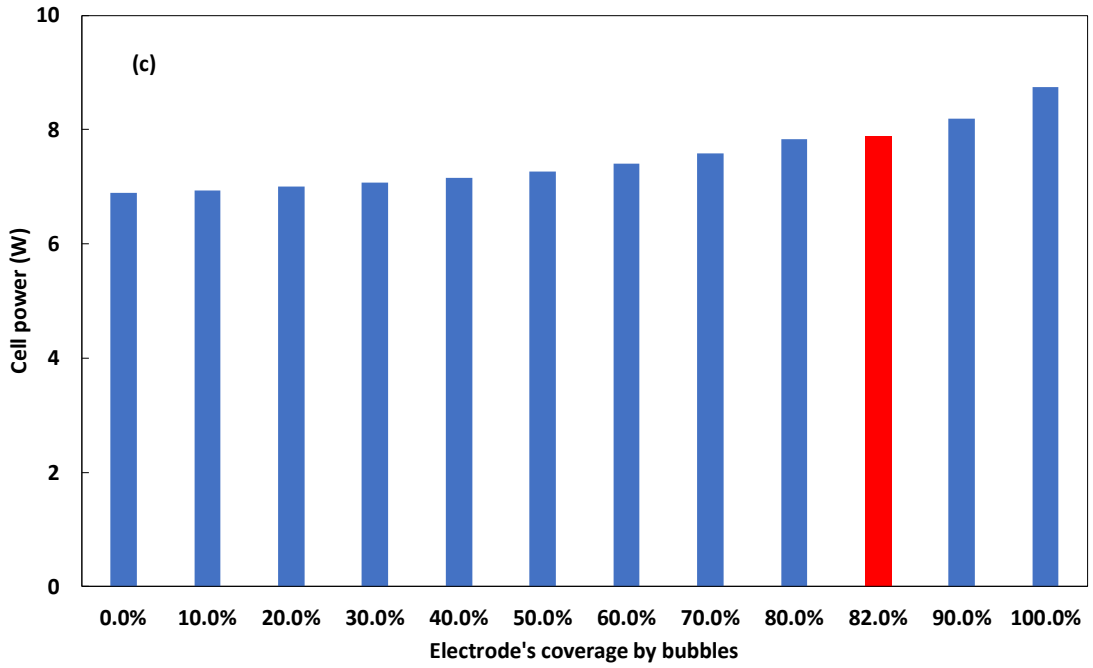

Figure 3.4 *Effect of the electrodes' coverage by bubbles on the ohmic and cell voltage (a), ohmic and bubble resistances (b), and cell power (c) in the electrolysis.*

b) Continuous sono-electrolysis

The continuous sono-electrolysis experiments have been performed under a solar radiation of 938.5 W/m^2 that resulted in a slightly higher experimental cell current, and an identical cell potential as that retrieved experimentally with the silent configuration under a lower incident radiation. In Fig 3.5, we report the I-V and P-V curves of the ET-M53640 panel under a solar radiation of 938.5 W/m^2. The highest power equals 22.39 W and is achieved at a panel current of 1.523 A and a deliverable potential of 14.7 V. Thus, with the MPPT regulation, the electrolyzer is supplied with a direct current of 1.523 A, the simulation of the operation of the continuous sono-electrolyzer is performed under this current for an electrodes' coverage percentage varying between 0 and 1. The univariable parameters are reported in Table 3-3, while the variations of the cell and ohmic voltages, the ohmic and bubble resistances and the cell power in function of the *e* factor are shown in Fig 3.5.

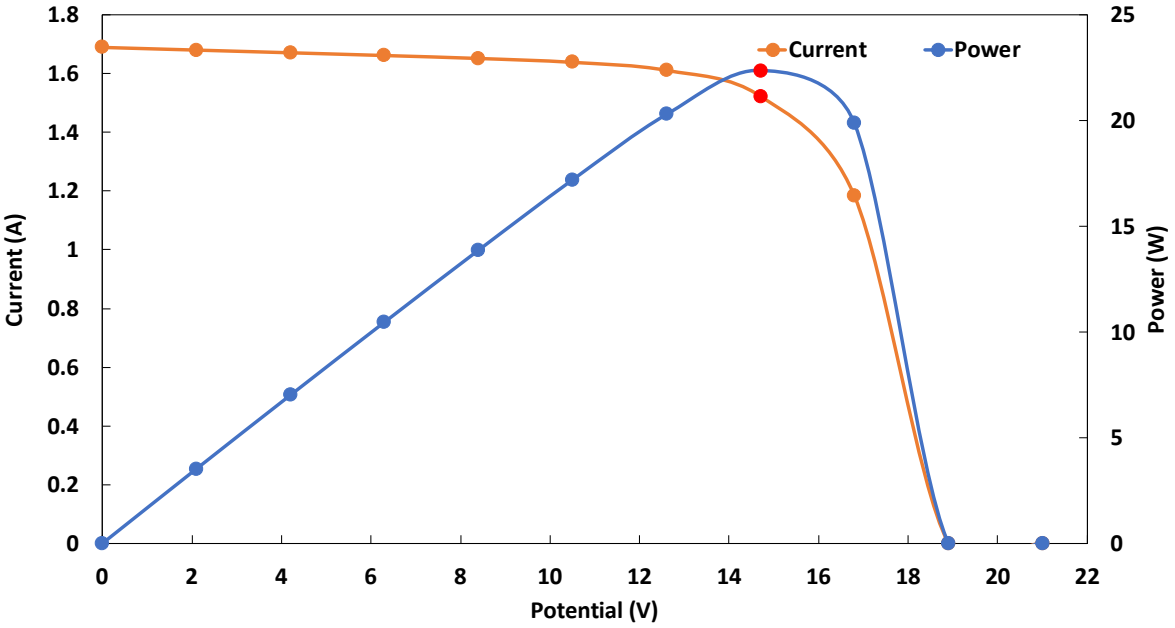

Figure 3.5 *Simulated I-V characteristics of the solar panel feeding the continuous sono-electrolyzer under real solar radiation (938.5 W/m2).*

The simulation shows that the experimental conditions induce a flow rate of hydrogen that equals 15.9 µg/s. The resulting activation and concentration overpotentials are slightly higher than those retrieved earlier under the conditions of the silent electrolysis. The activation overpotential equals 299 mV, while the concentration voltage has a value of 0.853 mV. Clearly, the concentration overpotential remains negligible, which is explained by the relatively low current density (56 mA/cm^2). The electrodes resistances, the resistance of the cell due to the physical separation of the anodic and cathodic compartments, the electrical resistance of the wires as well as the bubble-free electrolyte resistance remain identical to those presented earlier with the simulation under silent conditions. The total cell potential is then governed by the bubble resistance, which in turn depends on the coverage percentage of the electrodes.

Table 3-3 *Results of the continuous sono-electrolysis parameters from simulation*

Symbol	Description	Values
I_{max}	Maximum current (A)	1.523
$\dot{m}_{H_2}$	Hydrogen production (µg/s)	15.9
E_{rev}	Reversible voltage (V)	1.2342
U_{conc}	Concentration voltage (mV)	0.853
U_{act}	Activation voltage (V)	0.299

R_{cell}	Cell resistance (Ω)	2.5
R_{bf}	Free-bubble resistance (mΩ)	250.36
R_a	Anodic resistance (nΩ)	9,07
R_c	Cathodic resistance (nΩ)	9,07
$R_{electrical}$	Electrical resistance (mΩ)	21

Fig 3.6 (a) presents the evolutions of the overall cell voltage as well as the ohmic overpotential in function of the electrodes' coverage percentage under the continuous ultrasound conditions. The cell potential increases from 5.76 V to 7.36 V when the e factor passes from 0 to 1. The ohmic overpotential constitutes the major part of the cell potential, with a proportion ranging between 73.34% and 79.14%. The cell potential measured experimentally under the continuous sonication conditions is met at an electrodes' coverage percentage comprised between 30% and 40%. The simulation with a straightened step on the value of e allowed the determination of the electrodes' coverage percentage corresponding to the measured cell potential, namely 5.96 V. This value equals 37%, its related ohmic overpotential is 4.42 V, equivalent to 2.90 Ω as reported in Fig 3.6 (b). When excluding the overpotential due to the resistance of the cell due to its geometry (physical separation of the anodic and cathodic compartments), the bubble resistance is limited to 132.54 mΩ in this case as shown in the same Fig 3.6 (b), while it would attain 1.05 Ω when the electrodes' coverage increases to 100%. The integration of continuous sonication has visibly freed a considerable surface of the electrodes, offering larger active area and lowering the Ohmic resistance and the power consumption. The consumed power of the cell is reported in Fig 3.6 (c) in function of the electrodes' coverage percentage, it equals 9.07 W for a value of 37%, while it would exceed 10.01W for the coverage percentage of 82% retrieved earlier under silent conditions. The consumed power is then reduced by 9.33%. These results are in agreement with the explanation presented by Cataldo [15], where it was assumed that ultrasound induces a stirring effect in the bulk electrolyte and near the electrode surface which promotes the desorption of gas bubbles from the electrodes. Additionally, it was assumed that the reduction in overvoltage is related to

both microjets and microstreaming effects which contribute in the electrode cleaning due to the high velocity of these microjets [114].

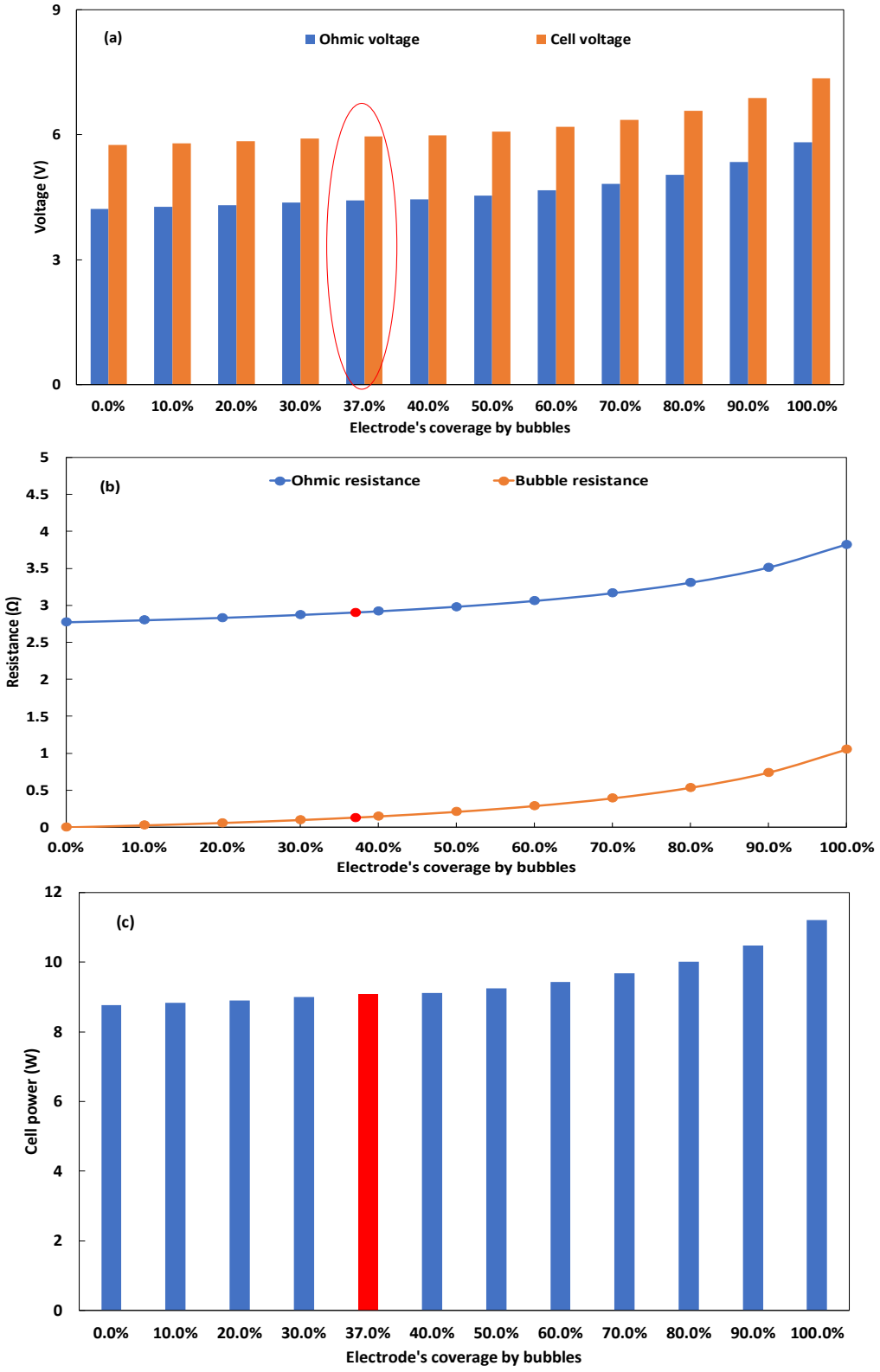

Figure 3.6 *Effect of the electrodes' coverage by bubbles on the ohmic and cell voltage (a), ohmic and bubble resistances (b), and cell power (c) in the continuous sono-electrolysis.*

c) Pulsed sono-electrolysis

The pulsed sono-electrolysis experiments were performed under an incident solar radiation of 899 W/m^2, this condition led to an experimental cell voltage of 5.96 V, which is identical to the values retrieved with previous experiments performed under silent and continuous ultrasound conditions. The performance of the PV supplying the pulsed sono-electrolysis cell is studied through the polarization curve represented in Fig 3.7.

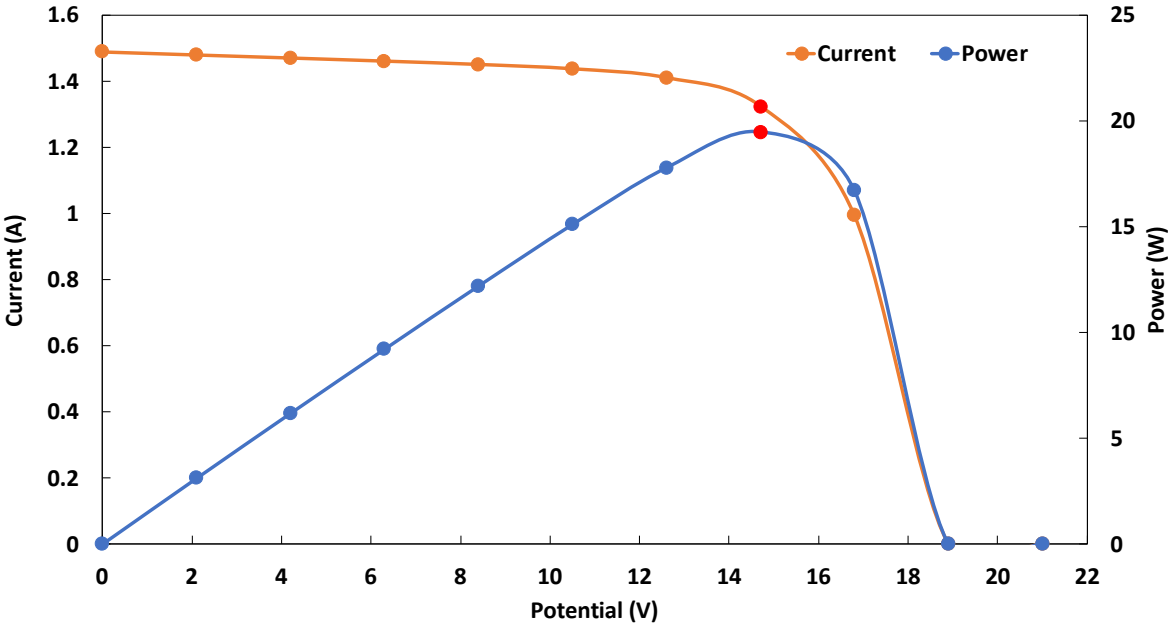

Figure 3.7 *Simulated I-V characteristics of the solar panel feeding the pulsed sono-electrolyzer under real solar radiation (899 W/m2).*

Fig 3.7 demonstrates that the maximum power point equals 19.48 W, and is achieved at a current of 1.453 A, which corresponds to a deliverable voltage of 14.7 V. The direct current feeding the electrolysis cell is slightly lower than the value corresponding to the continuous sono-electrolysis configuration (4.6% lower), and 9.7% higher than the current recorded under silent condition configuration. This direct current feeds the electrolysis cell in the presence of indirect pulsed sonication as described earlier. The simulation of the performance of the sonoelectrolyzer returns the parameters reported in Table 3-4.

The hydrogen production rate retrieved in this case equals 15.165 µg/s, while the activation and concentration overpotentials are estimated at 298 and 0.812 mV,

respectively. The monitoring of the evolution of the bubble resistance, which depends on the electrodes' coverage percentage, would indicate the value of the *e* factor characterizing the pulsed sono-electrolysis configuration, and hence the cell ohmic resistance. The corresponding value will be identified through the measured cell voltage, estimated at 5.96 V.

Table 3-4 *Results of the pulsed sono-electrolysis parameters from simulation*

Symbol	Description	Values
I_{max}	Maximum current (A)	1.453
$\dot{m}_{H_2}$	Hydrogen production (µg/s)	15.165
E_{rev}	Reversible voltage (V)	1.2342
U_{conc}	Concentration voltage (mV)	0.812
U_{act}	Activation voltage (mV)	298
R_{cell}	Cell resistance (Ω)	2.5
R_{bf}	Free-bubble resistance (mΩ)	250.36
R_a	Anodic resistance (nΩ)	9,07
R_c	Cathodic resistance (nΩ)	9,07
$R_{electrical}$	Electrical resistance (mΩ)	21

Fig 3.8 (a) reports the evolution of the cell and ohmic voltages as a function of the electrodes' coverage percentage. The cell voltage value of 5.96 V is met at an *e* factor of 58.3%. In this case, the cell shows an Ohmic resistance of 4.424 Ω.

Fig 3.8 (b) presents the variation of the bubble resistance as a function of the *e* factor. For the previously retrieved electrodes' coverage percentage of 58.3%, the bubble resistance equals 273.42 mΩ, which is equivalent to 1.09-fold the bubble free electrolyte resistance. In terms of power consumption, the operating conditions of the cell under pulsed sonication leads to a cell power value of 8.66 W, as shown in Fig 3.8 (c). this value is 7.14% higher than what would be theoretically retrieved in the absence of bubbles covering the electrodes surface. Besides, when considering the electrodes' coverage percentage retrieved earlier both under silent and continuous sonication conditions, which equal 82% and 37%, respectively. The bubble resistance would be

equivalent to 575 and 132 mΩ, while the cell power would equal 9.29 and 8.35 W, respectively, for a similar supply current value.

To sum up, the key parameters characterizing the three studied configurations, as per the performed simulations, are reported in Table 3-5.

Table 3-5 *Key parameters characterizing the operation of the electrolyzer under silent, indirect continuous sonication and indirect pulsed sonication conditions*

Symbol	Silent	Continuous US	Pulsed US
$\boldsymbol{U_{cell}}$ **(V)**	5.96	5.96	5.96
$\boldsymbol{I_{max}}$**(A)**	1.325	1.523	1.453
$\boldsymbol{R_b}$**(mΩ)**	569.51	132.54	273.42
$\boldsymbol{e}$	82%	37%	58.3%

Table 3-5 indicates that for a similar cell voltage, the highest cell current corresponds to the continuous sono-electrolysis configuration, leading to a higher rate of produced hydrogen. The higher current value is associated to a lower bubble resistance and a reduced electrodes' coverage percentage. In the presence of indirect continuous sonication, the bubble resistance becomes 76% lower than in the absence of sonication and 52% lower than under pulsed sonication. Hence, the integration of continuous sonication is proved to be the most efficient mode for bubble removal through acoustic cavitation action, this would be particularly interesting and significant in membraneless/ membrane electrolyzers with no physical separation related to the geometry of the cell

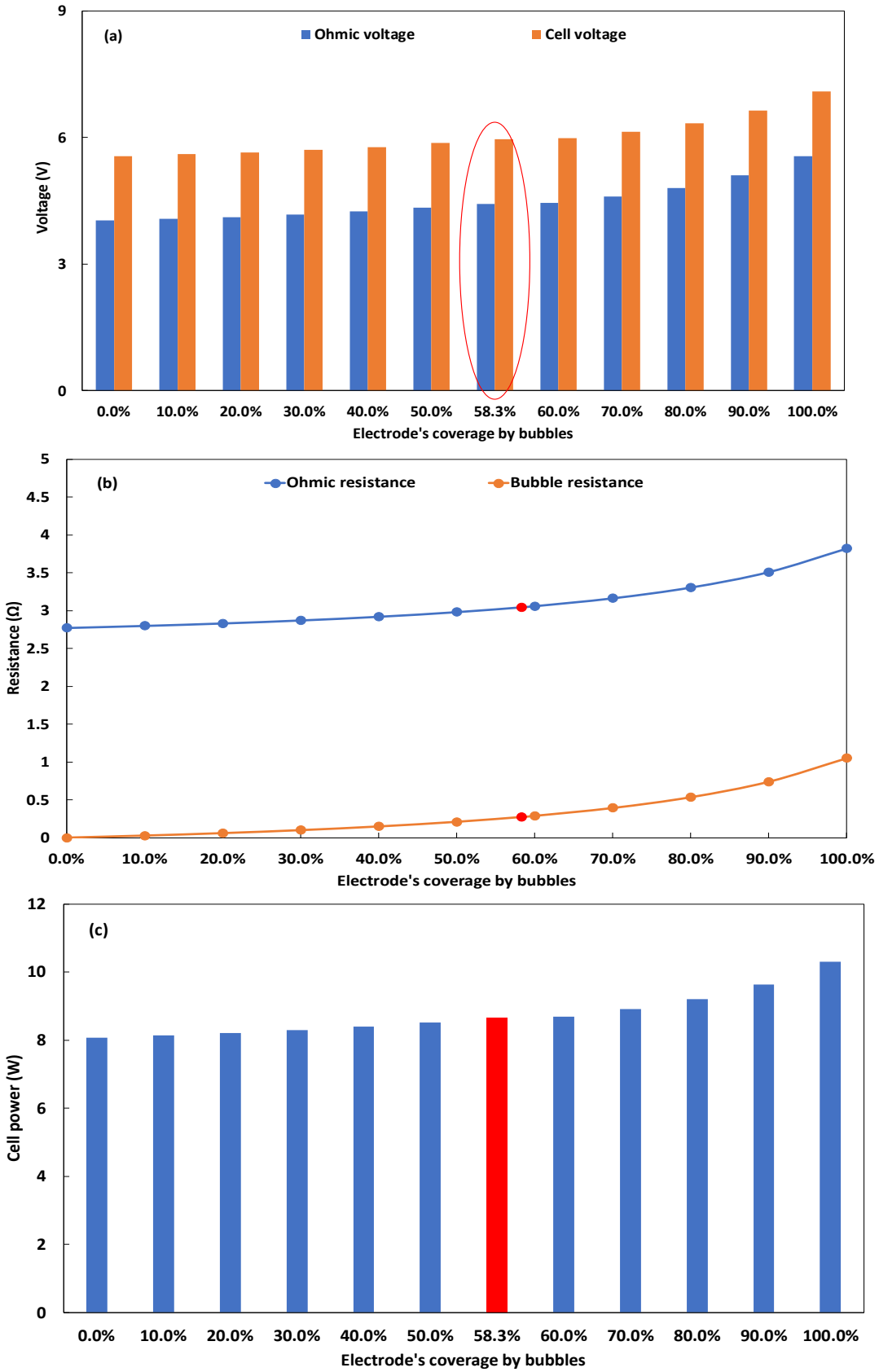

Figure 3.8 *Effect of the electrodes' coverage by bubbles on the ohmic and cell voltage (a), ohmic and bubble resistances (b), and cell power (c) in the pulsed sono-electrolysis.*

3.4.2 Dynamic conditions

3.4.2.1 Numerical comprehension of the sono-electrolysis performance

a) Silent conditions

Fig 3.9 (a) shows the simulated hourly solar irradiance and delivered current f for each month. It is clear that the solar radiation and the delivered current are at their highest values during the summer period. The highest values of solar radiation 992 W/m^2 are reached in the summer period during the month of May around solar noon, while the maximum delivered current of 1.6 A was recorded during the month of June. The kinetic of hydrogen production according to the hourly delivered current is shown in Fig 3.9 (b). The kinetic of hydrogen production increases with increasing current according to Faraday's law and reaches its maximum of 8 µmol/s in June around solar noon.

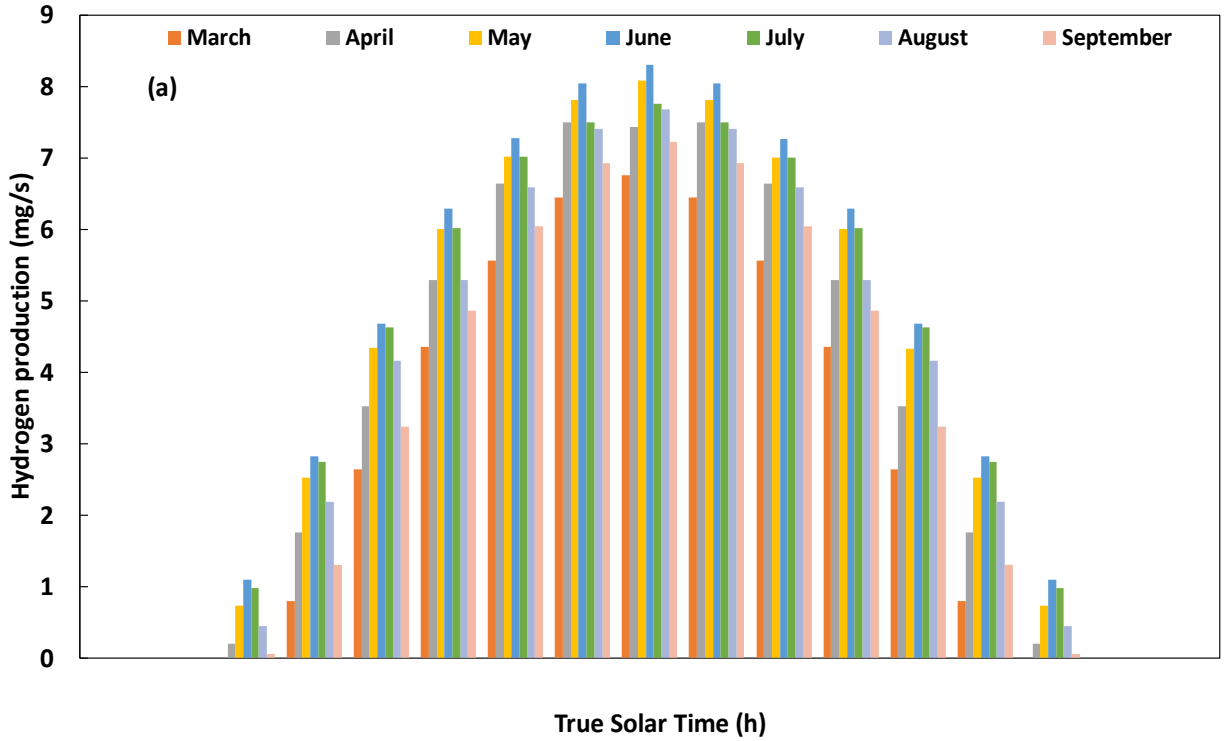

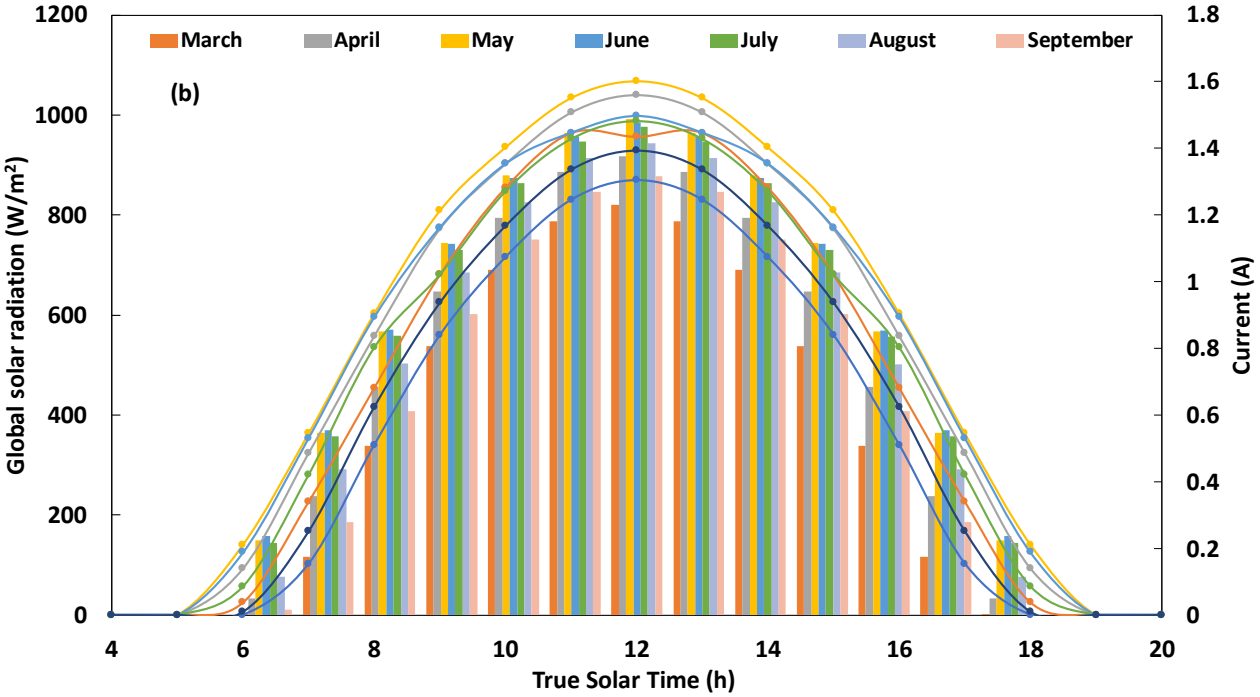

Figure 3.9 *Simulated results of monthly hourly solar radiation and delivered current (a) and kinetics of hydrogen production and delivered current (b).*

b) Acoustic conditions

According to the obtained results and based on the calorimetric study [93], the characterization of the sonication system demonstrated an acoustic efficiency of 13.7% when considering the delivered power of 60W. This means that the remainder of the power consumed is dissipated as heat to the electrolyte and the surrounding environment.

Fig 3.10 (a) and (b) shows the average cell resistance and cell voltage as a function of the coverage of the electrode with air bubbles simulated under a continuous sonication. The electrode bubble coverage in the presence and absence of ultrasound is 37% and 82%, respectively, based on the previous experimental results[94]. Thus, it can be seen that in the quiescent system, the ohmic voltage and the cell voltage range from 2.6 to 3.5V and from 4.1 to 4.8V, respectively, depending on the month, whereas under sonication they decrease to 2.25 to 2.8V for the ohmic voltage and to 3.7 to 4.3V for the cell voltage.

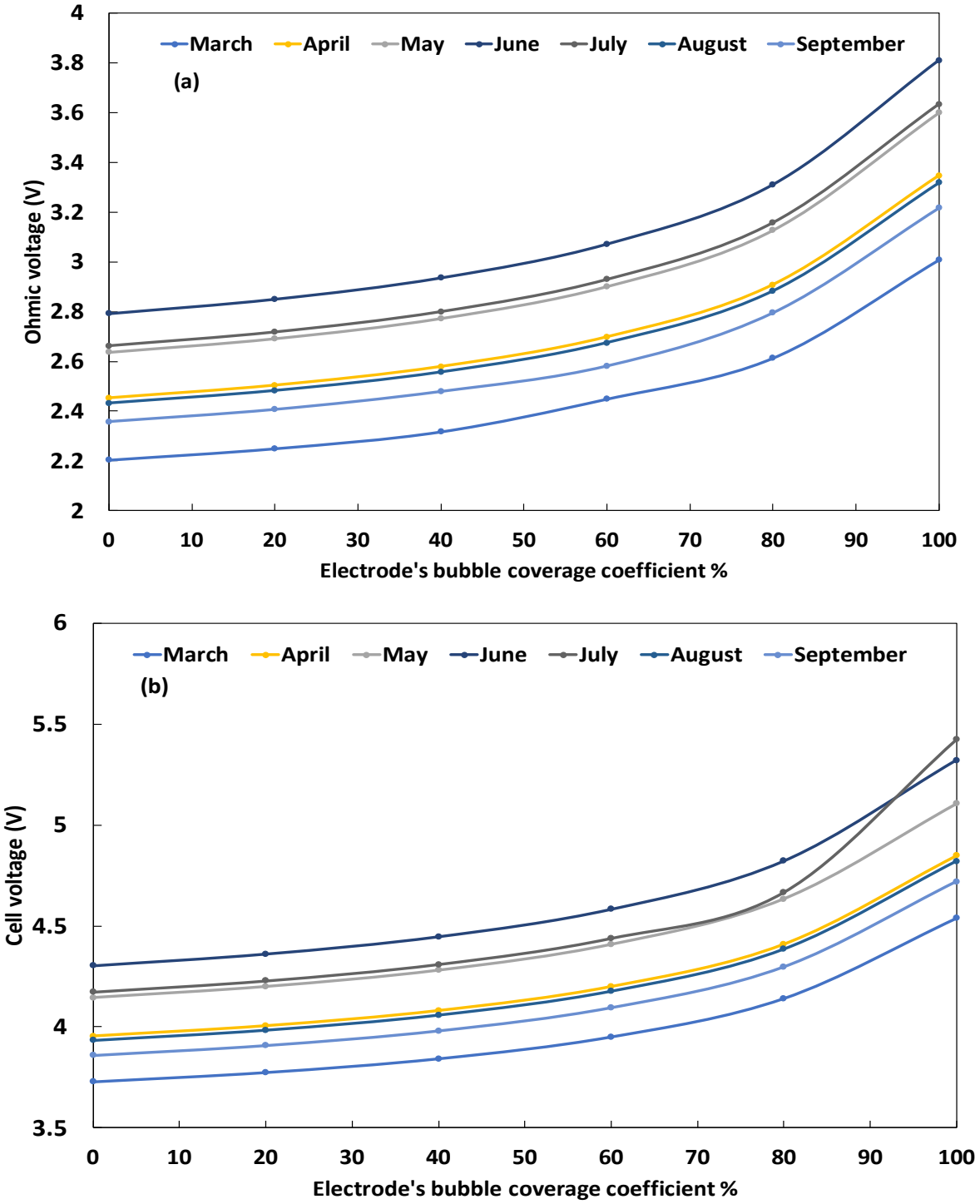

Figure 3.10 *Simulated results of monthly average (a) ohmic voltage; (b) cell voltage in function of electrode's bubble coverage.*

As it is assumed in the literature, the bubble presence in the electrolyte and on the electrodes' surface increases the ohmic resistance and voltage and thus the power consumption. It was observed that the higher the current supplied by the solar panel, the higher the hydrogen production kinetic and the higher the bubble and ohmic

resistance. The integration of the sonication reduces the ohmic voltage by about 13.5-20% and the cell voltage by 9.7-10.4%, depending on the month. This means that for the same feed current, the hydrogen kinetics described by the mass flow rate is more important due to the effective desorption effect of the sonication.

3.4.3 Modeling comprehension of the role of ultrasounds in PV-sono-electrolysis

After studying the effect of ultrasound on the bubble coverage of the electrodes, the second pathway to investigate is the effect of ultrasounds on mass transfer, specifically through the enhancement of the mass transfer coefficient which affects the limit current and hence the concentration overpotential as shown in Eq 1.19 and Eq 1.20, respectively. Fig 3.11 shows the simulated variation if the concentration overpotential as a function of the diffusion coefficient in the range 50×10^{-6} to 200×10^{-6} cm^2/s. Increasing the diffusion coefficient causes a decrease of the concentration overpotential, which is more pronounced at higher incident solar radiation. However, as the current density is low, the concentration overpotential remains limited to the order of mV [3]. Consequently, the effect of ultrasounds cannot be explained by the improvement of the mass transport properties alone, and even if such an effect exists, its extent is limited and can be neglected.

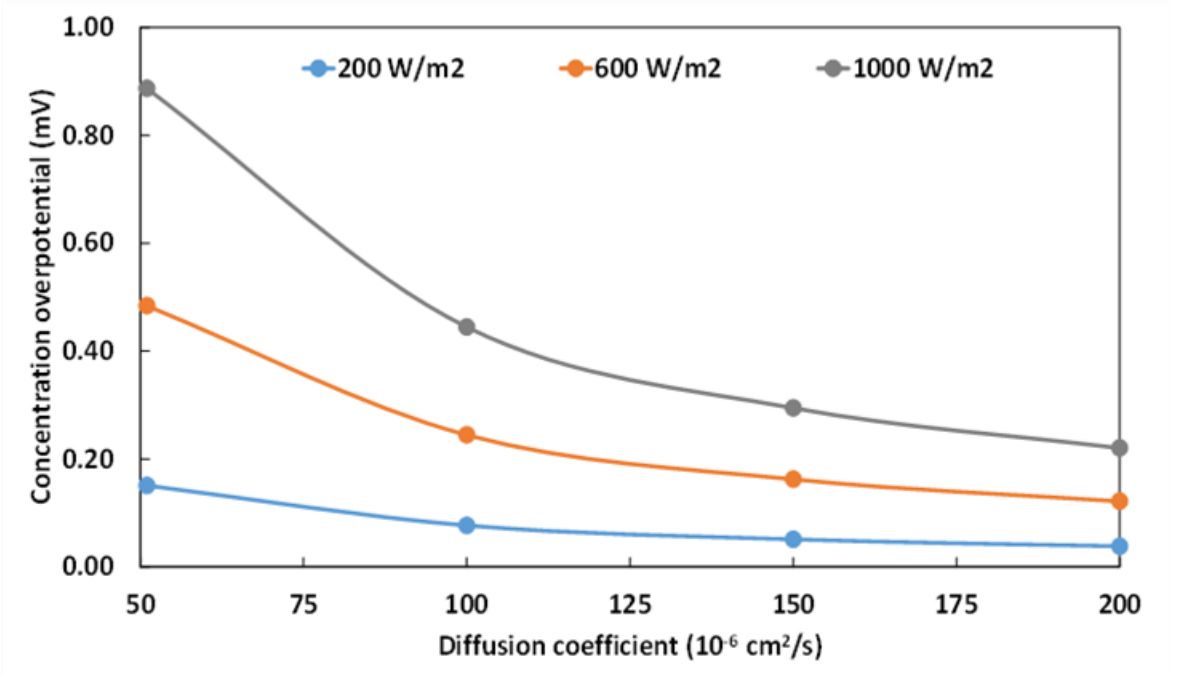

Figure 3.11 *Simulated effect of diffusion coefficient on the concentration overpotential*

The kinetics of hydrogen production is subject to Eq 1.21, where the Faraday efficiency describes how close is the behaviour of the sono-electrolytic cell is to the ideal performance governed by the Faraday equation. The literature agrees that the Faraday efficiency is lower than 1 when the current density becomes significant [115,116]. Fig 3.12 demonstrates that the mass flow rate of hydrogen is more affected by the value of Faraday's efficiency when the incident solar radiation is higher. For instance, it passes from 3.28 to 8.2 µg/s when Faraday's efficiency increases from 0.4 to 1. Nonetheless, the results in section 3.4.1.2 reveals that the measured value of mass flow rate of hydrogen is quasi-equal to the simulated ideal production, with a difference of 5.92% and an upper hand to the experimental value, probably explained by the presence of water vapor. Consequently, the Faraday efficiency equals 1. In the absence of ultrasounds, and according to our previous findings [94], a similar result is retrieved. Hence, the effect of ultrasounds cannot be attributed to a modification of Faraday efficiency.

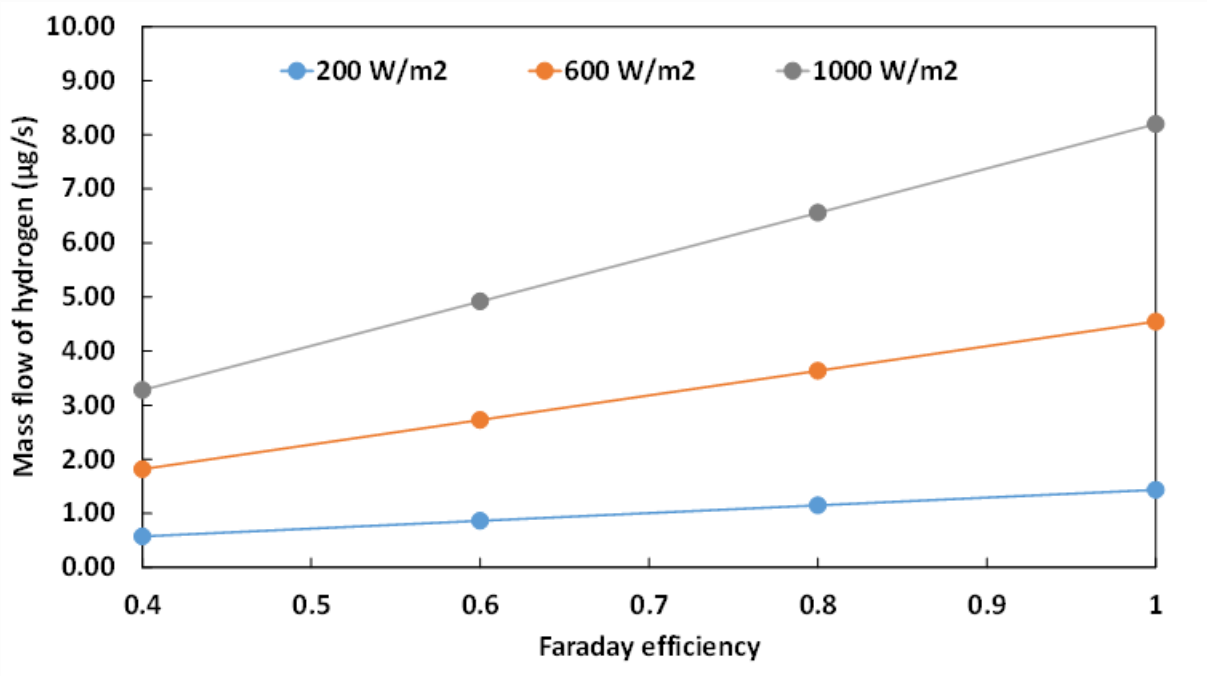

Figure 3.12 *Simulated effect of Faraday efficiency on the mass flow of hydrogen*

3.5 Conclusion

In the present chapter, the effect of sonication on the membraneless H-cell alkaline electrolyser supplied by PV has been studied experimentally and numerically under

static and dynamic conditions. The hybrid approach, combining experiments and fundamental modelling was based on a parametric study of the effect of sonication on the electrolyte resistance, the concentration overpotential and the mass flow rate of hydrogen produced.

The three configurations (silent, continuous sonication and pulsed sonication) have been studied under incident solar radiations leading to similar experimentally measured cell voltages of 5.957 ($\pm$0.1%).

The performance of the PV panel feeding the electrolyser has been simulated under each incident solar radiation (827, 938.5 and 899 W/m^2) through the polarization curve. The direct current resulting from the MPPT control was obtained numerically in each case, and the highest value corresponded to the continuous sono-electrolysis configuration, for similar cell voltages obtained experimentally.

The measured cell voltage value allowed the identification of the electrodes' coverage percentage matching with each configuration, and consequently the ohmic resistance parameters, including the bubble resistance. The indirect continuous sono-electrolysis demonstrated the lowest electrodes' coverage percentage with a value of 37%, against 82% under silent conditions and 58.3% under pulsed sonication. The resulting bubble resistance passed from 569.81 mΩ in the absence of ultrasounds, to 132.54 mΩ when integrating continuous sonication and 273.42 mΩ under pulsed sonication. Hence, in the presence of indirect continuous sonication, the bubble resistance becomes 76% lower than in the absence of sonication and 52% lower than under pulsed sonication.

Based on the effect of ultrasounds on the diffusion coefficient, the influence of ultrasounds cannot be entirely attributed to improvements in mass transport properties, and any such effect, if present, appears to be limited and negligible. Furthermore, according to our results, the effect of ultrasound cannot be attributed to a change in Faraday efficiency. This is because the experimental verification has shown that the Faraday efficiency remains consistently 1 regardless of the presence or absence of ultrasound. In addition, the comparison between measured and simulated hydrogen

mass flow rates showed a small difference of 5.92%, with the experimental values possibly influenced by the presence of water vapour. Hence, the integration of continuous sonication is proved to be the most efficient mode for bubble removal through acoustic cavitation action.

Finally, dynamic conditions showed that hydrogen production was highest in summer when radiation was maximum. In addition, maximum reductions of 13% and 10% in ohmic and cell voltages, respectively, were recorded under radiation conditions.

CHAPTER 4

"Green hydrogen production from wastewater: Integration of PV supply and sonication"

CHAPTER 4: GREEN HYDROGEN PRODUCTION FROM WASTEWATER: INTEGRATION OF PV SUPPLY AND SONICATION

4.1 Introduction

Currently, there are several technologies for hydrogen production using solar energy based on the direct splitting of water exist, while concentrated solar power, direct solar desalination, or photocatalysis remain less advanced [117,118]. Green hydrogen from water electrolysis is considered to be the most mature technique [118].

Basically, generation of hydrogen from water electrolysis is based on the following Eq 4. 1.

$$H_2O + Electricity\ (232.2\ kJ/mol) = H_2 + \frac{1}{2}O_2 + Heat\ (48.6\ kJ/mol) \quad (4.1)$$

The efficiency of the electrolyzer is a crucial parameter in hydrogen production system, as the overall cost of the process is closely related to the desired efficiency [59]. Alkaline water electrolysis, which is the earliest, the simplest and the most mature technology, has an efficiency in the range of 50-70% that makes it the most traded water electrolysis method in the market [119]. However, the production of 1 kg of hydrogen through water electrolysis technique needs approximately 9 kg of fresh water [120].

Meanwhile, the increasing amount of wastewater disposal is a reason of huge concerns regarding the environmental pollution in numerous sectors [7]. Currently, almost 1000 km^3 of wastewater is produced worldwide each year, including more than 300 km^3 of municipal wastewater and more than 600 km^3 of industrial wastewater [121], while an increase by 24% in wastewater generation is expected in the next 7 years worldwide (2030) and 51% by 2050, compared to the current rate [122]. In a time of the crisis of scarcity in fresh water, wastewater is seen as a promising feedstock for hydrogen and production. According to researchers assumptions, wastewater contains an energy varying from 17.8 to 28.7 kJ/g COD equivalent to 3-4 folds the energy demand for water treatment [123]. For instance, more than 2300 tons of H_2 could theoretically be

produced daily in the UK, given the UK's wastewater production of approximately 11 billion L/day [124].

The waste-to-energy strategy addresses three major environmental issues, namely waste management, greenhouse gas emissions and energy production [125]. As alternatives for fresh water, the seas (seawater), estuaries, surface water (streams, rivers and lakes), groundwater, rainwater, water from the public grid, recycled water (treated municipal or industrial wastewater) or water condensation processes (e.g. cooling towers) are considered to be a potential sources for water electrolysis [120] and global bio-hydrogen generation. Therefore, the adoption of systems that simultaneously produces hydrogen while treating wastewater is important for the minimization of greenhouse gas emissions and the recovery of the energy consumed in wastewater treatment [126]. In addition, electrolytic hydrogen production and wastewater treatment technologies are usually regarded as energy-consuming techniques. Therefore, renewable and environmentally friendly energy sources are needed as an alternative to conventional energy sources, which are considered to be as a major source of pollution [127].

In this chapter, we investigate hydrogen production by sono-electrolysis of wastewater treated by a laboratory side-stream membrane bioreactor (SSMBR). The effect of water quality on the produced hydrogen is evaluated using a GC-TCD (gas chromatograph coupled to a thermal conductivity detector), and the effect of sonication on the energy efficiency and kinetics of hydrogen production is also assessed. Finally, the voltage source as a conventional electrical energy source, i.e., a conventional DC generator, was replaced by a current source consisting of a PV power supply, which acts as a green energy source for the production of green hydrogen from membrane bioreactor permeate.

4.2 Experimental procedure

4.2.1 Description of the MBR unit

A lab scale side-stream MBR consisting of a 24L aerobic reactor was used and fed with domestic wastewater with an average daily water consumption of 2.4 L. The MBR unit

was operated at a hydraulic retention rate of 10 days, with a Mixed Liquor Suspended Solids (MLSS) concentration in the reactor of 5 g/L. The average flow in the MBR unit remained around 24 L/h at a transmembrane pressure in the average of 0.1-0.35 bar. In the fermenter, wastewater undergoes aerobic biological degradation, which is ensured by an aeration system installed at the bottom of the aerobic reactor. The fermenter is equipped with a DO (dissolved oxygen) sensor in order to maintain the DO level in the range of 2-3 mg/L, pH sensor to maintain the pH in the range of 5.5-6.7 and a conductivity meter. The fermenter and the membrane module are connected through a circulating siemens IEC/EN 60034 pump as shown in Fig 4.1.

The membrane separation step is provided by a polyethersulfone (PES) ultrafiltration flat sheet membrane with a permeability exceeding 285 L/h m^{-2} bar^{-1} and a total membrane surface area of 23.2×5.8 cm^2. It has a nominal molecular weight cut-off (M.W.C.O.) of 150000 Daltons.

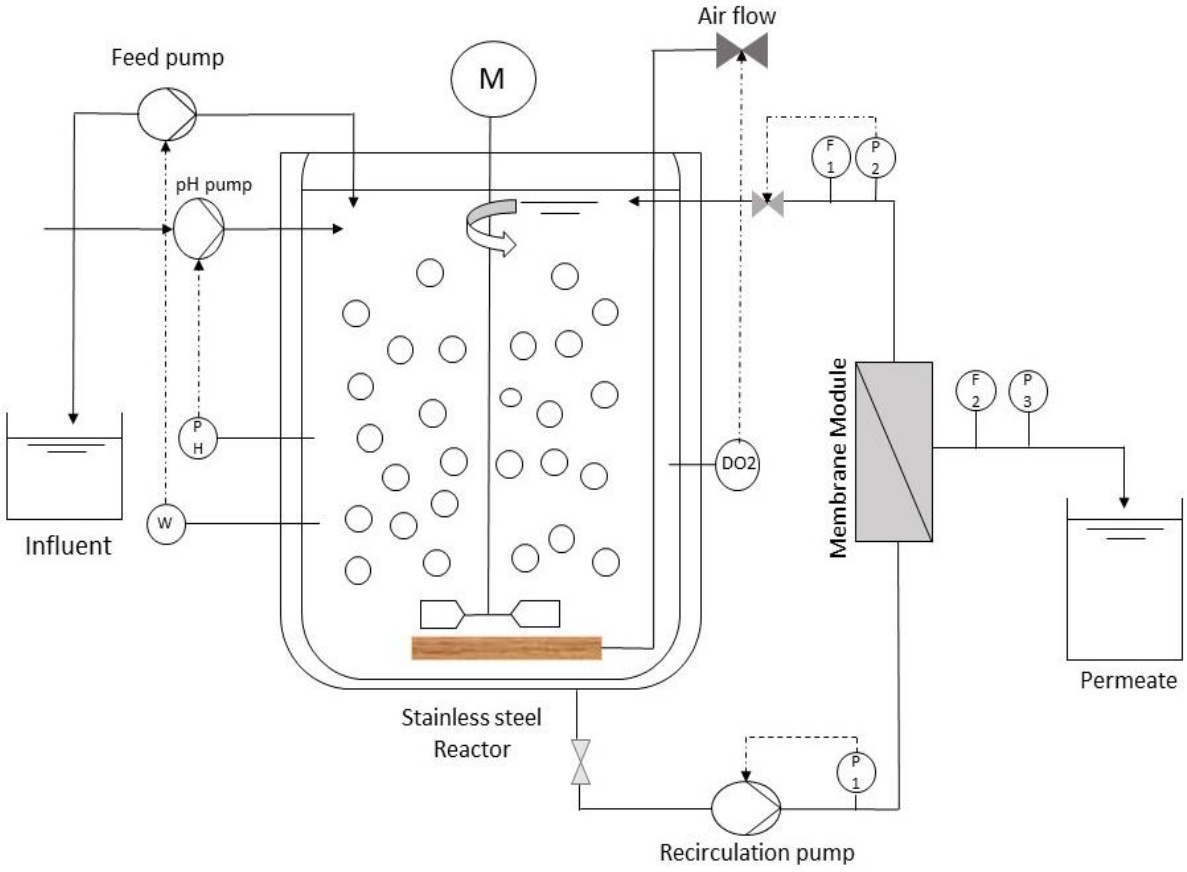

Figure 4.1 *Schematic of the experimental side-stream MBR setup*

4.2.2 Synthesis and characterization of model wastewater

Model domestic wastewater was prepared to mimic the original characteristics of real domestic wastewater, namely its conductivity, pH, nitrogen content, phosphor content, carbon content etc., in order to be used for treatment in MBR. The synthetic domestic wastewater composition in distilled wastewater is as follow: 640 g/L of $C_6H_{12}O_6$, 147 g/L of $CaCl_2$, 220g/L of $NaHCO_3$, 80g/L of $(NH_2)_2CO$, 98g/L of NH_4Cl, and 96g/L of $Na_3PO_4.12H_2O$. The characteristics of the synthesized wastewater and the adopted analysis methods are shown in Table 4-1.

Table 4-1 *Characteristics of synthesized domestic wastewater*

Parameters	Method/Device	Standard deviation of the method	Measured value in synthesized wastewtaer
pH	WTW pH 325	± 0.1	5.7
Electrical conductivity	WTW Cond 315i	± 10	1057 µS/cm
COD	Merck Cell Test,114541	± 4.7	689.8 mg/L
TC	Shimadzu TOC-L	± 1.15	241.7 mg/L
TOC	Shimadzu TOC-L	± 0.17	190.5 mg/L
$N\text{-}NH_4^+$	Merck Cell Test, 114544	± 0.4	38.7 mg/L
NH_4^+		± 0.5	49.8 mg/L
$N\text{-}NO_3^-$	Merck Cell Test, 114542	/	/
NO_3^-		/	/
$P\text{-}PO_4^{3-}$	Merck Cell Test, 100474	± 0.024	8.4 mg/L
PO_4^{3-}		± 0.07	25.7 mg/L

4.2.3 Alkaline electrolysis and sono-electrolysis of treated wastewater

The same H-cell setup presented in section 1.2.1.1 (b) is used. The experiments are performed with a membraneless then a Zirfon membrane configuration, and nickel plate and nickel foam electrodes in treated water KOH solution. A Voltcraft DIGI40 DC power supply was used as the power source. Sonication was integrated indirectly using the same bath at 40 kHz and 60W_e.

4.2.4 PV supplied electrolysis and sono-electrolysis of treated wastewater

As in the previous section, the permeate from the MBR unit was injected into the electrolyser using nickel plate as electrode material, while the DC generator was replaced by a PV solar panel with a direct connection to the electrolyser as shown in Fig 4.2.

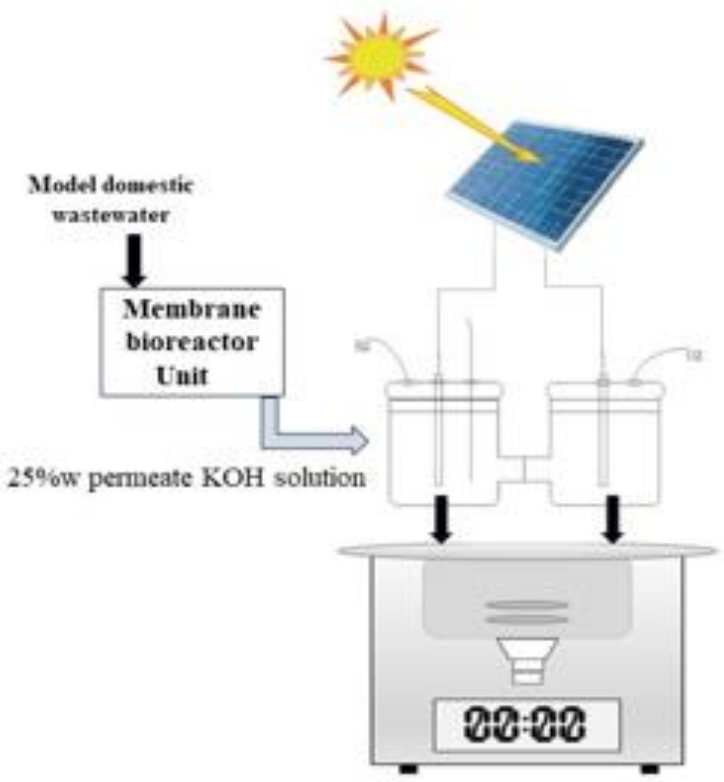

Figure 4.2 *Scheme of the solar hydrogen production process from wastewater*

4.2.5 Assessment of the purity of hydrogen

An Inficon micro-GC fusion gas analyzer with an integrated Thermal Conductivity Detector (TCD) was used to analyze the purity of produced hydrogen. The setup was directly connected to the gas inlet of the Gas chromatograph GC at an atmospheric pressure. Both Helium and Argon were used as carrier gases, the pressure in the column of the Argon was 35psi at a temperature of 100℃, which refers to 25psi and 60℃ for the Helium gas column.

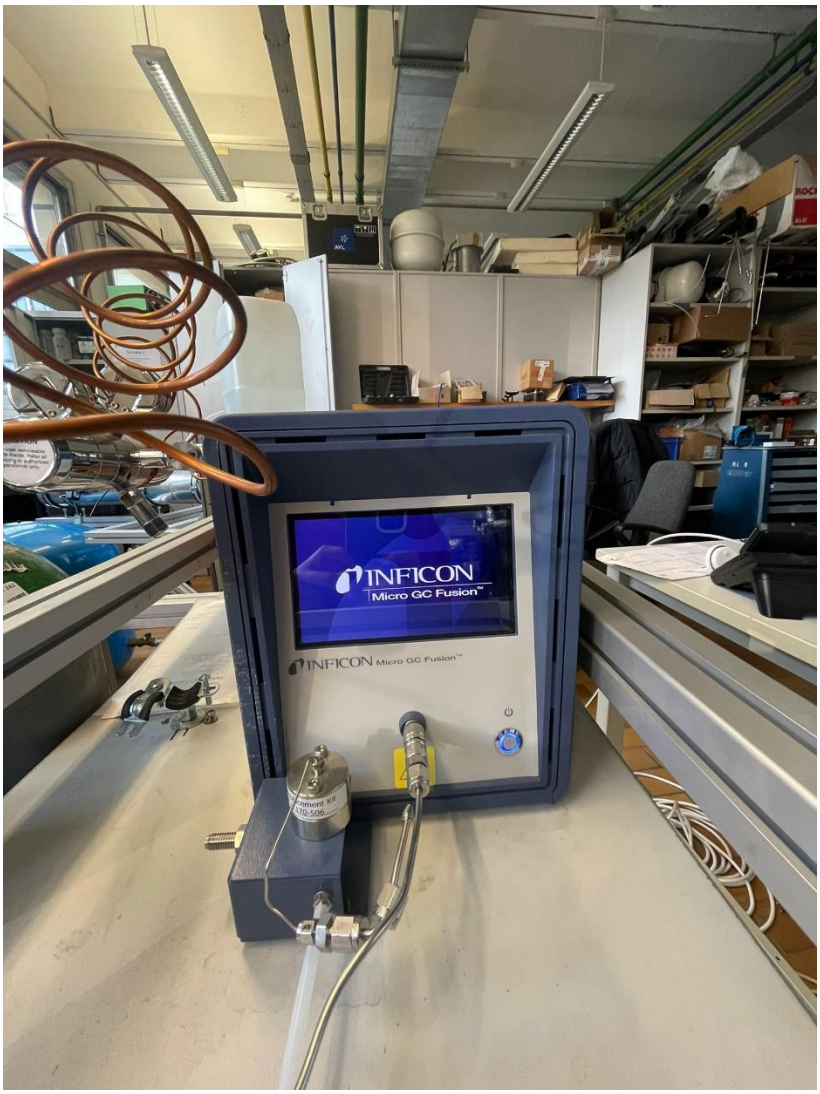

Figure 4.3 *Real image of Inficon GC for H_2 production gas analysis.*

4.3 Results and discussion

4.3.1 MBR permeate quality

In order to evaluate the efficiency of the MBR, the analysis of TOC, TC, IC and cell tests (COD, P-PO_4^{3-}, N-NH_4^+, N-NO_3^-) were performed for both the feed model wastewater and the permeate. The results of the permeate analysis are shown in Table 4-2.

One of the important parameters to ensure a high quality of effluent and smooth process operation is the MLSS that allows the measurement of the mass of suspended solids in the reactor tank during the activated sludge process. The MLSS was calculated by measuring the weight of the dried crucibles with sludge samples and dried crucibles with permeate samples at a temperature of 90°C for 24h.

The MLSS was set at 5 ±0.5 g/L. Although the MLSS concentration was relatively lower than the typical required concentration in an MBR system. According to the survey conducted, the MLSS should be in the range of 8.2-8.8 g/L [128]. However, in the current MBR system, MLSS concentrations higher than 5 g/L lead to rapid membrane clogging, resulting in poor MBR performance

4.3.1.1 Chemical Oxygen Demand (COD)

The Chemical Oxygen Demand (COD) is a key water quality parameter used to measure the amount of organic pollutants in water. The COD in the feed model water was in the average of 689.8 mg/L, which is within the typical range for domestic wastewater, as shown in Table 4-1. This value was reduced to 23-90 mg/L, resulting in an overall COD removal efficiency of up to 97%. The Hydraulic Retention Time (HRT) was set at 10 days throughout the process which is significantly longer than the typical HRT of 12 to 30 hours in AeMBRs [129]. This is due to the relatively small membrane area compared to the laboratory fermenter volume. The reported COD removal efficiency of the MBR is in good agreement with the literature [130].

4.3.1.2 Total Organic Carbon (TOC)

The TOC, like the COD is a measure of the amount of organic contaminants. The interest in TOC and TC removal is mostly related to the damage of the electrode and membrane material, the percentage of residual carbon can quickly degrade the electrodes and membrane material after a period of operation. As shown in Table 4-2, both TC and TOC ranged from 253 to 241.7 mg/L and from 190.5 to 225.3 mg/L respectively. In the permeate, the values were relatively constant and varied from 7.23-9 mg/L for TC and from 5.38-8.39 mg/L for TOC. TC removal of 96.7% and TOC removal of 97.2% were achieved.

In fact the quality of water for electrolysis is specified to be minimum at ASTM type II [131]. In this TOC particles concentrations must be lower than 50 µg/L. Therefore, the existence of high concentrations of TOC may affect the hydrogen purity.

4.3.1.3 Ammonium and nitrate

The presence of N in the form of ammonium and nitrate was detected in both feed and permeate, with a lower concentration in the permeate. The concentration of ammonium in the permeate was less than 0.5mg/L, a low concentration of nitrate was also recorded in the feed wastewater. This is clearly due to the nitrification of ammonia in the activated sludge tank, which is then converted to nitrate in the permeate. Therefore, an average nitrification rate of 63% was achieved in the system used (Table 4-2).

4.3.1.4 Phosphorus

Since the phosphate is not degraded by activated sludge. However, an accumulation of phosphate appears in the reactor tank, which is why phosphate was found at higher concentrations in the permeate ranging from 12 to 15.9 mg/L, compared to its concentration in the feed ranging from 7.7 to 8.4 mg/L. This could be due to the release of accumulated phosphate in the sludge. In fact, phosphate can be removed either by precipitation or by biological removal in an MBR system by exposing the bacteria to alternating anaerobic and aerobic conditions. Therefore, a recirculation of the sludge to another anaerobic unit for phosphate removal may be required. In this process, phosphate is taken up by the biomass, and the biological phosphate is released as an inorganic phosphate and removed by chemical precipitation.

Table 4-2 *Characteristics of the MBR permeate*

Parameter	***Unit***	*Average values in feed*	*Average values in permeate*
pH		5.7 ± 0.1	6.7 ± 0.1
Electrical conductivity	µS/cm	1227 ± 53	1354.7 ± 77
MLSS	g/L	5 ± 0.5	5 ± 0.5
COD	mg/L	689.8	50.1 ± 35
TC	mg/L	255.9 ± 4.2	12.8 ± 7
TOC	mg/L	208.5 ± 5.6	7.6 ± 0.7
$N\text{-}NH_4^+$	mg/L	29.9 ± 2.6	<0.5
NH_4^+	mg/L	38.4 ± 3.4	-
$N\text{-}NO_3^-$	mg/L	<0.5	18.7 ± 0.4
NO_3^-	mg/L	-	82.7 ± 1.8
$P\text{-}PO_4^{3-}$	mg/L	8 ± 0.1	16.5 ± 5.4
PO_4^{3-}	mg/L	24.6 ± 0.4	50.5 ± 16.4

4.3.2 Membraneless electrolysis and sono-electrolysis

4.3.2.1 Energy efficiency

25 wt% of KOH was added to the treated wastewater and used as the electrolyte for membraneless hydrogen production in all experiments using nickel and nickel foam electrodes. Fig 4.4 shows the energy efficiency of wastewater electrolysis and sono-electrolysis as a comparison between silent and continuous ultrasonic power. It is clear, that the energy efficiency was higher under sonication conditions as compared to silent conditions. In the case of nickel foam electrodes, the average of the energy conversion efficiencies of 45% and 49% were recorded under silent and continuous sonication conditions respectively using nickel electrodes. A higher energy efficiency was recorded using nickel electrodes. The improvement of the ultrasound effect was more pronounced reaching an average percentage of 50.65% where the efficiency was 47.2% under silent conditions.

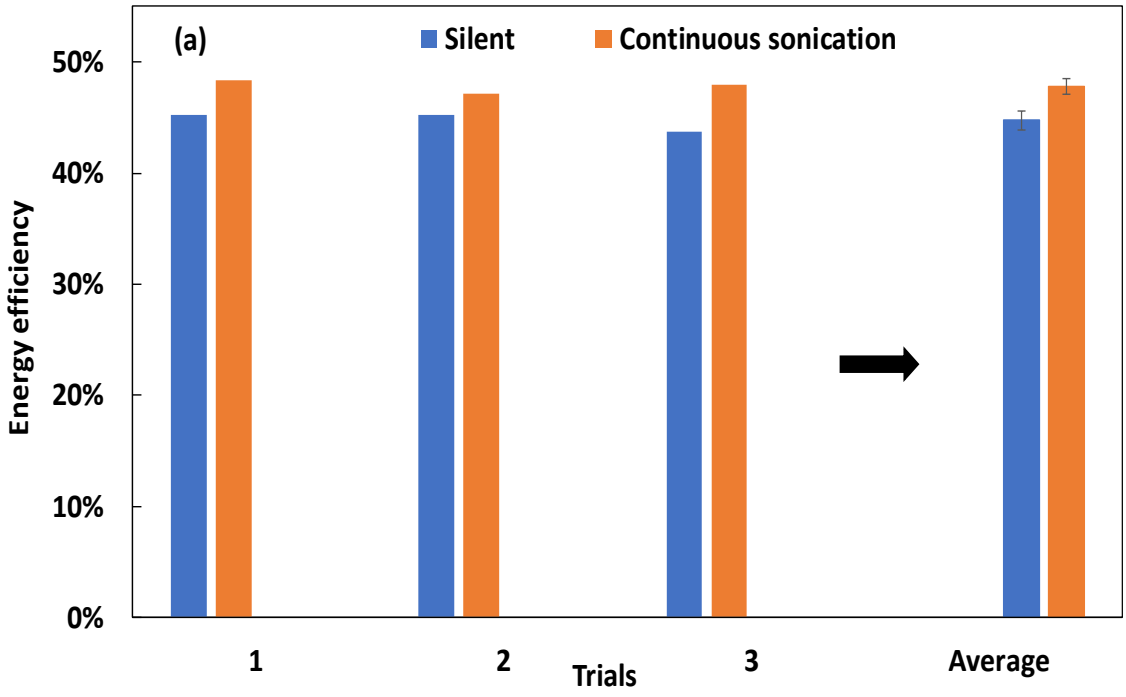

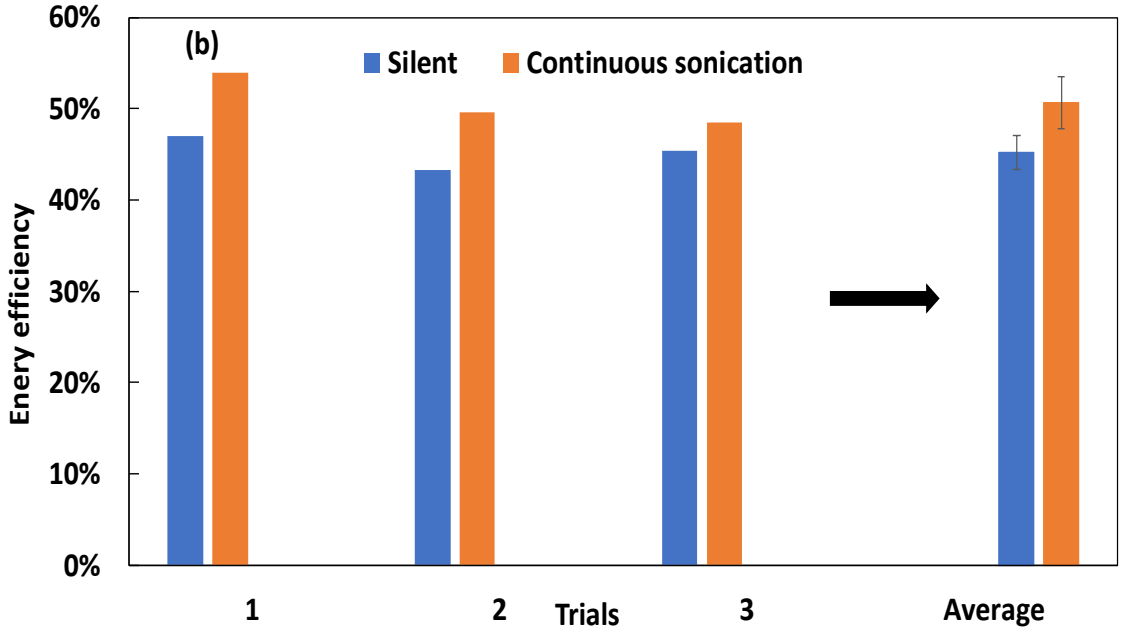

Figure 4.4 *Comparison of silent and continuous ultrasound effects on the energy efficiency for membraneless hydrogen production using nickel foam (a) and nickel electrodes (b).*

4.3.2.2 Kinetics of hydrogen production

Fig 4.5 (a) and (b) show the comparison in terms of hydrogen mass flow rate between silent and sono-electrolysis processes based on treated wastewater, using nickel plate and nickel foam electrodes. No improvement was observed using nickel foam electrodes as shown in Fig.4 (a). On average, the same mass flow rate of 3.99 µg/s was observed in both electrolysis and sono-electrolysis processes. However, an improvement was observed using nickel plate electrodes as shown in Fig.4(b), where the kinetics of hydrogen production increased from 3.82 µg/s under silent conditions to 4.13 µg/s after the integration of sonication.

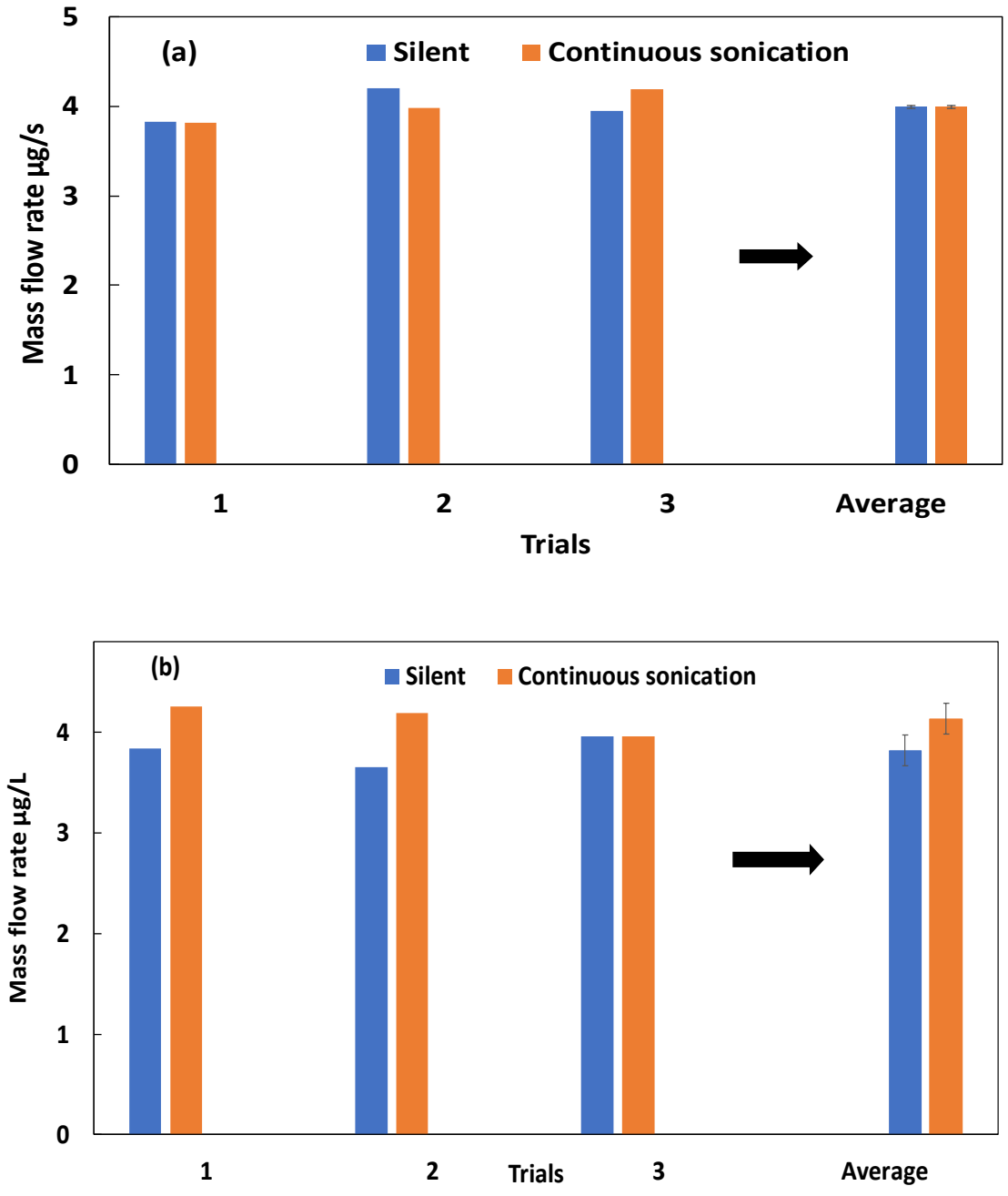

Figure 4.5 *Comparison of silent and continuous sonication effects on mass flow rate for membraneless hydrogen production using nickel foam (a) and nickel electrodes (b).*

4.3.3 Membrane electrolysis and sono-electrolysis

4.3.3.1 Energy efficiency

In the second configuration, Zircon-based diaphragm was integrated as a gas separator in 25 wt% KOH treated water-electrolyte. Fig 4.6 (a) and (b) presents the energy conversion efficiency of membrane electrolysis and sono-electrolysis using nickel foam and nickel electrodes. Due to the high resistance of diaphragm, the energy conversion

efficiency dropped as compared to membraneless configuration. Using nickel foam electrodes, an average energy conversion efficiency of 29.31% and 29.16% were recorded under silent and ultrasounds conditions respectively. Similarly, using nickel electrode, a significant increase in the energy efficiency was observed under silent conditions, where it reached 31.12%, while under sonication conditions the energy conversion efficiency was 1.25% lower than under silent conditions.

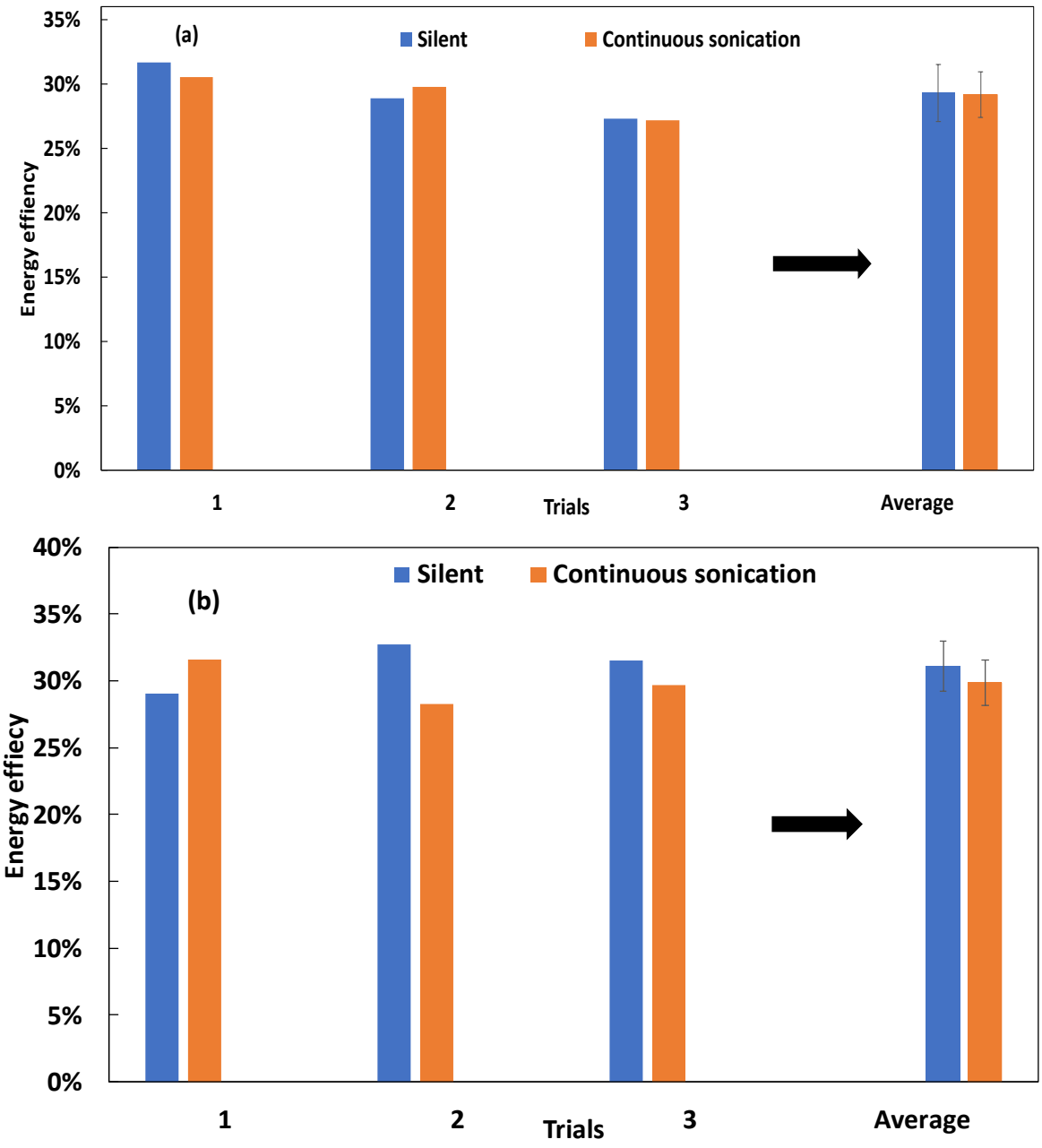

Figure 4.6 *Comparison of silent and continuous ultrasound effects on the energy efficiency for membrane hydrogen production using nickel foam (a) and nickel electrodes (b).*

4.3.3.2 Kinetics of hydrogen production

The results of the mass flow rate of hydrogen produced by electrolysis and sono-electrolysis using the same electrode material as previously are shown in Fig.4.7 (a) and (b). On average, the sonicated mode shows no improvement in hydrogen production kinetics. Using the nickel foam electrodes, the mass flow rate was approximately the same under silent and sonicated conditions with values of 2.42 and 2.43 µg/s, respectively. This rate is significantly lower than for the membraneless setup (approximately 4 µg/s). The same trend was observed when using nickel electrodes, where the average mass flow rates reached 2.65 and 2.55 µg/s under silent and ultrasound conditions, respectively. As in section 3.3.1 (membraneless), it appears that the introduction of the membrane cancels the positive effects of the nickel material and the sonication.

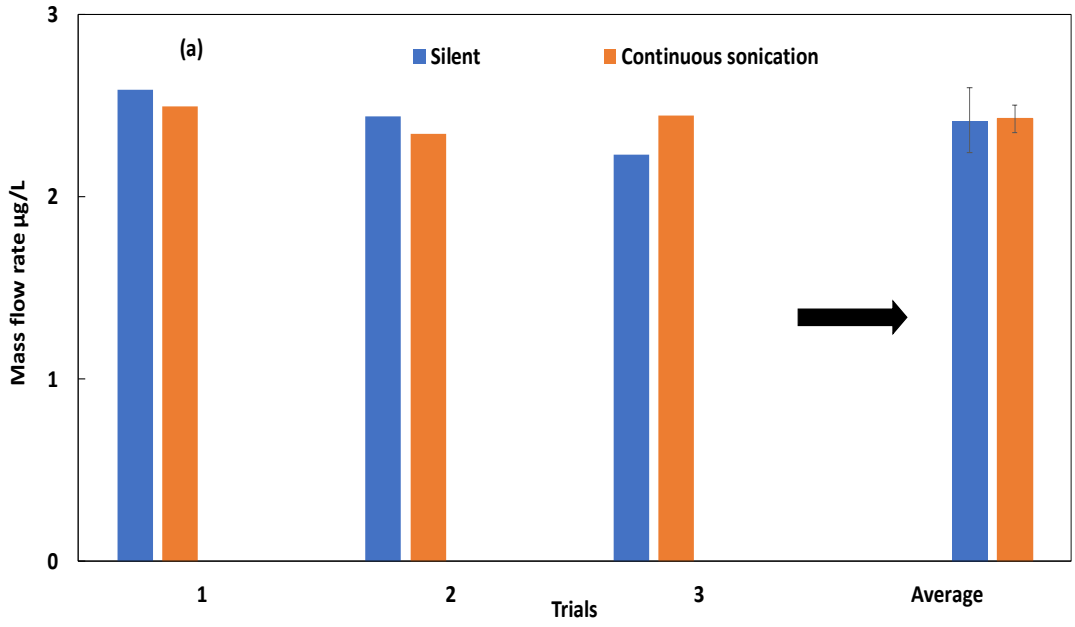

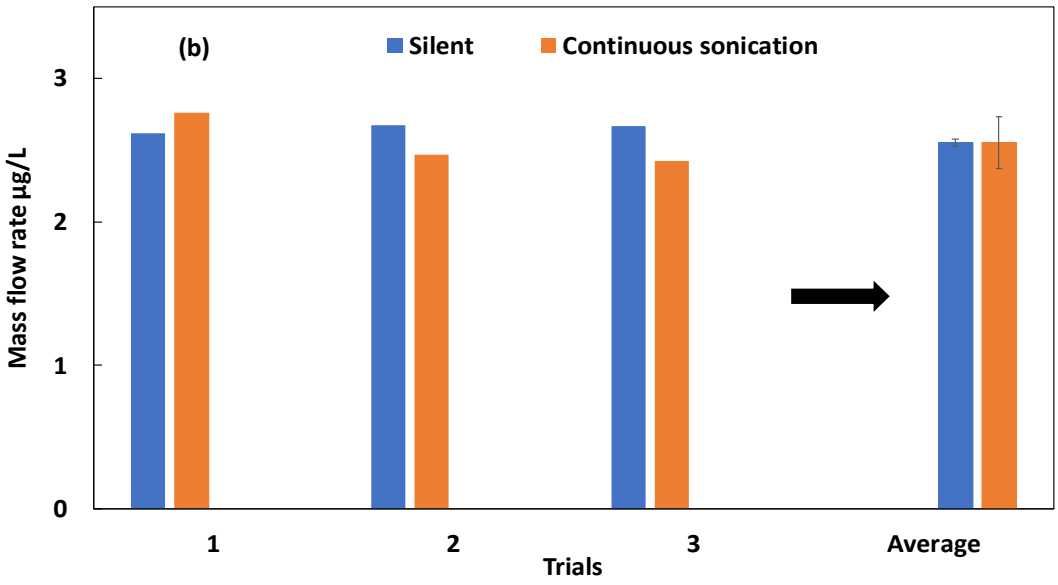

Figure 4.7 *Comparison of silent and continuous sonication effects on mass flow rate for membrane hydrogen production using nickel foam (a) and nickel electrodes (b).*

4.3.4 Hydrogen quality from membrane and membraneless electrolysis

The GC results for hydrogen gas purity are shown in Figure 7. The analyses were performed out in a replicate experiment to validate the results. The purity of the hydrogen gas produced from the permeate reached 85% as shown in Fig 4.8 (a) and (d). After the use of Zirfon membrane, the gas purity was slightly improved to 86%.

The presence of oxygen and nitrogen in the produced gas is shown in Fig 4.8 (b), (c) and (e), (f). In the case of membraneless and for oxygen, a concentration of 2.6% was detected. Similarly for nitrogen, 6.2% of the gas produced. After integration of the gas separator, the percentage of oxygen detected was reduced to 2.4%. The same applies to nitrogen, where 1.5% of the gas was detected in distilled water compared to 6.1% in treated water.

The O_2/H_2 ratio is an important parameter when it comes to the safety threshold of water electrolysis products. Table.3 shows the normalized mass flow of O_2 and H_2 where it can be seen that the O_2/H_2 ratio was kept below the safety threshold.

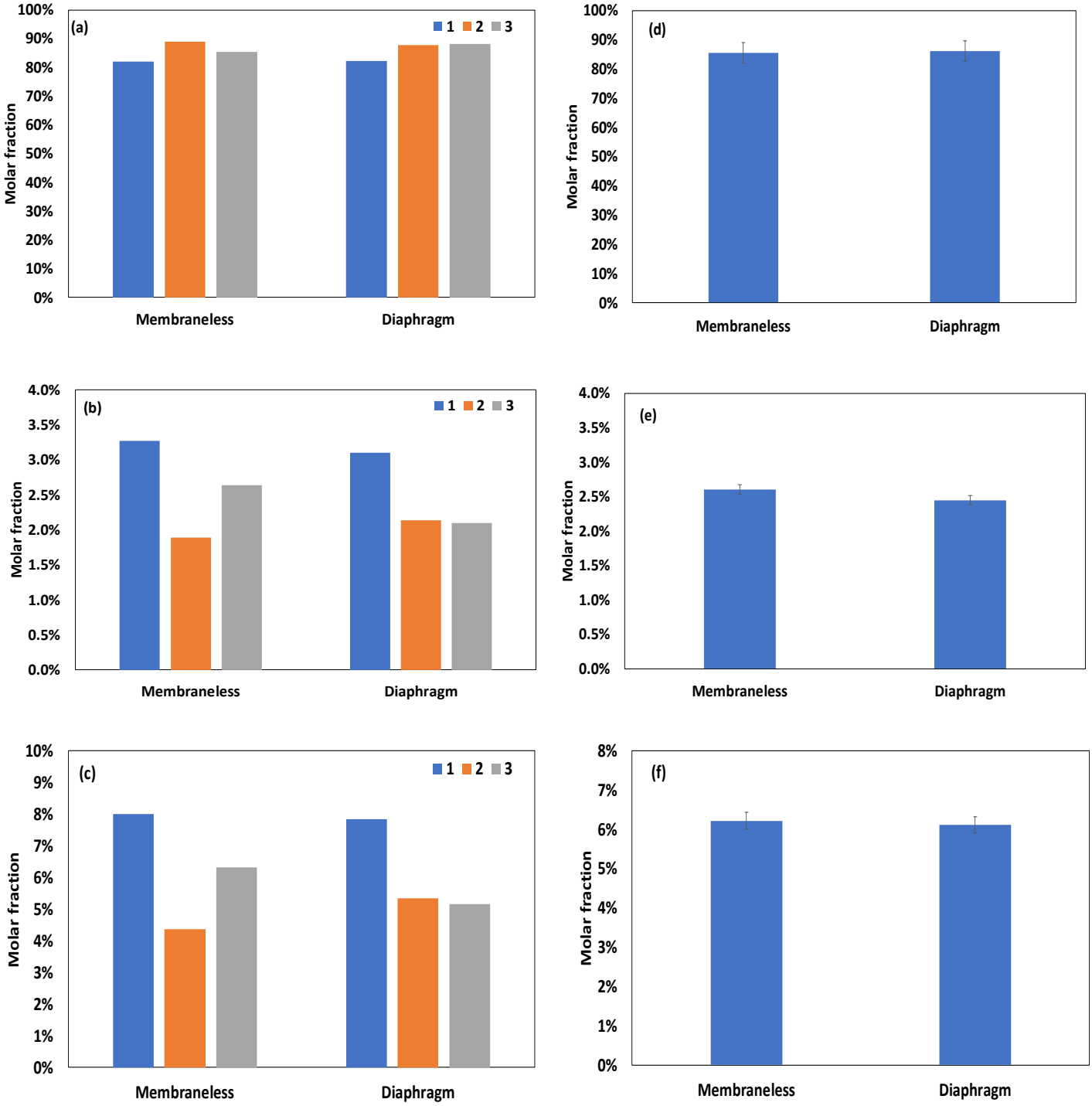

Figure 4.8 *Results of repeated GC-TCD analysis of hydrogen (a) and (d), oxygen (b) and (e), and nitrogen (c) and (f) for membraneless and diaphragm sono-electrolysis of MBR permeates. ((d), (e) and (f) refer to average values).*

Table 4-3 *Normalized molar fraction in the hydrogen-oxygen mixture in the anodic compartment*

		H_2	O_2
Permeate	**Membraneless**	97.000%	3.002%
	Diaphragm	97.671%	2.329%

4.3.5 PV supplied green hydrogen production

In this section, we present the results of the experiments carried out using the PV solar panel as the power source to feed the electrochemical cell. The tests were carried out under both silent and continuously sonicated conditions using the permeate from the membrane bioreactor instead of distilled water as an electrolyte, and the nickel electrodes as electrode' material.

Fig 4.9 (a) and (b) shows the resulting cell voltage from the supply current of the three repeated experiments of PV-supplied alkaline electrolysis using direct connection under silent conditions and continuous ultrasound. The experiments were carried out during the second week of September 2023 by exposing the photovoltaic panel to normal solar radiation in the afternoon at the Karlsruhe University of Applied Sciences (49'01N, 8'23E). Each series of experiments was repeated under identical conditions, while the experiments with silent and then continuous sonication were performed under slightly different incident solar radiations due to climate change.

In terms of cell voltage, Fig.4.9(a) shows the values of the cell voltage resulting from the PV power supply. The figure shows that the cell potential varies slightly from 4.34 V to 4.39 V, between the three studied cases, under silent and sonicated conditions as there was no MPPT regulator connected. giving an average cell potential of 4.36 V and 4.34V in the case of silent and ultrasound conditions, respectively.

The relative standard deviations resulting from the series of repeated experiments were estimated at 6.2% and 1.6% for the input current under silent conditions and continuous ultrasounds, respectively. Regarding the supply current, according to Fig 4.9 (b), average feeding currents of 1.08 and 1.15 A were recorded under silent and

ultrasounds conditions, respectively. The fluctuation due to weather conditions and the absence of an MPPT controller in the system explain the lack of similarity between the cell current and the feed current in each experiment.

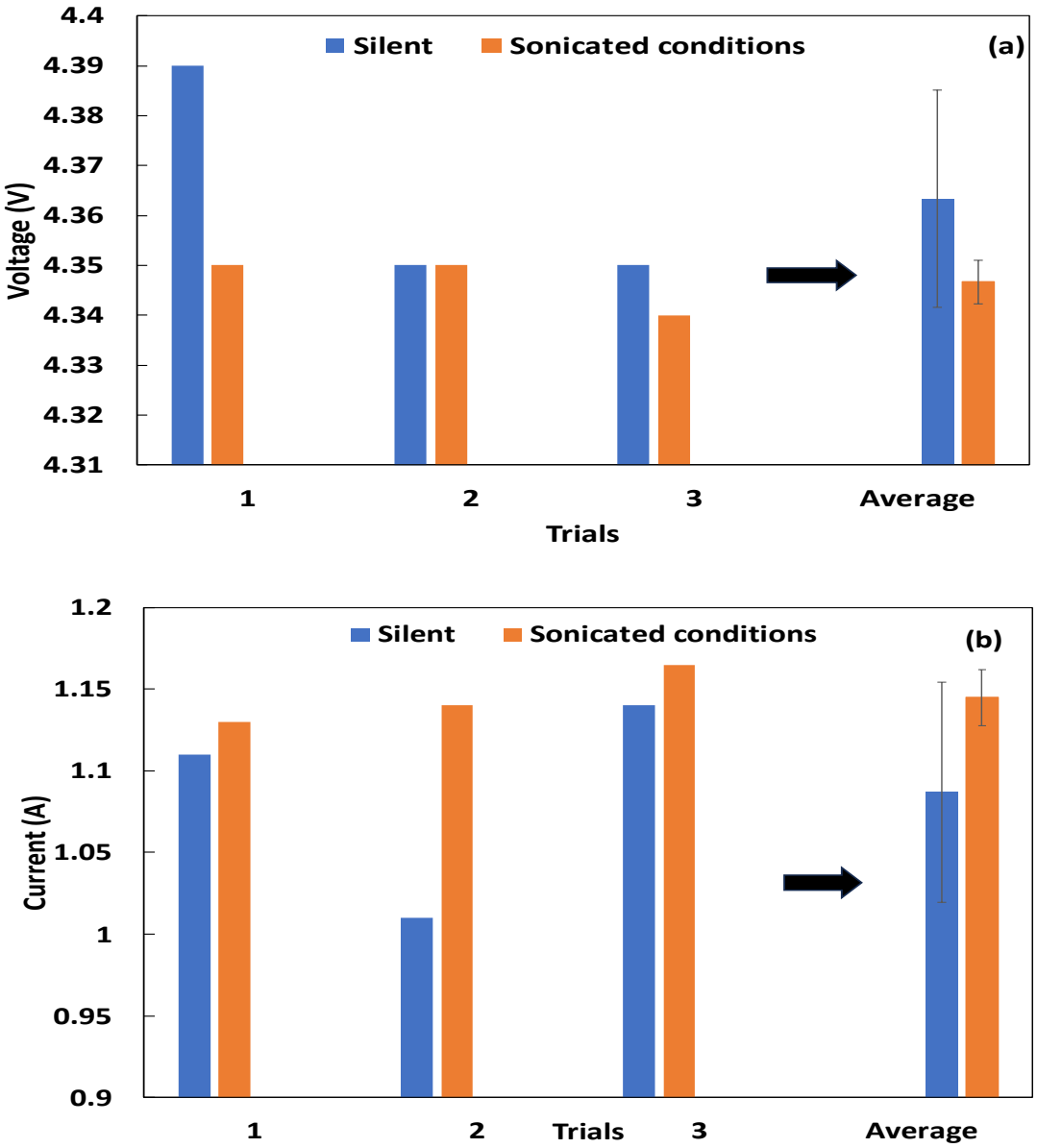

Figure 4.9 *Experimentally measured cell voltage (a) and PV output current (b) under silent and continuous ultrasounds conditions using Nickel plate electrodes and 25% of KOH permeate electrolyte (wt%).*

The energy efficiency and mass flow rate in both cases are shown in Fig. 4.10 (a) and (b), both under silent and continuous ultrasounds conditions of alkaline electrolysis using the permeate as a solvent rather than distilled water. The results are also presented as a series of repeated experiments, with their average values and their relative standard deviations. Overall, it can be seen that the integration of ultrasounds

under a current source does not lead to an improvement in the energy efficiency of the process. On the other hand, an improvement in the flow rate of hydrogen produced was observed by integrating continuous ultrasounds as shown in Fig. 4.10(b). In this case, the improvement observed in the mass flow rate is due to the increase in the desorption process, which leads to better electrochemical production of hydrogen.

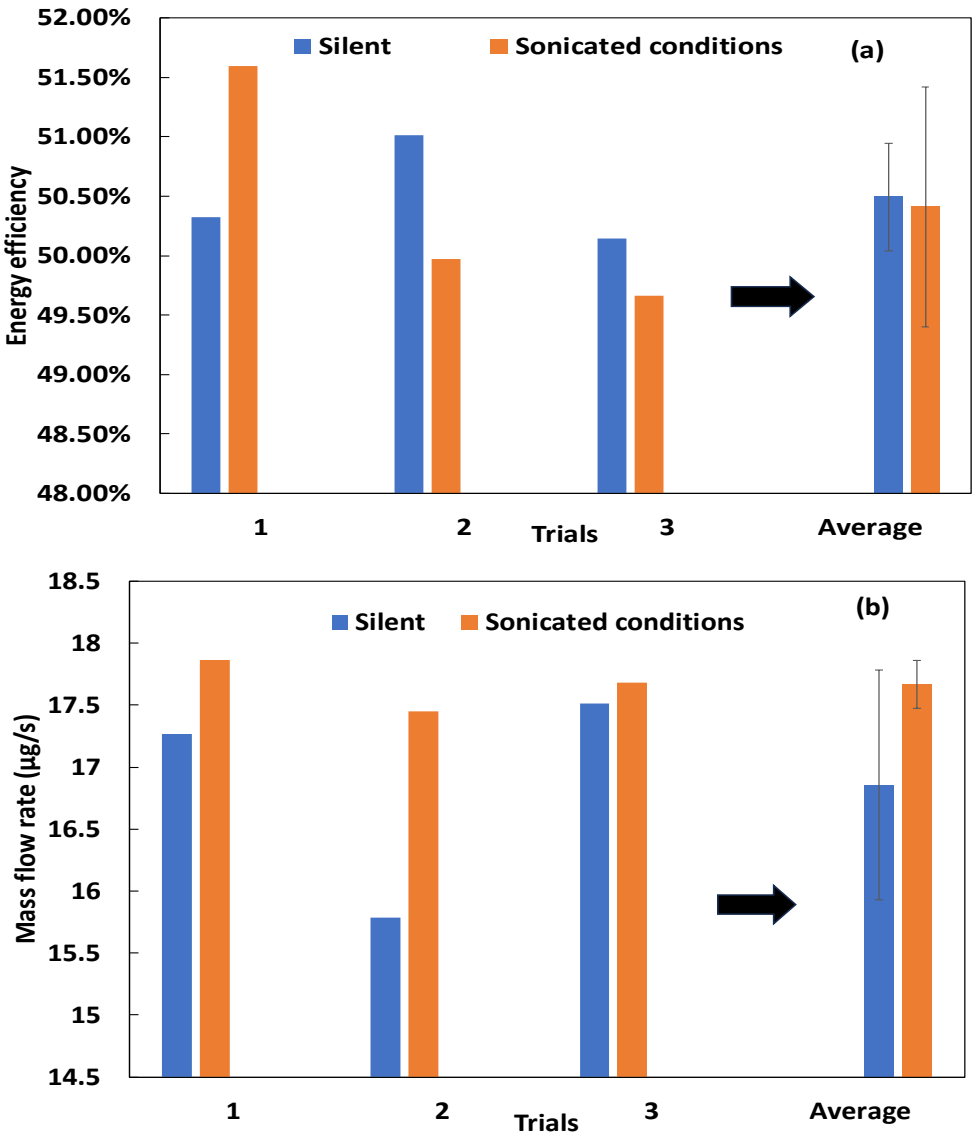

Figure 4.10 *Comparison of PV-solar supplied water electrolysis and water sono-electrolysis processes for hydrogen production in function of experimentally obtained energy efficiency (a) and mass flow rate (b) using nickel electrodes and 25% of KOH permeate electrolyte*

4.4 Conclusion

In the present chapter, we investigated hydrogen production from MBR permeate using ultrasonic assisted alkaline electrolysis. The membrane bioreactor treatment

resulted in COD and TOC removal of 96% each and nitrification rate exceeding 98%. However, although the SSMBR treatment significantly improves water quality, additional treatment steps (TOC and salinity reduction) are required to meet the stringent ASTM Type II limits for H_2 production by electrolysis. In addition, the overall purity of the hydrogen produced reached 85%, with the presence of traces of nitrogen and oxygen gases, while remaining below the safety threshold of the O_2/H_2 ratio.

In the second part, the integration of the ultrasounds field led to a higher energy conversion efficiency and hydrogen production kinetic power when the voltage source was adopted and using membraneless electrolysis and the two structures of nickel electrode (plate and foam). On the other hand, the coupling of ultrasounds to the membrane electrolyzer did not show any enhancement effect on both the energy efficiency and the mass flow rate of produced hydrogen. The enhancement effect observed in the membraneless system was attributed to bubble detachment from the electrode surface leading to a reduction in bubble resistance. However, this effect was negligible compared to the high value of the membrane resistance after the introduction of the membrane.

Under a current source, after replacing distilled water as an electrolyte solvent with the resulting permeate, the integration of ultrasounds did not lead to any improvement in energy efficiency. However, an improvement in the flow rate of the produced hydrogen was observed. In this case, the improvement observed in the mass flow rate was probably due to the increase in the desorption process, which led to a better electrochemical production of hydrogen.

CHAPTER 5

"Hydrogen production under conventional and PV supply from Fresh and wastewater: a comparative study"

CHAPTER 5: HYDROGEN PRODUCTION UNDER CONVENTIONAL AND PV SUPPLY FROM FRESH AND WASTEWATER: A COMPARATIVE STUDY

5.1 Introduction

In the previous chapters, we studied the electrolysis of water using a DC generator and a PV solar panel, on one hand. On the other hand, the electrolysis of fresh water (distilled water) and wastewater has also been studied. Therefore, for a better understanding of the integrated process, we propose in this chapter to gather the results under a comparative study of blue and green hydrogen production (supplied with conventional and renewable electrical powers, respectively) in terms of energy efficiency and gas production kinetics. The same comparison should then be made with distilled water and treated wastewater. In addition, the assessment of the purity of the produced gases will be evaluated.

5.2 Numerical procedure

In the case of the current source (PV panel), the modelling approach is based on the combination of the PV model and the electrolyzer model as shown previously in sections 3.3.1, 1.3.2, 1.3.3 and 1.3.5.

While in the case of the voltage source, the model is based on a feeding voltage of 4V and is simulated according to the electrolyzer's model presented in sections 1.3.2, 1.3.3, 1.3.4 and section 1.3.5

5.3 Experimental procedure

Similarly to the previous chapters, the H-cell setup is used for the comparison study.

In the first comparison, the DC generator and the PV panel are the same models used in sections 1 and 3, as presented in Fig 5.1 (a) and (b).

In the second comparison, the distilled water is replaced by the permeate obtained from the membrane bioreactor system, as described in chapter 4. The power supply in this part is the DC generator (voltage source), while a special focus is given to the

quality of hydrogen produced from fresh water and treated wastewater, according to Fig. 5.2(a) and (b).

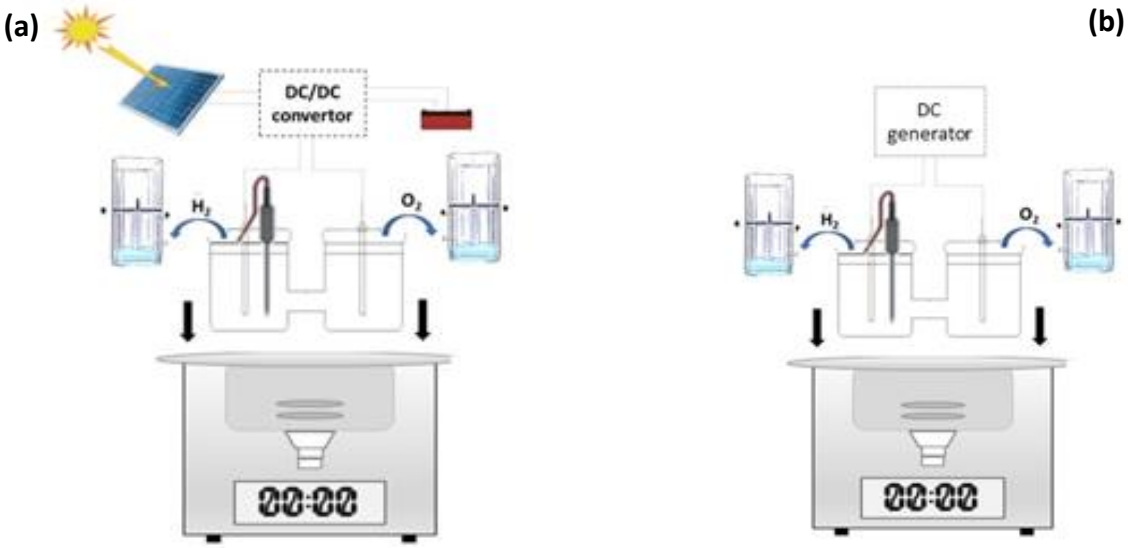

Figure 5.1 *Figure 5.1 Scheme of the comparison base on the power source*

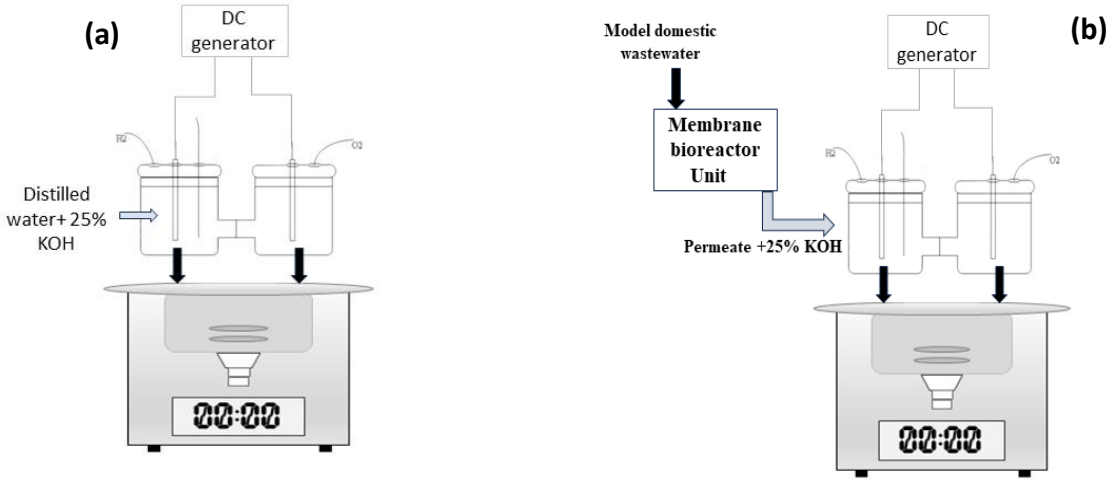

Figure 5.2 *Scheme of hydrogen production process from distilled water (a) and permeate (b)*

5.4 Results and discussion

5.4.1 Performance comparison under voltage and current sources

In the following, we consider the average values of the mass flow rates of produced hydrogen, obtained from the series of repeated experiments in each case. These values

are converted into a normalized parameter defined as the ratio of the mass flow rate of H_2 reported to the average value obtained under silent conditions. The results are presented for two types of power supply, namely a DC voltage source and a PV panel receiving different solar radiations resulting in similar cell voltages. The normalized flow rates are presented in both cases in Fig 5.3 (a) and (b), respectively, under silent, continuous ultrasounds and pulsed ultrasounds conditions of alkaline electrolysis. We can notice that the enhancement in the flow rate of produced hydrogen due to the integration of continuous ultrasounds is higher when a voltage source is used.

Overall, the increase observed when using a voltage source is explained by the increase of the current at constant potential due to the drop in the ohmic resistance, which accelerates the kinetics, added to a promoted recovery of the gas by a better and faster desorption inducing a higher recovery of the gas. Thus, in the case of a voltage source, the improvement of the H_2 rate is due to both effects (increase of current and improved desorption), whereas in the case of a current source such as the PV supply, under a given solar radiation, the noticed improvement in the flow rate of H_2 can only be explained by the improvement of the desorption.

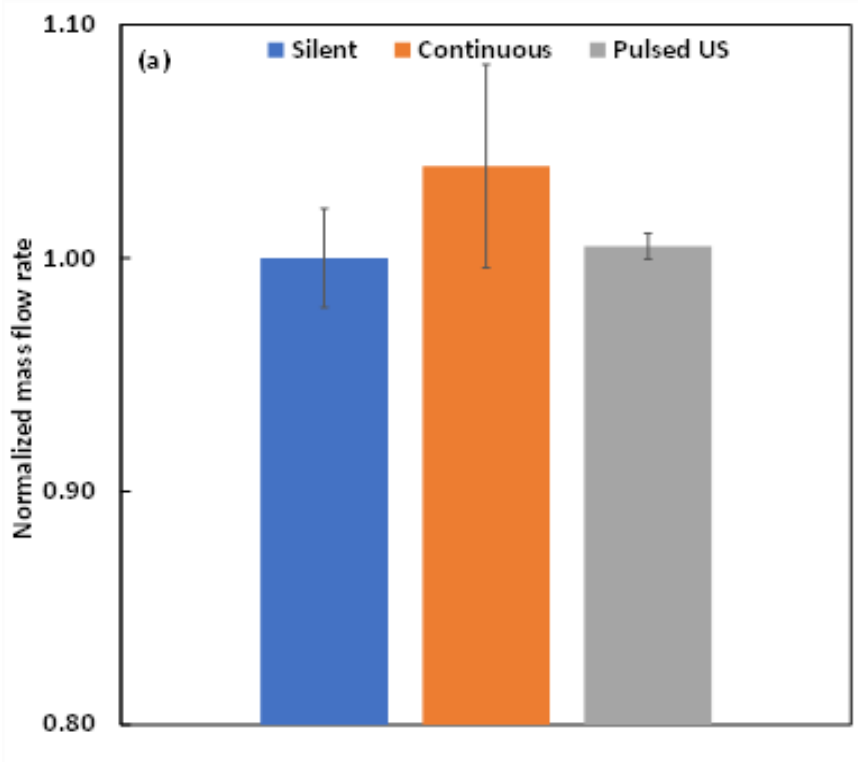

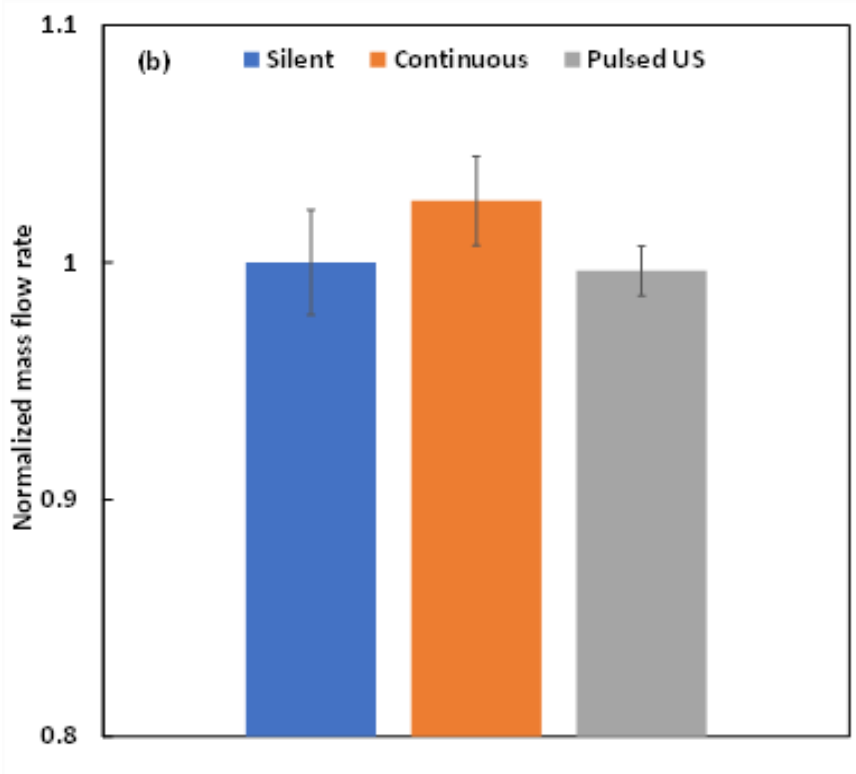

Figure 5.3 *Normalized mass flow rates of hydrogen produced by electrolysis, continuous sono-electrolysis and pulsed sono-electrolysis under supplied by a voltage source (a) and a PV panel (b) using Nickel plate electrodes and 25% of KOH electrolyte (wt%).*

5.4.2 Effect of electrolyte quality

5.4.2.1 Energy efficiency

Fig 5.4 shows a comparison in terms of energy efficiency between fresh and permeate electrolysis under silent and continuous sono-electrolysis using nickel plates and nickel foam electrodes. It is noticeable that the energy efficiency was higher when distilled water was used, as compared to the permeate electrolyte, under silent electrolysis using the two types of electrodes. Whereas, under sonicated conditions, the energy efficiency was similar reaching 48% and 51% for nickel foam and nickel plate electrodes, respectively.

This observation could be explained by the contribution of sonication to the reduction of ohmic resistance and in particular the bubble and electrolyte resistances. In the case of the permeate, the presence of the impurities leads to an increase in the electrolyte resistance and thus reduces the energy efficiency of the process.

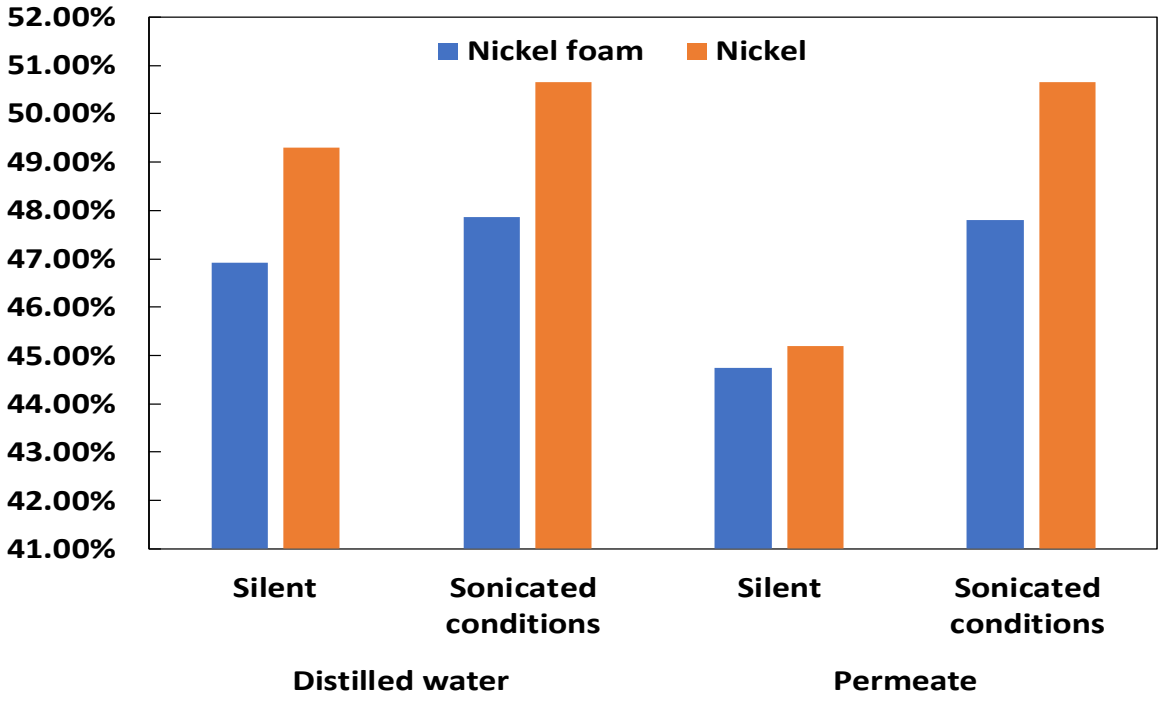

Figure 5.4 *Comparison of silent and continuous ultrasounds effects on the energy efficiency for membraneless fresh and treated water electrolysis for hydrogen production using nickel foam and nickel electrodes.*

5.4.2.2 Kinetics of hydrogen production

Similarly to the previous section, in this part of the study, we illustrate the comparison in terms of mass flow rate of hydrogen between distilled water and permeate electrolysis under silent and continuous sono-electrolysis using nickel plates and nickel foam electrodes. In terms of mass flow rate, the highest values were recorded under sonication conditions and using distilled water when nickel plates were used as electrodes. However, in the case of nickel foam, the presence of impurities in the electrolyte does not really affect the mass flow rate of produced hydrogen.

As mentioned above, ASTM Type II [131] specifies the minimum water quality for electrolysis systems. According to this standard, electrolysis requires TOC impurity concentrations below 50 µg/L, which has not been verified for the permeate of the SSMBR. This may explain the impurities present in the produced gases. The presence

of impurities within the electrolyte may lead to side reactions that compete with the electrochemical production of hydrogen gas.

MBR treatment considerably improves effluent quality, however further treatment processes are required, including for instance activated carbon (AC) for TOC reduction. Moreover, deionization steps should be investigated, especially as MBR does not remove ions. Therefore, the remaining ionic impurities may be present in the electrolyte and may cause material degradation of the electrodes and membrane, and may also affect the purity of the produced gases as shown in Table 5-1.

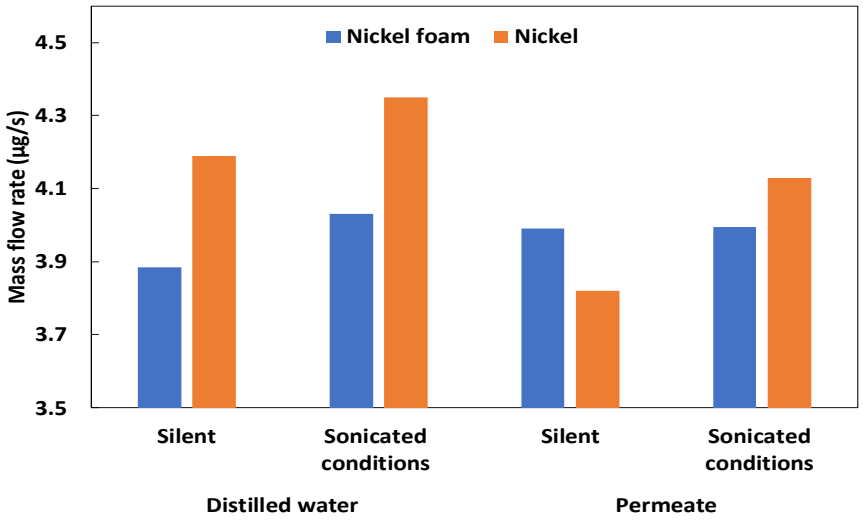

Figure 5.5 *Comparison of silent and continuous ultrasound effects on the kinetics of membraneless fresh and treated water electrolysis for hydrogen production using nickel foam and nickel electrodes.*

Table 5-1 *Impact of impurities on the water electrolysis process*

Impurity	Source	Effect
Cl^-	$CaCl_2$	Corrosion of nickel, with the exception of special structures [131], contamination of H_2 by Cl_2 gas.
Na^+	$NaHCO_3$	No effect reported in the literature [131].
HCO_3^-	$NaHCO_3$	Reduction of the electrolyte conductivity, pore-clogging in membrane systems [131].
NH_4^+	NH_4Cl	Contamination of H_2 by NH_3 gas.
NO_3^-	----	No effect has been reported in the literature.
Ca^+	$CaCl_2$	Depositing at high pH can cause mass transport problems at electrodes [131].

5.4.3 Quality of hydrogen

The GC results for hydrogen gas purity are shown in Fig 5.6. The analyses were carried out in a series of repeated experiment to validate the results. As it can be seen in Fig 5.6 (a) and (d), the purity of the hydrogen gas produced from distilled water reached 90%, which was 5% higher than in the case of treated wastewater. After the use of Zirfon diaphragm, the gas purity has increased to 96% and 86% using distilled and treated water, respectively.

Figs. 5.6 (b), (c), (e) and (f) show the presence of oxygen and nitrogen in the produced gas mixture. In the case of membraneless configuration, a concentration of 1.8% and 2.6% was detected for oxygen using distilled and treated water, respectively. Similarly for nitrogen, fractions of 4.6% and 6.2% were detected using distilled and treated water, respectively.

After the integration of the gas separator, the percentage of oxygen detected was reduced to 0.6% using distilled water and to 2.4% using treated water. The same applies to nitrogen, where 1.5% of the gas was detected in distilled water, compared to 6.1% in treated water.

The presence of oxygen and, in particular, nitrogen in high concentrations, even in the electrolysis of distilled water with the gas separator, is due to air contamination. In addition, from a safety point of view, the ratio of H_2/O_2 presents an important criterion, therefore, for the four experiments and setups, the ratio of H_2/O_2 was verified, and all the obtained values were under the safety threshold (3.8% O_2 in H_2 at 20°C and 1 atm) as shown in Table 5-2.

Examples of purity requirements for hydrogen is the polymer exchange membrane fuel cell (PEMFC) are shown in Table 5-3. Accordingly, novel and highly efficient purification technologies for the production of low cost and high quality H_2 should be urgently developed to support large-scale applications of H_2 energy in the transport sector [132].

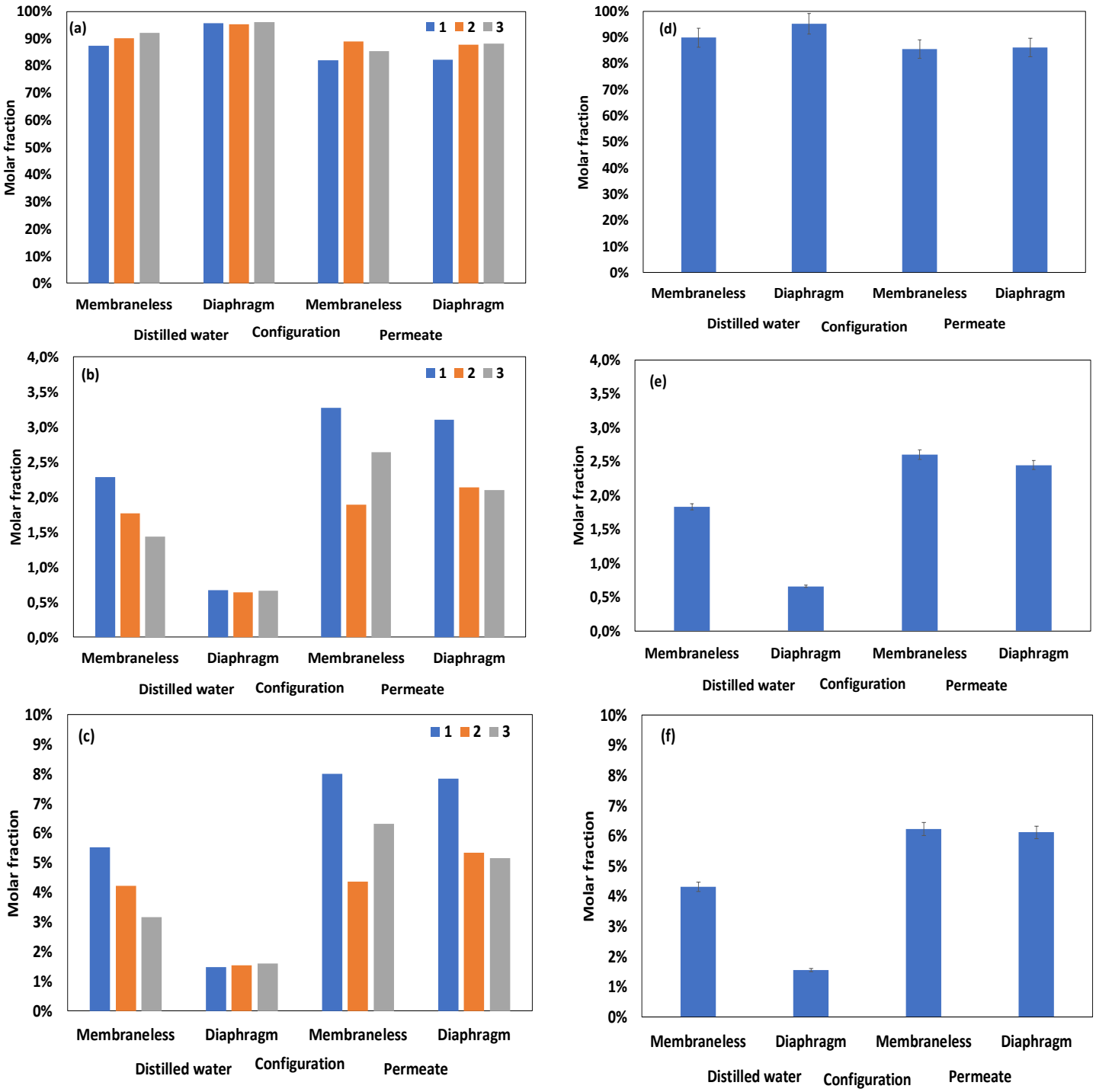

Figure 5.6 *Results of repeated GC-TCD analysis of hydrogen (a) and (d), oxygen (b) and (e) , and nitrogen (c) and (f) for membraneless and diaphragm sono-electrolysis of distilled water and MBR permeates. ((d), (e) and (f) refer to average values).*

Table 5-2 *Normalized molar fraction in the hydrogen-oxygen mixture in the anodic compartment*

		H_2	O_2
Distilled water	**Membraneless**	98.466%	1.534%
	Diaphragm	99.314%	0.687%
Permeate	**Membraneless**	97.000%	3.002%
	Diaphragm	97.671%	2.329%

Table 5-3 *Requirements for the impurities content in H_2 for fuel cells and purification technologies [129]*

Compound	**Pure H_2**	**High pure H_2**	**Ultrapure H_2**	**Possible purification techologies**
H_2	99.99%	99.999%	99.9999%	
Total non H_2 gases	/	10 ppm	1ppm	
H_2O	10 ppm	3 ppm	0.5 ppm	Elevated temperature pressure swing adsorption Carbon-based membranes [132]
O_2	5 ppm	1 ppm	0.2 ppm	Carbon-based membranes [132]
N_2	60 ppm	5 ppm	0,4 ppm	Pressure swing adsorption [132]
He, Ar	Agreed by supply and demand	Agreed by supply and demand	0.2-0.4 ppm	Pressure swing adsorption [132]
CO_2	5 ppm	1 ppm	0.1 ppm	Pressure swing adsorption Metal, polymer and carbon-based membrane [132]
CO	5 ppm	1 ppm	0.1 ppm	Pressure swing adsorption [132]

5.5 Conclusion

In this chapter, the comparison of water electrolysis powered by a voltage and a current energy source in terms of energy efficiency and kinetics of gas production, on the one hand, and on the other hand, electrolytic hydrogen production from distilled and permeate solutions was discussed. It has been shown that, the improvement in the flow rate of hydrogen produced by the integration of continuous ultrasounds is greater when a voltage source is used. This improvement can be explained by the increase in current at constant potential due to the reduction of the ohmic resistance, thus accelerating the kinetics and improving the gas recovery through greater and faster desorption.

The purity of the hydrogen gas produced from distilled water was 5% higher than in the case of the MBR permeate with the presence of traces of nitrogen and oxygen. Then, the gas separator has contributed to increase the purity of the hydrogen to reach 96% when using distilled water and 86% when using MBR permeate. In all the cases, the explosive mixture threshold was never reached.

GENERAL CONCLUSION

GENERAL CONCLUSION

The main objective of the present research project is to develop an innovative process for the production of green hydrogen based on wastewater sono-electrolysis powered by photovoltaic solar energy and using low-cost materials. The parametric study showed that the increase in ionic conductivity when using the KOH solution compensates for the associated increase in ohmic resistance and leads to accelerated kinetics of hydrogen production. The nickel electrodes (plate and foam structures) show a better performance, and the integration of the ultrasonic field in the case of the nickel foam electrodes and the KOH electrolyte would compensate the increase due to the temperature rise under silent conditions, leading to a gain in the energy supplied to the heating module.

The decrease in bubble resistance due to ultrasound was estimated under silent and continuous sonication. The highest reduction was observed with nickel foam electrodes using KOH electrolyte, with a reduction rate of 64%. The experiments showed an average improvement in H_2 rate of 3.93% and a relative gain in energy conversion efficiency of 2.76% when sonication was integrated. While the modelling results showed that the polarisation curves obtained experimentally under silent and ultrasonic conditions showed quasi-linear evolution, related to the ohmic overpotential. The obtained average ohmic resistance was estimated to be 9.03 Ω under silence and 8.38 Ω under ultrasound, a decrease of 7.2%.

The Zirfon UTP 500 diaphragm demonstrated high energy efficiency, stability in high alkaline conditions, and favorable hydrogen production kinetics compared to other membranes used. However, the modeling results indicated that the effect of ultrasound on reducing the ohmic resistance was not significant compared to the high resistance of the Zirfon diaphragm. On the other hand, the propagation of ultrasound within the electrolyte improved the hydrogen production kinetics despite the presence of the diaphragm.

From the modelling of the coupled PV-electrolysis, indirect continuous sono-electrolysis showed the lowest electrode coverage with a value of 37%, compared to 82% under silent conditions and 58.3% under pulsed sonication. Thus, in the presence of indirect continuous sonication, the bubble resistance is 76% lower than in the absence of sonication and 52% lower than under pulsed sonication. In addition, the effect of ultrasounds cannot be entirely attributed to improvements in mass transport properties. Such an effect, if present, appears to be limited and negligible. Moreover, it cannot be explained by a change in Faraday efficiency. This is because the experimental verification has shown that the Faraday efficiency remains consistently equal to 1 regardless of the presence or absence of ultrasounds.

Furthermore, the comparison between measured and simulated hydrogen mass flow rates showed a small difference of 5.92%. The experimental values may be influenced by the presence of water vapour. Therefore, the most efficient mode for bubble removal by acoustic cavitation action is found to be the integration of continuous ultrasounds.

Finally, we focus on replacing the distilled water with the MBR treated water. The MBR treatment resulted in 96% COD and TOC removal and >63% nitrification. However, in order to meet the stringent ASTM Type II limits for H_2 production by electrolysis, additional treatment steps (TOC and salinity reduction) are required. Furthermore, the overall purity of the hydrogen produced reached 85%, with traces of nitrogen and oxygen gases present, while remaining below the O_2/H_2 safety threshold.

Then, by adopting the voltage source and using membraneless electrolysis and the two types of nickel electrode structures, the integration of the ultrasonic field led to higher energy conversion efficiency and hydrogen production kinetic power. On the other hand, there was no improvement in both the energy efficiency and the mass flow rate of hydrogen produced when ultrasound was coupled to a membrane electrolyzer.

REFERENCES

1. Jain IP. Hydrogen the fuel for 21st century. *Int J Hydrogen Energy* 2009;**34**:7368–78.

2. Kerboua K, Hamdaoui O. Energetic challenges and sonochemistry : A new alternative for hydrogen production ? *Curr Opin Green Sustain Chem* 2019;**18**:84–9.

3. Islam H, Burheim OS, Pollet BG. Sonochemical and Sonoelectrochemical Production of Hydrogen. *Ultrason - Sonochemistry* 2018, DOI: 10.1016/j.ultsonch.2018.08.024.

4. Islam MH, Lamb JJ, Burheim OS *et al.* Ultrasound-assisted electrolytic hydrogen production. *Micro-Optics and Energy: Sensors for Energy Devices*. 2020, 73–84.

5. Piergiovanni Domenighini, Ferdinando Costantino, Pier Luigi Gentili, Anna Donnadio, Morena Nocchetti, Alceo Macchioni FR and FC. Future perspectives in green Hydrogen production by catalyzed sono-photolysis of water. *Sustain Energy Fuel* 2021;**00**, DOI: 10.1039/D4SE00277F.

6. Ismail AA, Bahnemann DW. Photochemical splitting of water for hydrogen production by photocatalysis: A review. *Sol Energy Mater Sol Cells* 2014;**128**:85–101.

7. Corredor J, Rivero MJ, Rangel CM *et al.* Comprehensive review and future perspectives on the photocatalytic hydrogen production. *J Chem Technol Biotechnol* 2019;**94**:3049–63.

8. Khan T, Yu M, Waseem M. Review on recent optimization strategies for hybrid renewable energy system with hydrogen technologies : State of the art , trends and future directions. *Int J Hydrogen Energy* 2022;**47**:25155–201.

9. Mcphail SJ. Hydrogen energy: State of the art and perspectives. *Current Trends and Future Developments on (Bio-) Membranes*. Elsevier Inc., 2020, 3–19.

10. Liu G, Sheng Y, Ager JW *et al.* Research advances towards large-scale solar hydrogen production from water. *EnergyChem* 2019;**100014**:1–51.

11. Li X, Sun X, Song Q *et al.* A critical review on integrated system design of solar thermochemical water-splitting cycle for hydrogen production Organic Rankine cycle.

Int J Hydrogen Energy 2022;**47**:33619–42.

12. Torres-palma RA, Serna-galvis EA. *Sonolysis*. Elsevier Inc., 2018.

13. Kishor U, Guptha S, Pandi N *et al.* A review on recent advances in hydrogen energy , fuel cell , biofuel and fuel refining via ultrasound process intensification. *Ultrason Sonochem* 2021;**73**:105536.

14. Theerthagiri J, Madhavan J, Lee SJ *et al.* Sonoelectrochemistry for energy and environmental applications. *Ultrason Sonochem* 2020;**63**:104960.

15. Cataldo F. Effects of ultrasound on the yield of hydrogen and chlorine during electrolysis of aqueous solutions of NaCl or HCl. *J Electroanal Chem* 1992;**332**:325–31.

16. G.pollet B. *Power Ultrasound in Electrochemistry.*, 2012.

17. Walton DJ, Burket LD, Murphy MM. Sonoelectrochemistry :and oxygen evolution chlorine, hydrogen at platinised platinium. *Elecrrochimica ACta* 1996;**41**:2747–51.

18. Li S De, Wang CC, Chen CY. Water electrolysis in the presence of an ultrasonic field. *Electrochim Acta* 2009;**54**:3877–83.

19. Mcmurray HN, Worsley DA, Wilson BP. Hydrogen evolution and oxygen reduction at a titanium sonotrode Hydrogen evolution and oxygen reduction at a titanium sonotrode. *Chem Commun* 1998:887–8.

20. Zadeh SH. Hydrogen Production via Ultrasound-Aided Alkaline Water Electrolysis. *Autom Control Eng* 2014;**2**:103–9.

21. Pollet B, Lorimer JP, Phull SS *et al.* The effect of ultrasonic frequency and intensity upon electrode kinetic parameters for the Ag (S 2 O 3) 3 2 / Ag redox couple. *J Appl Electrochem* 1999;**29**:1359–66.

22. Budischak C, Honsberg, Christiana RLO. Electroanalytic effects of ultrasound on a hydrogen evolution reaction in KOH. *33rd IEEE Photovoltaic Specialists Conference*. 2008, 1–3.

23. Symes D. Sonoelectrochemical (20 kHz) production of hydrogen from aqueous solutions. 2011.

24. Lin M, Hourng L. Ultrasonic wave field effects on hydrogen production by water electrolysis. *J Chinese Inst Eng* 2014;**54**:37–41.

25. Pollet BG. A Short Introduction to Sonoelectrochemistry. *Electrochem Soc Interface* 2018;**27**:41–2.

26. Stubna I, Csáki S, Ondruska J. Hofmann's electrolyser in laboratory works. *AIP Conf Proc* 2019;**2152**, DOI: 10.1063/1.5124776.

27. Wang M, Wang Z, Gong X *et al.* The intensification technologies to water electrolysis for hydrogen production – A review. *Renew Sustain Energy Rev* 2014;**29**:573–88.

28. Zeng K, Zhang D. Recent progress in alkaline water electrolysis for hydrogen production and applications. *Prog Energy Combust Sci* 2010;**36**:307–26.

29. Kerboua K, Hamdaoui O, Islam MH *et al.* Low carbon ultrasonic production of alternate fuel: Operational and mechanistic concerns of the sonochemical process of hydrogen generation under various scenarios. *Int J Hydrogen Energy* 2021, DOI: 10.1016/j.ijhydene.2021.05.191.

30. Tijani AS, Afiqah N, Kamarudin B. ScienceDirect Investigation of the effect of charge transfer coefficient (CTC) on the operating voltage of polymer electrolyte membrane (PEM) electrolyzer. *Int J Hydrogen Energy* 2018;**19**:1–14.

31. Sellami MH, Loudiyi K. Electrolytes behavior during hydrogen production by solar energy. *Renew Sustain Energy Rev* 2017;**70**:1331–5.

32. Mohamed B, Ali B, Ahmed B *et al.* Study of hydrogen production by solar energy as tool of storing and utilization renewable energy for the desert areas. *Int J Hydrogen Energy* 2016;**41**:20788–806.

33. Leroy RL, Bowen CT, Claire P *et al.* The thermodynamics of aqueous water electrolysis. *J Electrochem Soc* 1980;**127**:1954–62.

34. Vincenzo Liso, Giorgio Savoia, Samuel Simon Araya SKK. Modelling and experimental analysis of a polymer electrolyte membrane water electrolysis cell at different operating temperatures. *energies* 2018;**11**:1–18.

35. Allen J. Bard, Larry R. Faulkner HSW. *Elechtrochemical Methods , Fundamentals and Applications.*, 2022.

36. Abul Kalam Azad, Khan MMK. *Bioenergy Resources and Technologies.*, 2021.

37. Gambou F, Guilbert D, Zasadzinski M *et al.* A comprehensive survey of alkaline electrolyzer modeling : electrical domain and specific electrolyte conductivity To cite this version : HAL Id : hal-03663132 A comprehensive survey of alkaline electrolyzer modeling : electrical domain and specific elect. *energies* 2022;**15**.

38. Henao C, Agbossou K, Hammoudi M *et al.* Simulation tool based on a physics model and an electrical analogy for an alkaline electrolyser. *J Power Sources* 2014;**250**:58–67.

39. Abdin Z, Webb CJ, Gray EMA. Modelling and simulation of an alkaline electrolyser cell. *Energy* 2017;**138**:316–31.

40. Kibria MF, Mridha MS. Electrochemical studies of the nickel electrode for the oxygen evolution reaction. *Int J Hydrogen Energy* 1996;**21**:179–82.

41. Kibria MF, Mridha MS, Khan AH. Electrochemical studies of a nickel electrode for the hydrogen evolution reaction. *Int J Hydrogen Energy* 1995;**20**:435–40.

42. Amores E, Rodrı L, Clemente-jul C. Semi-empirical model and experimental validation for the performance evaluation of a 15 kW alkaline water electrolyzer nica S a. *Int J Hydrogen Energy* 2018;**43**:1–14.

43. Toma M, Fukutomi S, Asakura Y *et al.* A calorimetric study of energy conversion efficiency of a sonochemical reactor at 500kHz for organic solvents. *Ultrason Sonochem* 2011;**18**:197–208.

44. Mason TJ. *Sonochemistry : The Uses of Ultrasound in Chemistry*. Cambridge: Royal Society of Chemistry, 1990.

45. Contamine RF, Wilhelm AM, Berlan J *et al.* Power measurement in sonochemistry. *Ultrason Sonochem* 1995;**2**:S43–7.

46. Kerboua K, Hamdaoui O, Alghyamah A. Acoustic frequency and optimum sonochemical production at single and multi-bubble scales: A modeling answer to the scaling dilemma. *Ultrason Sonochem* 2021;**70**:105341.

47. Kerboua K, Hamdaoui O, Al-Zahrani S. Sonochemical production of hydrogen: A numerical model applied to the recovery of aqueous methanol waste under oxygen-argon atmosphere. *Environ Prog Sustain Energy* 2021;**40**, DOI: 10.1002/ep.13511.

48. Yasui K. Alternative model of single bubble sonoluminescence. *Phys Rev E* 1997;**56**:6750–60.

49. Ye L, Zhu X. Analysis of the effect of impact of near-wall acoustic bubble collapse micro-jet on Al 1060. *Ultrason Sonochem* 2017;**36**:507–16.

50. Roberto S, Avila G, Song C *et al.* Fast transient microjets induced by hemispherical cavitation bubbles. *J Fluid Mech* 2015;**767**:31–51.

51. Schramm-Baxter J, Mitragotri S. Needle-free jet injections: Dependence of jet penetration and dispersion in the skin on jet power. *J Control Release* 2004;**97**:527–35.

52. Kerboua K, Merouani S, Hamdaoui O *et al.* How do dissolved gases affect the sonochemical process of hydrogen production? An overview of thermodynamic and mechanistic effects – On the "hot spot theory." *Ultrason Sonochem* 2021;**72**:105422.

53. Kerboua K, Hamdaoui O. Void fraction , number density of acoustic cavitation bubbles , and acoustic frequency : A numerical investigation. *J Acoust Soc Am* 2019;**146**:2240–52.

54. Kerboua K, Hamdaoui O, Alghyamah A. Numerical characterization of acoustic cavitation bubbles with respect to the bubble size distribution at equilibrium. *Processes* 2021;**9**:1–21.

55. Huang H, Shu D, Fu Y *et al.* Synchrotron radiation X-ray imaging of cavitation

bubbles in Al-Cu alloy melt. *Ultrason Sonochem* 2014;**21**:1275–8.

56. Le Bideau D, Mandin P, Benbouzid M *et al.* Review of necessary thermophysical properties and their sensivities with temperature and electrolyte mass fractions for alkaline water electrolysis multiphysics modelling. *Int J Hydrogen Energy* 2019;**44**:4553–69.

57. Allebrod F, Chatzichristodoulou C, Mollerup PL *et al.* Electrical conductivity measurements of aqueous and immobilized potassium hydroxide. *Int J Hydrogen Energy* 2012;**37**:16505–14.

58. Dekker M. Measurement of The Electrolytic Conductance. *Ewing's Analytical Instrumentation Handbook*. 2005, 561–78.

59. Millet P, Grigoriev S. Water Electrolysis Technologies. *Renewable Hydrogen Technologies*. 2013, 19–41.

60. Li W, Tian H, Ma L *et al.* Materials Advances Low-temperature water electrolysis : 2022, DOI: 10.1039/D2MA00185C.

61. Ganley JC. High temperature and pressure alkaline electrolysis. *Int J Hydrogen Energy* 2009;**34**:3604–11.

62. Gilliam RJ, Graydon JW, Kirk DW *et al.* A review of specific conductivities of potassium hydroxide solutions for various concentrations and temperatures. *Int J Hydrogen Energy* 2007;**32**:359–64.

63. Jang D, Cho H, Kang S. Numerical modeling and analysis of the effect of pressure on the performance of an alkaline water electrolysis system. *Appl Energy* 2021;**287**:116554.

64. Jang D, Choi W, Cho H *et al.* Numerical modeling and analysis of the temperature effect on the performance of an alkaline water electrolysis system. *J Power Sources* 2021;**506**:230106.

65. Hazarika K, Gogoi SB. Comparative Study of an Enhanced Oil Recovery process with

various chemicals for Naharkatiya Oil Field. *Int J Appl Sci Biotechnol* 2014;**2**:432–6.

66. Schalenbach M, Zeradjanin AR, Kasian O *et al.* A perspective on low-temperature water electrolysis - Challenges in alkaline and acidic technology. *Int J Electrochem Sci* 2018;**13**:1173–226.

67. Hitchcock LB, Mcilhenny JS. Viscosity and Density of Pure Alkaline Solutions and Their Mixtures. *Ind Eng Chem* 1935;**27**:461–6.

68. Nazari-Mahroo H, Pasandideh K, Navid HA *et al.* How important is the liquid bulk viscosity effect on the dynamics of a single cavitation bubble? *Ultrason Sonochem* 2018;**49**:47–52.

69. Wu H, Zheng H, Li Y *et al.* Effects of surface tension on the dynamics of a single micro bubble near a rigid wall in an ultrasonic field. *Ultrason Sonochem* 2021;**78**:105735.

70. Asakura Y, Yasuda K. Frequency and power dependence of ultrasonic degassing. *Ultrason Sonochem* 2022;**82**:105890.

71. Bhatnagar S, Schiffter H, Coussios CC. Exploitation of acoustic cavitation-induced microstreaming to enhance molecular transport. *J Pharm Sci* 2014;**103**:1903–12.

72. Abe JO, Popoola API, Ajenifuja E *et al.* ScienceDirect Hydrogen energy , economy and storage : Review and recommendation. 2019;**4**, DOI: 10.1016/j.ijhydene.2019.04.068.

73. Chi J, Yu H. Water electrolysis based on renewable energy for hydrogen production. *Chinese J Catal* 2018;**39**:390–4.

74. Arafat ES. Applications of Porous Flow-Through Electrodes. *J Electrochem Soc Electrochem Sci Technol* 1983;**130**:380–4.

75. Li, Dmitri Bessarabov, Haijiang Wang, Hui Li NZ. *PEM Electrolysis for Hydrogen Production Principles and Applications.*, 2016.

76. Zadeh SH. Sonoelectrochemical Production of Hydrogen via Alkaline Water

Electrolysis. 2012.

77. Merouani S, Hamdaoui O, Boutamine Z *et al.* Experimental and numerical investigation of the effect of liquid temperature on the sonolytic degradation of some organic dyes in water. *Ultrason Sonochem* 2016;**28**:382–92.

78. Löning JM, Horst C, Hoffmann U. Investigations on the energy conversion in sonochemical processes. *Ultrason Sonochem* 2002;**9**:169–79.

79. Al-Juboori RA, Yusaf T, Bowtell L. Energy Conversion Efficiency of Pulsed Ultrasound. *Energy Procedia* 2015;**75**:1560–8.

80. Pollet BG. *Power Ultrasound in Electrochemistry : From Versatile Laboratory Tool to Engineering Solution*. Wiley, 2012.

81. Yasui K, Tuziuti T, Lee J *et al.* The range of ambient radius for an active bubble in sonoluminescence and sonochemical reactions. *J Chem Phys* 2008;**128**, DOI: 10.1063/1.2919119.

82. Kerboua K, Hamdaoui O. Oxidants emergence under dual-frequency sonication within single acoustic bubble: effects of frequency combinations. *Iran J Chem Chem Eng* 2019;**40**:323–32.

83. Rashid MM, Mesfer MK Al, Naseem H *et al.* Hydrogen Production by Water Electrolysis: A Review of Alkaline Water Electrolysis, PEM Water Electrolysis and High Temperature Water Electrolysis. *Int J Eng Adv Technol* 2015:2249–8958.

84. Ahmad Kamaroddin MF, Sabli N, Tuan Abdullah TA *et al.* Membrane-based electrolysis for hydrogen production: A review. *Membranes (Basel)* 2021;**11**:1–27.

85. Buckner CA, Lafrenie RM, Dénommée JA *et al.* Hydrogen Production by Membrane Water Splitting Technologies. *Advances In Hydrogen Generation Technologies*. 2018, 19–37.

86. Kumar SS, Himabindu V. Materials Science for Energy Technologies Hydrogen production by PEM water electrolysis – A review. *Mater Sci Energy Technol* 2019;**2**:442–

54.

87. Plevová M, Hnát J, Žitka J *et al.* Optimization of the membrane electrode assembly for an alkaline water electrolyser based on the catalyst-coated membrane. *J Power Sources* 2022;**539**, DOI: 10.1016/j.jpowsour.2022.231476.

88. Renaud R, LeRoy RL. Separator materials for use in alkaline water electrolysers. *Int J Hydrogen Energy* 1982;**7**:155–66.

89. Schalenbach M, Lueke W, Stolten D. Hydrogen Diffusivity and Electrolyte Permeability of the Zirfon PERL Separator for Alkaline Water Electrolysis. *J Electrochem Soc* 2016;**163**:F1480–8.

90. Lv H, Chen J, Zhou W *et al.* Mechanism analyses and optimization strategies for performance improvement in low-temperature water electrolysis systems via the perspective of mass transfer: A review. *Renew Sustain Energy Rev* 2023;**183**:113394.

91. Burton NA, Padilla R V, Rose A *et al.* Increasing the efficiency of hydrogen production from solar powered water electrolysis. *Renew Sustain Energy Rev* 2020;**135**:110255.

92. Pollet BG, Foroughi F, Faid AY *et al.* Ultrasonics - Sonochemistry Does power ultrasound (26 kHz) affect the hydrogen evolution reaction (HER) on Pt polycrystalline electrode in a mild acidic electrolyte ? *Ultrason - Sonochemistry* 2020;**69**:105238.

93. Kerboua K, Merabet NH. Sono-electrolysis performance based on indirect continuous sonication and membraneless alkaline electrolysis: Experiment, modelling and analysis. *Ultrason Sonochem* 2023;**96**:106429.

94. Nour Hane Merabet KK. Green hydrogen from sono-electrolysis : A coupled numerical and experimental study of the ultrasound assisted membraneless electrolysis of water supplied by PV. *Fuel* 2024;**356**:129625.

95. Choi H, Rhyu C, Lee S *et al.* Study on Anion Exchange Membrane for the Alkaline Electrolysis. *J Hydrog New Energy* 2011;**22**:184–90.

96. Brauns J, Schönebeck J, Kraglund MR *et al.* Evaluation of Diaphragms and Membranes as Separators for Alkaline Water Electrolysis. *J Electrochem Soc* 2021;**168**:014510.

97. Merabet NH, Kerboua K. Green Hydrogen from PV-Supplied Sono-Electrolysis : Modelling and Experimental Investigations of the Mechanism and Performance. *Eurasia Proc Sci Technol Eng Math* 2023;**23**:100–5.

98. Boudries R. Analysis of solar hydrogen production in Algeria: Case of an electrolyzer-concentrating photovoltaic system. *Int J Hydrogen Energy* 2013;**38**:11507–18.

99. Ibrahim Dincer ASJ. *Solar Based Hydrogen Production Systems.*, 2013.

100. Atlam O, Barbir F, Bezmalinovic D. A method for optimal sizing of an electrolyzer directly connected to a PV module. *Int J Hydrogen Energy* 2011;**6**:1–7.

101. Burton NA, Padilla R V., Rose A *et al.* Increasing the efficiency of hydrogen production from solar powered water electrolysis. *Renew Sustain Energy Rev* 2021;**135**:110255.

102. Kova A, Marciu D, Budin L. Solar hydrogen production via alkaline water electrolysis. *Int J Hydrogen Energy* 2018;**4**:9841–8.

103. Song H, Luo S, Huang H *et al.* Solar-Driven Hydrogen Production : Recent. *ACS Energy Lett* 2022:1043–65.

104. Nguyen T, Goshome K, Endo N. Optimization strategy for high efficiency 20 kW-class direct coupled photovoltaic-electrolyzer system based on experiment data. *Int J Hydrogen Energy* 2019;**44**:26741–52.

105. Amodio L, Pagano M, Guti F. Hydrogen production by water electrolysis and off-grid solar PV. *Int J Hydrogen Energy* 2020;**46**:1–11.

106. Mraoui A, Benyoucef B, Hassaine L. Experiment and simulation of electrolytic hydrogen production : Case study of photovoltaic-electrolyzer direct connection. *Int J*

Hydrogen Energy 2017;**43**:3441–50.

107. Ghribi D, Khelifa A, Diaf S. Study of hydrogen production system by using PV solar energy and PEM electrolyser in Algeria. *Hydrog energy* 2012;**38**:1–11.

108. Villalva MG, Gazoli JR, Filho ER. Comprehensive Approach to Modeling and Simulation of Photovoltaic Arrays. *IEEE Trans POWER Electron* 2009;**24**:1198–208.

109. Rahim AHA, Salami A, Fadhlullah M *et al.* Optimization of direct coupling solar PV panel and advanced alkaline electrolyzer system. *Energy Procedia* 2015;**79**:204–11.

110. Maleki SAM, Hizam H, Gomes C. Estimation of hourly, daily and monthly global solar radiation on inclined surfaces: Models re-visited. *Energies* 2017;**10**, DOI: 10.3390/en10010134.

111. Sun Y, Dall'Agnese C, Zhang C *et al. Applications of MXenes and Their Composites in Catalysis and Photoelectrocatalysis*. INC, 2021.

112. Bandal H, Reddy KK, Chaugule A *et al.* Iron-based heterogeneous catalysts for oxygen evolution reaction; change in perspective from activity promoter to active catalyst. *J Power Sources* 2018;**395**:106–27.

113. Ameur K, Ameur A, Mokhtari B *et al.* Modeling and Control of a Photovoltaic Generator Using MPPT Regulator. *Rev des Sci Sci l'Ingénieur* 2012;**2**:9–15.

114. Lamb JJ, Pollet BG. *Micro-Optics and Energy: Sensors for Energy Devices.*, 2020.

115. Choi J, Shin M, Kim B *et al.* High-performance ceramic composite electrodes for electrochemical hydrogen pump using protonic ceramics. *Int J Hydrogen Energy* 2017;**42**:13092–8.

116. Zhu H, Ricote S, Kee RJ. Faradaic efficiency in protonic-ceramic electrolysis cells. *JPhys Energy* 2022;**4**, DOI: 10.1088/2515-7655/ac3729.

117. Park H, Kim S. Solar desalination coupled with water remediation and molecular hydrogen production: a novel solar water-energy nexus. *Energy Environ Sci* 2018;**11**:344–53.

118. Woods P, Bustamante H, Aguey-Zinsou K-F. The hydrogen economy - Where is the water? *Energy Nexus* 2022;**7**:100123.

119. Song Hu , Bin Guo, Shunliang Ding, Fuyuan Yang, Jian Dang, Biao Liu , Junjie Gu , Jugang Ma MO. A comprehensive review of alkaline water electrolysis mathematical modeling. *Appl Energy* 2022;**327**:120099.

120. Simoes SG, Catarino J, Picado A *et al.* Water availability and water usage solutions for electrolysis in hydrogen production. *J Clean Prod* 2021;**315**:128124.

121. Lu L, Guest JS, Peters CA *et al.* Wastewater treatment for carbon capture and utilization. *Nat Sustain* 2018;**1**, DOI: 10.1038/s41893-018-0187-9.

122. Arun J, Shriniti V, Shyam S *et al.* Technical insights on various routes of hydrogen production from pharmaceutical , hydrothermal , sewage and textile wastewaters : Cost comparison and challenges. *Fuel* 2023;**340**:127471.

123. Islam AKMK, Dunlop PSM, Hewitt NJ *et al.* Bio-Hydrogen Production from Wastewater: A Comparative Study of Low Energy Intensive Production Processes. *Clean Technol* 2021;**3**:156–82.

124. Pitchaimuthu S, Sridharan K, Nagarajan S *et al.* Solar Hydrogen Fuel Generation from Wastewater — Beyond Photoelectrochemical Water Splitting : A Perspective. *Energies* 2022;**15**:1–23.

125. Elgarahy AM, Ahmed MGE, Ayman H *et al.* Hydrogen production from wastewater , storage , economy , governance and applications : a review. *Environ Chem Lett* 2022;**20**:3453–504.

126. Aydin MI, Karaca AE, Qureshy AMMI *et al.* A comparative review on clean hydrogen production from wastewaters. *J Environ Manage* 2021;**279**:111793.

127. Wang B, Jiang H, Gu D *et al.* An insight into solar thermo-assisted and organic-molecule alternated water splitting chemistry for hydrogen production and wastewater treatment by elucidating redox model and thermodynamics. *Energy Convers Manag*

2020;**226**, DOI: 10.1016/j.enconman.2020.113551.

128. Gukelberger E, Atiye T, Mamo JA *et al.* Membrane Bioreactor–Treated Domestic Wastewater for Sustainable Reuse in the Lake Victoria Region. *Integr Environ Assess Manag* 2020;**16**:942–53.

129. Deowan SA, Bouhadjar SI, Hoinkis J. *Membrane Bioreactors for Water Treatment*. Elsevier Ltd, 2015.

130. Monclús H, Sipma J, Ferrero G *et al.* Biological nutrient removal in an MBR treating municipal wastewater with special focus on biological phosphorus removal. *Bioresour Technol* 2010;**101**:3984–91.

131. Becker H, Murawski J, Shinde D V. *et al.* Impact of impurities on water electrolysis: a review. *Sustain Energy Fuels* 2023;**7**:1565–603.

132. Zhemin Du, Congmin Liu, Junxiang Zhai, Xiuying Guo, Yalin Xiong, Wei Su GH. A Review of Hydrogen Purification Technologies for Fuel Cell Vehicles. *Catalysts* 2021;**393**:1–17.